Chemical Science

ROYAL SOCIETY OF CHEMISTRY

REVIEW

View Article Online
View Journal | View Issue

Cite this: *Chem. Sci.*, 2024, **15**, 11188

Selective oxygen reduction reaction: mechanism understanding, catalyst design and practical application

Shilong Li,[ab] Lei Shi,[b] Yingjie Guo,[ab] Jingyang Wang,[b] Di Liu *[a] and Shenlong Zhao *[b]

The oxygen reduction reaction (ORR) is a key component for many clean energy technologies and other industrial processes. However, the low selectivity and the sluggish reaction kinetics of ORR catalysts have hampered the energy conversion efficiency and real application of these new technologies mentioned before. Recently, tremendous efforts have been made in mechanism understanding, electrocatalyst development and system design. Here, a comprehensive and critical review is provided to present the recent advances in the field of the electrocatalytic ORR. The two-electron and four-electron transfer catalytic mechanisms and key evaluation parameters of the ORR are discussed first. Then, the up-to-date synthetic strategies and *in situ* characterization techniques for ORR electrocatalysts are systematically summarized. Lastly, a brief overview of various renewable energy conversion devices and systems involving the ORR, including fuel cells, metal–air batteries, production of hydrogen peroxide and other chemical synthesis processes, along with some challenges and opportunities, is presented.

Received 30th April 2024
Accepted 26th June 2024

DOI: 10.1039/d4sc02853h

rsc.li/chemical-science

1 Introduction

As fossil fuels are gradually depleted around the world, the development of sustainable energy sources has attracted significant attention from researchers globally.[1–6] The oxygen reduction reaction (ORR) involving four-electron or two-electron mechanisms plays a key role in renewable energy conversion technologies and some important chemical processes. For

[a]*School of Chemical & Environmental Engineering, China University of Mining and Technology (Beijing), Beijing, 100083, P. R. China. E-mail: liudi0713@163.com*

[b]*CAS Key Laboratory of Nanosystem and Hierarchical Fabrication, CAS Center for Excellence in Nanoscience, National Center for Nanoscience and Technology, University of Chinese Academy of Sciences, Beijing, 100190, P. R. China. E-mail: zhaosl@nanoctr.cn*

Di Liu

Di Liu received her B. S. degree from Shandong University in 2011 and her PhD degree from Tsinghua University in 2016. She is currently an associate professor at the China University of Mining and Technology (Beijing). Her current research is focused on the rational synthesis and mechanism exploration of perylenediimide (PDI)-based organic semiconductor materials for visible-light-driven photocatalysis and photoelectrocatalysis.

Shenlong Zhao

Shenlong Zhao received his B.E. degree from Shandong University in 2011. He obtained his PhD degree from the Harbin Institute of Technology and the National Center for Nanoscience and Technology in 2017, and then, he served as a postdoctoral fellow at the University of New South Wales and an FH Loxton research fellow at the University of Sydney. Currently, he is a professor/principal investigator at the National Center for Nanoscience and Technology. His research interests focus on the preparation and application of functional inorganic and organic carbon nanomaterials for energy conversion and storage.

example, the four-electron ORR is an ideal reaction pathway for fuel cells and metal–air batteries because it can provide the highest electron transfer and energy release efficiency. On the other hand, the two-electron electrochemical ORR process powered by electricity from wind or solar energy is considered as a green approach for producing hydrogen peroxide. Additionally, because hydrogen peroxide is a green oxidant, there have been many recent reports on its application in cascade reactions.[7] Specifically, after the generation of hydrogen peroxide, it is further reacted with substrates to achieve pollutant degradation or the production of high-value chemicals. However, the low selectivity, sluggish kinetics and high cost of ORR catalysts hinder the energy conversion efficiency and practical applications of the technologies mentioned before.

To address the above-mentioned challenges, various strategies have been proposed for theoretical studies, materials fabrication and system design. Computational calculation is employed to in-depth understand the key steps and intermediates during two-electron or four-electron ORR pathways, aiming to provide better insights into the catalytic mechanism of the ORR.[8] Substantial progress has significantly promoted catalytic materials from laboratory research to practical applications to some extent. With the recent explosive development of machine learning, researchers are leveraging existing studies on reaction mechanisms and kinetics to further advance catalyst design and mechanism exploration.[9] Machine learning is a high-throughput screening platform to accelerate catalyst discovery and optimization processes. It is primarily manifested in the effective prediction and optimization of catalyst structures, activities, and selectivity through reaction mechanism analysis and structure–performance relationship study.[10] To further understand reaction mechanisms and catalytic processes, various *in situ* characterization techniques combined with theoretical calculations are developed. The complex evolution of electrocatalysts at the molecular level is revealed by real-time monitoring of their electronic and geometric structural changes. The developed meticulous characterization approaches allow for precise monitoring of material property changes, such as electronic structure, surface composition, and catalytic activity, providing valuable information for designing efficient catalysts.[11,12]

Along with the intensive research efforts in the ORR field, various materials including noble metals, transition metals and metal-free materials have been prepared as electrocatalysts. To improve the catalytic activity, selectivity and stability, a series of approaches such as size tailoring, defect engineering and structural control have been developed. Certain four-electron ORR catalysts have been demonstrated to be even more durable and perform better than state-of-the-art precious metal catalysts in polymer electrolyte membrane (PEM) fuel cells and metal–air batteries.[13–17] Additionally, substantial progress in the electrosynthesis of industrial chemicals through the two-electron ORR has been made.[18–22] For example, carbon-based catalysts have been fabricated using a surface modification strategy and used as electrocatalysts for two-electron oxygen reduction, achieving a selectivity of over 90% towards pure H_2O_2 at a current density of 200 mA cm^{-2} using a solid electrolyte system.[23] Recently, electrochemically synthesized H_2O_2 through the ORR is further utilized to degrade sulfonated polystyrene through an advanced oxidation process (AOP).[7]

Recent achievements in the ORR make it possible for advanced energy conversion technologies to overtake the traditional ones in the race to the renewable energy and new chemical engineering marketplace. Therefore, a timely review of such a rapidly growing field of significant importance is highly desirable. This review aims to provide a comprehensive and critical updated overview of recent advances by summarizing important work reported during the past three years and presenting critical issues governing the fundamental understanding of ORR mechanisms. The key role of spectroscopy characterization techniques in structure–performance relationship study is discussed, with special emphasis on combining *in situ* characterization and computational calculations during real-time catalysis. An overview of various advanced synthesis methods for high-performance ORR electrocatalysts and their applications in renewable energy conversion devices and systems involving the ORR, along with some challenges and opportunities, is presented.

2 ORR mechanism and machine learning

In the ORR process, there are two reaction pathways that involve the two-electron and four-electron transfer processes. In the reaction process, the adsorption and desorption of *OH and *OOH are particularly important, whether it is a four-electron process or a two-electron process.[9,24–28] The catalytic ability of the catalyst to adsorb *OOH is crucial in determining whether a two-electron or four-electron ORR occurs (Fig. 1A).[12,32,33] Unlike many other reactions, there is no distinction between primary and side reactions for the two reaction pathways. Both are crucial components depending on the application scenario. In industrial production and chemical product synthesis, the two-electron ORR is the target reaction. Hydrogen peroxide, as a green oxidant and a significant chemical product, is produced through the two-electron ORR process. Compared with traditional methods, the electrosynthesis of hydrogen peroxide powered by green electricity has gained popularity in recent years because of its environmental protection and high efficiency. Besides the synthesis of hydrogen peroxides, the produced hydrogen peroxides are utilized to react with substrates for *in situ* degradation or synthesis of other high-value products. In the development of new green energy devices, the four-electron ORR is favored because of its high electron transfer, energy efficiency, and environmentally friendly reaction products, making it widely applied in fuel cells and metal–air batteries.[7,13,34,35] Based on the significant applications of the aforementioned ORR catalysts, researchers have developed numerous types of ORR catalysts in recent years, ranging from the initial platinum-based catalysts to later transition metal catalysts, and subsequently to carbon-based catalysts, single-atom catalysts, and others.[36,37] However, despite the

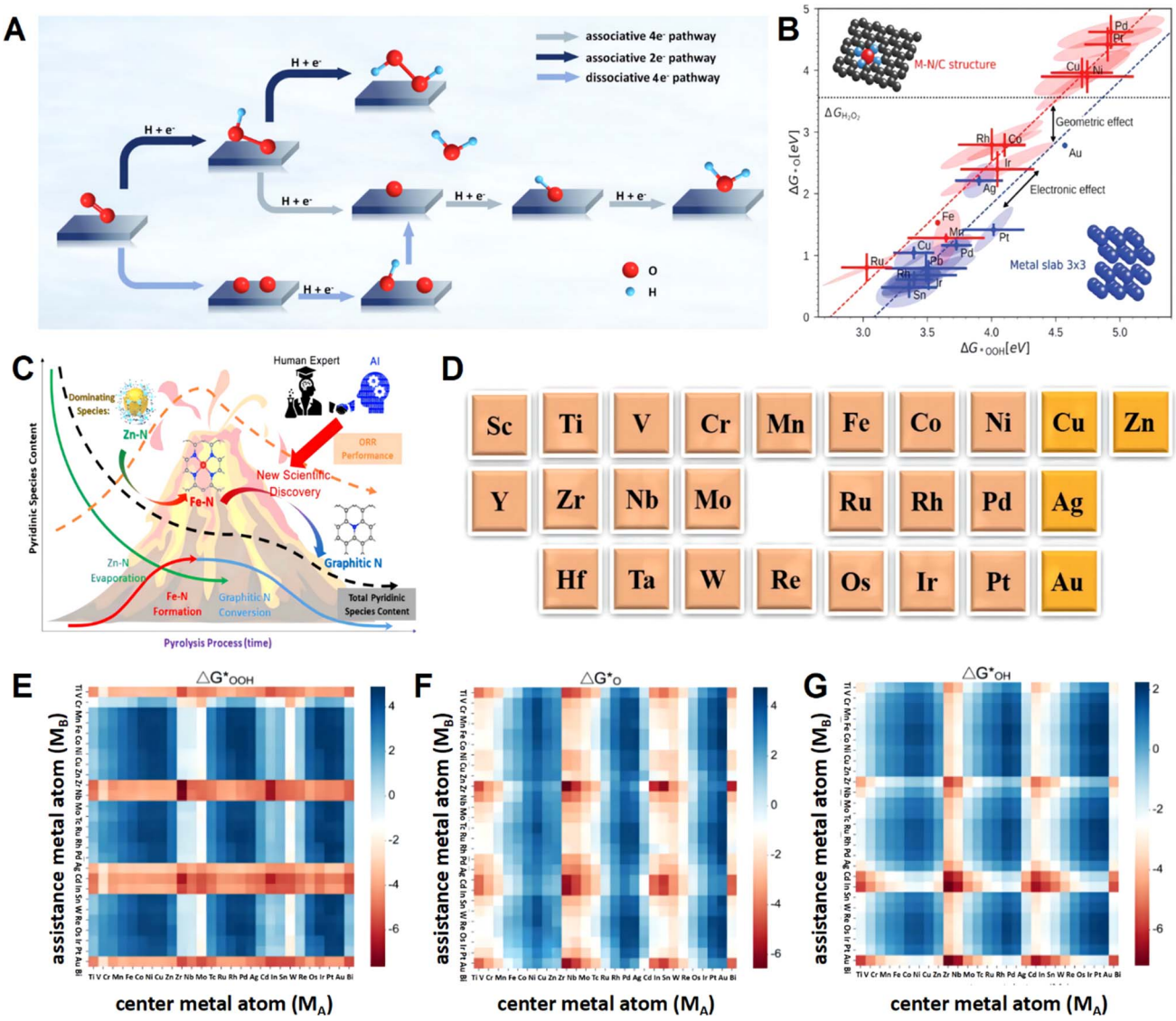

Fig. 1 (A) Schematic diagram of the ORR. (B) Adsorption trend of *OOH and *O on transition metal slabs and single-atom electrocatalysts. Reproduced from ref. 29 with permission. Copyright 2018, American Chemical Society. (C) Illustration of the mechanism discovered in this figure through collaboration between human experts and AI. Reproduced from ref. 30 with permission. Copyright 2021, American Chemical Society. (D) Element type of central metal atom. Reproduced from ref. 10 with permission. Copyright 2021, Elsevier. Heat map of ML-predicted values for ΔG_{*OOH} (E), ΔG_{*O} (F), and ΔG_{*OH} (G). Reproduced from ref. 31 with permission. Copyright 2024, American Chemical Society.

promising performance exhibited by various catalysts, challenges such as low selectivity and poor stability persist. Therefore, further exploration of the mechanisms, kinetics, and thermodynamics involved in the ORR process, clarifying the differences between the two-electron ORR and four-electron ORR in this process, and using this information to guide the design and development of catalysts are particularly crucial for the development of high-selectivity catalysts.

For the two-electron ORR, the adsorption of *OOH is the key to the entire reaction process. Therefore, when theoretical calculations are needed to screen two-electron ORR catalysts, the first consideration is the binding energy between the active sites and *OOH, denoted as ΔG_{*OOH}. Excellent two-electron ORR catalysts have similar requirements for ΔG_{*OOH} as in the hydrogen evolution reaction, where neither too strong nor too weak binding of the key intermediate is desired.[27] In contrast to the two-electron ORR, there are three key intermediates for the four-electron ORR, namely *O, *OH, and *OOH. The requirements for ΔG_{*OH}, ΔG_{*OOH}, and ΔG_{*O} are different for the four-electron ORR. Additionally, there exists a strong correlation between their binding energies. Therefore, during catalyst screening, researchers need to consider the electronic structure and adjust the active sites to ensure the selection of high-quality four-electron ORR catalysts.[38,39] Taking metals as an example, as shown in Fig. 1B, different types of metals exhibit significantly different adsorption behaviors towards intermediates. Based on this, different selectivity outcomes can be achieved by selecting the corresponding metals.

2.1 Two-electron ORR

The two-electron ORR process can be divided into alkaline and acidic conditions. During the alkaline process, the active site first binds with oxygen and then receives an electron and a proton to form *OOH. Subsequently, it accepts another electron to form HO_2^- and finally desorbs to complete the reaction. The reaction that occurs under acidic conditions differs from the reaction under alkaline conditions, and abundant free H^+ ions can react with *OOH to form H_2O_2 directly. The specific processes under alkaline and acidic conditions are as follows, where A represents activity sites.

Alkaline process:

$$A + O_2 \rightarrow A\text{-}O_2 \quad (1)$$

$$A\text{-}O_2 + H_2O + e^- \rightarrow A\text{-}OOH + OH^- \quad (2)$$

$$A\text{-}OOH + e^- \rightarrow A + HO_2^- \quad (3)$$

The overall reaction of the two-electron pathway is $O_2 + H_2O + 2e^- \rightarrow HO_2^- + OH^-$ (−0.076 V *vs.* SHE, pH = 14).

Acidic process:

$$A + O_2 \rightarrow A\text{-}O_2 \quad (4)$$

$$A\text{-}O_2 + H^+ + e^- \rightarrow A\text{-}OOH \quad (5)$$

$$A\text{-}OOH + H^+ + e^- \rightarrow A + H_2O_2 \quad (6)$$

The overall reaction of the two-electron pathway is $O_2 + 2H^+ + 2e^- \rightarrow H_2O_2$ (0.695 V *vs.* SHE, pH = 0).

In the above process, it can be observed that a key point for the two-electron process is the acquisition of an electron by A-OOH to generate HO_2^- and H_2O_2. This also serves as an important basis for designing two-electron catalysts. It is worth noting that in the two-electron process, after the completion of the reaction, both H_2O_2 and HO_2^- will undergo continuous reduction.[40] The involved reactions are

$$HO_2^- + H_2O + 2e^- \rightarrow 3OH^- \quad (7)$$

$$H_2O_2 + 2H^+ + 2e^- \rightarrow 2H_2O \quad (8)$$

Therefore, the protection of products in the two-electron ORR should also be considered in the initial design of catalysts.

2.2 Four-electron ORR

The four-electron ORR process can be divided into alkaline and acidic conditions; the reactions occurring in an acidic environment and an alkaline environment essentially have no significant differences,[41] and the specific processes are as follows, where A represents activity sites.

Alkaline process:

$$A + O_2 \rightarrow A\text{-}O_2 \quad (9)$$

$$A\text{-}O_2 + H_2O + e^- \rightarrow A\text{-}OOH + OH^- \quad (10)$$

$$A\text{-}OOH + e^- \rightarrow A\text{-}O + OH^- \quad (11)$$

$$A\text{-}O + H_2O + e^- \rightarrow A\text{-}OH + OH^- \quad (12)$$

$$A\text{-}OH + e^- \rightarrow A + OH^- \quad (13)$$

The overall reaction of the four-electron pathway is $O_2 + 2H_2O + 4e^- \rightarrow 4OH^-$ (0.401 V *vs.* SHE, pH = 14).

Acidic process:

$$A + O_2 \rightarrow A\text{-}O_2 \quad (14)$$

$$A\text{-}O_2 + H^+ + e^- \rightarrow A\text{-}OOH \quad (15)$$

$$A\text{-}OOH + H^+ + e^- \rightarrow A\text{-}O + H_2O \quad (16)$$

$$A\text{-}O + H^+ + e^- \rightarrow A\text{-}OH \quad (17)$$

$$A\text{-}OH + H^+ + e^- \rightarrow A + H_2O \quad (18)$$

The overall reaction of the four-electron pathway is $O_2 + 4H^+ + 4e^- \rightarrow 2H_2O$ (1.229 V *vs.* SHE, pH = 0).

It is worth noting that the difference between two-electron and four-electron pathways lies in the fact that different types of oxygen adsorption can trigger different reaction mechanisms. This is attributed to the binding strength between O_2 and the active site.[42] When the active site has a strong affinity for O_2, O_2 is parallelly adsorbed by two neighboring active centers, and then a bridging oxygen configuration (A-O-O-A) is formed. The adsorbed O_2 subsequently couples with a proton to form an A-OH intermediate, which is further reduced to H_2O. In contrast, the end-on adsorbed O_2 undergoes proton-coupled electron transfer, forming a MOOH intermediate. In the case of the electron transfer pathway, A-O and A-OH are formed successively, ultimately resulting in H_2O formation. Compared to the bridging oxygen configuration, the end-on oxygen configuration has higher efficiency, and the reaction is also accelerated, which is very important for catalyst design and performance.[33,43]

Dissociative four-electron pathway:

$$A + O_2 \rightarrow A\text{-}O_2 \quad (19)$$

$$A\text{-}O_2 \rightarrow 2A\text{-}O \quad (20)$$

$$2A\text{-}O + 4H^+ + 4e^- \rightarrow 2H_2O \quad (21)$$

2.3 Machine learning

In recent years, the rapid advancement of machine learning technology, which emulates human thinking to perform tasks like our brain does, has significantly affected various industries.[44] In the field of chemistry, machine learning leverages existing theoretical research and data to develop predictive models, thereby significantly advancing catalyst design and mechanism research. Specifically, researchers can design and construct the prediction tool by generating an experimental dataset to investigate various reactant networks under diverse reaction conditions. Through a systematic experimental design process, the neural network model actively learns from

numerous catalytic processes. As the dataset expands, the developed workflow continuously improves the predictive capability, thereby facilitating the accuracy of prediction of highly active catalysts.[45–51] As shown in Fig. 1C, researchers utilize machine learning to analyze a large amount of data and explain the mechanism underlying changes in pyridinic nitrogen species in iron-doped ZIF-derived ORR catalysts. They observe that prolonged pyrolysis leads to excessive graphitization that converts Fe–N active sites into inactive graphitic nitrogen sites, thereby reducing the total nitrogen content and diminishing the abundance of active sites in the final stage. Subsequently, a new machine learning model is constructed using further data and analyses to reveal the underlying mechanism of this combination and predict the interrelationship.[30] Differing from the aforementioned approach, another application method of machine learning involves constructing models and predicting materials before the start of experiments, and conducting experiments based on the prediction results. Unlike traditional theoretical calculations, machine learning begins with reaction mechanisms and determines the optimal combinations for specific reaction pathways by exploring various arrangements and selections of metals, along with multiple intermediates. Furthermore, machine learning can also analyze reaction mechanisms and uncover the interactions between catalysts and substrates, thus aiding in the comprehension of the fundamental principles of catalytic reactions. For instance, the best-performing models are used to predict the adsorption free energies of adsorbates (G_{*OOH}, G_{*O}, and G_{*OH}) for multi-metal substances and dual-metal-site catalysts (Fig. 1D).[31] In Fig. 1E–G, three sets of data (G_{*OOH}, G_{*O}, and G_{*OH}) calculated using machine learning show that different metal combinations result in varied effects.[52] Particularly, in the design of bimetallic catalysts, the selection of the corresponding metal combinations is based on the target product and reaction pathway. Although machine learning enables the calculation of more accurate data, the high quality of the constructed model and the accuracy of the existing training data are crucial. To build more accurate models, researchers need to obtain more precise reaction mechanisms and collect extensive data based on these mechanisms for constructing new study models. The complementary and mutually reinforcing relationship between experimental work and machine learning is essential for their joint development and progress. Researchers should balance their focus on both aspects to promote overall advancement.[53]

3 Catalytic performance evaluation

Electrochemical testing is a commonly used method to evaluate the activity and stability of ORR catalysts. Objective assessment of catalytic activity is crucial for screening the best catalysts and establishing broad structure–activity relationships, providing a foundation for benchmark catalysts in practical applications.[54] Additionally, electrochemical testing can also be used to evaluate the stability of ORR catalysts. During long-term testing, monitoring whether the catalyst's electrochemical activity declines and observing any structural changes or dissolution of the catalyst can provide information about its stability and durability. Therefore, ORR electrochemical testing can be employed not only for the evaluation and screening of catalysts, but also for the investigation of catalytic mechanisms.[55] However, relying solely on a single testing method is not reliable, hence the importance of combining multiple measurement techniques to accurately evaluate catalyst properties, such as elemental composition, electrochemically active surface area (ECSA), Faraday efficiency (FE), and electrochemical stability, among others. Nevertheless, many of the current methods lack standardization, posing obstacles in accurate comparison of the catalytic activity and stability of various catalysts. In this section, various testing methods will be introduced, and the appropriate methods for different types of catalysts will be discussed.[56]

3.1 Linear sweep voltammetry

Linear sweep voltammetry (LSV) is a widely used electrochemical testing method. ORR testing is generally performed using the rotating ring-disk electrode (RRDE), where different LSV curves are obtained at different rotation speeds to achieve evenly spaced ORR LSV curves. Several key parameters are involved, such as limiting current density (j_l), half-wave potential ($E_{1/2}$), and onset potential (E_{onset}).[57] The E_{onset} can be defined as the potential corresponding to a current density of 0.1 mA cm^{-2}, while the $E_{1/2}$ can be defined as the potential corresponding to half of the j_l. Typically, the $E_{1/2}$ for commercial Pt/C is around 0.82 V *versus* relative hydrogen electrode (*vs.* RHE),[58] which is an important indicator to evaluate the performance of ORR catalysts. The scan rate is generally set at 5–20 mV s^{-1}.[52]

3.1.1 Experimental principle. Firstly, the electrode reaction can be fundamentally divided into four steps: mass transfer, adsorption, surface reaction, desorption.[59] The ORR at the electrode surface is very fast, leading to a rapid decrease in oxygen concentration near the electrode. As the reaction time increases, the oxygen content also gradually reduces. This means that the oxygen concentration near the electrode varies with time. Therefore, it is generally recommended to purify oxygen for half an hour before the test to easily achieve saturation and minimize the influence of oxygen changes.[60,61]

3.1.2 Rotating-ring disk electrode technique. In 1942, Levich first proposed rotating disk electrode (RDE) theory based on the principles of fluid dynamics, which attracted widespread attention in the field of electrochemistry.[62,63] The RDE overcomes certain drawbacks of stationary electrodes and classical vibrating wire electrodes, taking electrochemical development to a new level. To study the distribution of surface current density on electrodes and reduce or eliminate the influence of factors such as the diffusion layer, researchers have developed a high-speed rotating electrode by comparing various electrode configurations and stirring methods. This electrode that is shaped like a disk on one end is also referred to as a RDE. The RDE can establish a uniform and stable diffusion layer and possesses advantages such as ease of achieving steady-state and good reproducibility of polarization curves. Researchers can control mass transfer in solution through different rotation speeds. It is suitable for determining diffusion process parameters in

solutions or researching the electrochemical reaction kinetics of solid electrodes. In the case of the RRDE, a platinum ring is added around the periphery of the RDE.[62] By measuring the ring current and the disk current, more accurate calculations of Faraday efficiency, the number of electron transfers, *etc.*, can be obtained. The relevant formulae are as follows:

$$\mathrm{FE} = \frac{i_{\mathrm{ring}}}{i_{\mathrm{disk}} \times N} \tag{22}$$

$$n = 4 \times \frac{i_{\mathrm{disk}}}{i_{\mathrm{disk}} + i_{\mathrm{ring}}/N} \tag{23}$$

where i_{ring} and i_{disk} denote the ring and disk currents, respectively, and N is the current collection efficiency of the RRDE.[64]

It should be noted that variations in the quality of the catalyst film can result in different measured values of the limiting diffusion current, even with identical samples and test conditions. Therefore, ensuring consistent film quality during each sample deposition to minimize random errors is of paramount importance in RRDE testing.[65] Researchers observe the sample using SEM after sample preparation is completed to determine the optimal preparation conditions.[66]

3.1.3 Koutecky–Levich analysis. When the reaction occurring on the surface of a RDE is controlled by both diffusion and kinetic processes, the observed total current destiny (J) is the sum of the diffusion current destiny (J_{L}) and the kinetic current destiny (J_{k}), which is commonly referred to as the Koutecky–Levich (K–L) equation.[67]

$$\frac{1}{J} = \frac{1}{J_{\mathrm{L}}} + \frac{1}{J_{\mathrm{K}}} = \frac{1}{B\omega^{1/2}} + \frac{1}{J_{\mathrm{K}}} \tag{24}$$

$$B = 0.62nFC_0(D_0)^{2/3}\nu^{-1/6} \tag{25}$$

here F is the Faraday constant, C_0 is the concentration of O_2 in the electrolyte, D_0 is the diffusion coefficient of O_2 in the electrolyte, ν is the viscosity of the electrolyte, and ω is the rotational speed of the electrode (rad s^{-1}). According to the equation, the reciprocal of the current exhibits a linear relationship with $\omega^{-1/2}$, known as the K–L plot. The intercept of this line is equal to $1/J_{\mathrm{k}}$, allowing the extraction of the electron transfer number (n) from the slope of the K–L plot. It is worth noting that the K–L curve is only a reliable method to determine n at sufficiently high overpotentials.[68]

3.2 Electrochemically active surface area

In practical applications, it is common to compare the geometric ORR activity of a series of catalysts by comparing the E_{onset} or $E_{1/2}$.[69–71] The following factors should be particularly noted: firstly, the geometric activity is closely related to the catalyst loading. The more catalyst is on the electrode, the lower the overpotential required to achieve a given geometric current density. Furthermore, geometric activity cannot reflect the intrinsic activity because intrinsic activity is defined as a key descriptor of conventional surface electrocatalytic reactions and only involves a limited number of catalytically active species. For example, the same catalyst loaded on different working electrode substrates exhibits significant differences in their geometric activity.[72] Additionally, nanoscale electrocatalysts often provide a much higher surface area compared to their loaded electrode's geometric surface area. Accurately estimating the intrinsic catalytic activity is a prerequisite for determining the optimal electrocatalyst. Previous studies have shown that the normalized current density with respect to the ECSA is a reasonable strategy to examine the intrinsic activity. There are two commonly used electrochemical methods to determine the ECSA: (i) cyclic voltammetry (CV) and (ii) electrochemical impedance spectroscopy (EIS).[73–75] For the first method, CV curves at several different scan rates (ν) are obtained in the non-faradaic region to extract the double-layer capacitance (C_{dl}). This region is typically limited to a 0.1 V range centered around the open circuit potentail (OCP). The relationship between the obtained C_{dl} and ν, as well as the charging current (i_{c}), is given by the following equation:

$$C_{\mathrm{dl}} = \frac{i_{\mathrm{c}}}{\nu} \tag{26}$$

In the second method, EIS is performed in the non-faradaic region. A Nyquist plot is obtained using the application of sinusoidal potential

$$C_{\mathrm{dl}} = \left[Q_0\left(\frac{1}{R_{\mathrm{s}}} + \frac{1}{R_{\mathrm{ct}}}\right)^{(a-1)}\right]^{\frac{1}{a}} \tag{27}$$

$$Q_0 = \frac{1}{\mathrm{ZCPE}(i\omega)^{1-a}} \tag{28}$$

In the equation, ZCPE represents frequency-dependent impedance, with α being the phase angle, ω representing the frequency of the applied sinusoidal potential, and $i = (-1)^{1/2}$. The ECSA can be calculated using C_{dl}, and A is the working electrode area.

$$\mathrm{ECSA} = A\frac{C_{\mathrm{dl}}}{C_0} \tag{29}$$

The electrochemically determined ECSA is on the same order of magnitude as the catalyst surface area. However, it should be noted that inaccurate measurement values of C_{dl} can arise when the adsorption of charged species dominates over pure double-layer charging in non-faradaic reactions. Therefore, the accuracy of ECSA-based determination of the catalyst surface area cannot be guaranteed, and caution should be exercised when using the ECSA to compare the catalytic performance of different materials.[65,75] In the cases where the ECSA cannot be used for comparing material activity, researchers can estimate the number of active sites by analyzing the oxidation and reduction peaks of the metal center.[76–79]

3.3 Turnover frequency

Turnover Frequency (TOF) is a parameter commonly used in catalysis to measure the activity of a catalyst. It represents the number of catalytic reactions or turnovers per active site per unit of time. TOF is calculated by dividing the rate of the

catalytic reaction by the number of active sites present on the catalyst surface. It provides valuable information on the efficiency and performance of a catalyst and is often used for comparing the catalytic activities of different materials.

$$\mathrm{TOF} = \frac{IA}{znF} \tag{30}$$

In the equation, I (mA cm^{-2}) represents the current density at a constant overpotential, A denotes the working electrode area, z represents the number of electrons transferred in the catalytic reaction, n represents the number of active sites (mol), and F denotes the Faraday constant (96 485 C mol^{-1}).

However, due to the difficulty in determining the exact number of active sites, there can be deviations in the calculation of TOF. Therefore, considering different types of materials, the following methods are presented for calculating TOF.[61,80] Here, only materials with metal as the active site are considered.

(a) $\mathrm{TOF_{Bulk}}$: all bulk-phase metal atoms are considered as active sites[81]

$$\mathrm{TOF_{bulk}} \times N_1 = \frac{IN_A}{zFm} \tag{31}$$

m (g cm^{-2}) represents the mass loading per cm^2 (if not otherwise specified, this area refers to the electrode reaction area), N_A is Avogadro constant, and N_1 (g^{-1}) denotes the number of active sites per gram of catalyst, which can be determined using inductively coupled plasma analysis. However, this method considers all metals as active sites, which can lead to an underestimation of TOF values and is more suitable for single-atom catalysts.[81]

(b) $\mathrm{TOF_{Surface}}$: all surface metal atoms are considered as active sites[81]

$$\mathrm{TOF_{Surface}} \times N_2 = \frac{IN_A}{zFmSg} \tag{32}$$

m (g cm^{-2}) represents the mass loaded per cm^2, Sg (m^2 g^{-1}) denotes the BET surface area (unless otherwise specified, this area is the electrode reaction area), and N_2 (m^{-2}) represents the number of active sites per m^2. However, this method considers the physical surface area measured by N_2 adsorption as the electrochemically active area, which may lead to an underestimation of the TOF. Calculation methods for the electrochemical surface area, such as the hydrogen adsorption/desorption method, CO stripping method, and non-faradaic region calculation based on the roughness factor, are specifically designed for noble and transition metals.[82]

(c) $\mathrm{TOF_{Redox}}$: metal atoms involved in oxidative electron transfer are considered as active sites[81]

These high-valent Ni(III) species are regarded as active sites for the oxygen evolution reaction (OER), initiating the OER process. Therefore, if the number of electrons involved in the redox transfer is known, the number of active sites can be determined by integrating the $Ni^{2+/3+}$ redox charge Q (peak area).

$$\mathrm{TOF_{Redox}} = \frac{Iz}{zQ_{\mathrm{Redox}}} \tag{33}$$

However, this method has limitations and is only suitable for electrocatalysis involving redox reactions and for determining the number of electron transfers in specific transition metals such as Ni, Co, Cu, *etc.* Further analysis is required depending on the specific circumstances.[83]

$\mathrm{TOF_R}$: ring current is used for calculating TOF [82]

Similar to the third method, for the OER, the TOF can be calculated using the ring current (oxygen two-electron reduction to hydrogen peroxide) collected from RRDE measurements.

$$\mathrm{TOF_R} = \frac{I_R}{S \times F \times z \times N \times n} \tag{34}$$

I_R represents the ring current, S denotes the electrode area, F is the Faraday constant (96 485 C mol^{-1}), z is the number of electron transfers in the catalytic reaction, N signifies the ring current collection efficiency in the RRDE ($N = 0.37$), and n represents the surface concentration or quantity of active sites (m^{-2}). Therefore, when conducting TOF measurements for different types of catalysts, researchers should choose the corresponding TOF measurement method to obtain the most accurate assessment of catalyst performance.[84]

3.4 Mass activity

In practical applications, calculating mass activity is a direct method for evaluating catalytic activity.[74,85] The formula for mass activity is as follows:

$$\text{Mass activity} = \frac{I/A}{\text{Loading mass}} \tag{35}$$

here I is current and A is electrode area. Loading mass refers to the total amount of dried material loaded on the electrode. Typically, the calculation of mass activity should be based on a specific potential, with a commonly chosen potential of 0.9 V *vs.* RHE for the ORR.[74]

3.5 Tafel slope

The mathematical expression of the Tafel equation is:

$$\eta = a + b \log j \tag{36}$$

where overpotential η and current density j are both taken as absolute values. Constants a and b are known as Tafel constants, and their values depend on the properties of the electrode material, electrode surface state, solution composition, and temperature. The magnitude of the Tafel slope can be used to compare the ease of electron transfer steps in different electrode systems.[86]

3.6 Product detection

In the product detection of the ORR, the primary focus lies in detecting the two-electron ORR product of H_2O_2. H_2O_2 detection is typically achieved by monitoring the UV absorption values of

Ce^{4+} ions, enabling the calculation of hydrogen peroxide concentration. Initially, $Ce(SO_4)_2$ solution with a concentration of 0.5 mM is prepared and then further diluted to various concentrations of standard solutions using H_2SO_4 solution. Subsequently, absorbance values are measured at 318 nm using UV-Visible spectrophotometry, and a standard curve is plotted to calculate the H_2O_2 concentration. Subsequently, to determine the yield, researchers need to, at regular intervals during the electrode working process, mix a certain volume of the cathodic reaction solution with 0.5 mM $Ce(SO_4)_2$ solution to prepare a 4 mL solution. After a period of incubation, the absorbance value is measured using UV-visible spectrophotometry. By comparing the absorbance value with the standard curve, the H_2O_2 concentration can be determined, allowing for the calculation of the H_2O_2 yield.[19]

3.7 Stability test

Durability testing is a critical component for assessing the stability of catalysts. This process typically employs the chronoamperometry and chronopotentiometry electrochemical method, wherein a constant potential/current is applied on the electrode surface, and the extent of decay in current/potential over long-term testing periods is observed. For the two-electron ORR, it is necessary to not only maintain a stable current but also periodically verify product yields to ensure the stability of hydrogen peroxide production. In contrast, the four-electron ORR, commonly used in fuel cells, requires an additional methanol tolerance test due to the use of methanol in certain fuel cell anode reactions. The testing method remains consistent with regular stability testing methodology, except for methanol, which is specifically introduced during the testing process.[87]

4 *In situ* characterization techniques

The term "*in situ*" refers to the characterization testing and real-time monitoring of a given catalyst during catalytic reactions. *In situ* monitoring generally includes various aspects, such as structural and morphological analysis, reaction intermediate detection, and fine structure monitoring. In recent years, the number of studies based on *in situ* characterization techniques has significantly increased, substantially advancing the development of reaction mechanisms, reaction kinetics, and reaction thermodynamics.[56,88,89] Also, researchers have gradually focused on utilizing these characterization techniques to guide the design of catalysts.[72,90–92]

4.1 Electron microscopy

Chemical characterization provides in-depth insights into the structure, properties, and reaction mechanisms of substances. The ORR is typically performed under harsh acidic or alkaline conditions, making it important to observe the catalyst's structural stability and transformation during the reaction process.[93–96] Furthermore, the complex reaction kinetics, multiple electron transfer processes, and adsorption–desorption of intermediates in ORR catalysts also hinder comprehensive understanding of the reaction mechanism. Therefore, researchers can rely on *in situ* or other advanced characterization techniques to capture key active intermediates during the catalytic activation process and gain a more comprehensive understanding of the reaction mechanism.[97–99] However, no single technique is universally applicable due to inherent limitations based on their principles. Therefore, using a combination of multiple characterization techniques and multiple instruments is the future direction of characterization technology development.[100,101] In this chapter, we will briefly introduce the working principles and advantages of numerous advanced characterization techniques and discuss some representative articles on the application of *in situ* characterization to enhance readers' understanding.

4.1.1 *In situ* electrochemical scanning tunnelling microscopy. *In situ* electrochemical scanning tunnelling microscopy (ECSTM) is a technique that combines electrochemistry with STM techniques to enable real-time observation and investigation of surface structures and electrochemical reactions at the atomic scale (Fig. 2A).[105–107] ECSTM utilizes the *in situ* control capability of electrochemistry and the high-resolution features of STM to observe and manipulate nanoscale structures and chemical changes on the electrode surface in an electrochemical system.[102,108,109] By controlling the electrode potential, ECSTM allows for the direct observation of changes in the surface structure and morphology before and after the reaction at the atomic scale (Fig. 2B). Besides, ECSTM is often used to study the surface mechanisms and kinetic processes of electrochemical reactions, such as adsorption, dissolution, and electrochemical corrosion of electrodes.[110] Additionally, ECSTM can be employed to investigate the electrocatalytic performance and interface characteristics of electrode materials, which is of crucial importance in the design and optimization of novel electrochemical catalysts and materials (Fig. 2C). Despite its advantages, ECSTM has some limitations, such as the probe size restrictions under high current density conditions and potential interference from the electrolyte on the probe and electrode surface during electrochemical reactions.[103,111] Therefore, careful selection and optimization of experimental conditions are required to ensure reliable results.[109] *In situ* experiments provide direct evidence for electrocatalytic processes and can significantly advance the field of electrocatalysis.[112]

For instance, the synergistic effect of Mg^{2+} in a CoPc-catalyzed carbon dioxide reduction reaction (CO_2RR) is investigated through *in situ* electrochemical experiments.[104] Electrochemical measurements demonstrated that CoPc exhibited higher CO_2RR activity in electrolytes containing Mg^{2+}. An ordered monolayer of CoPc was prepared on Au (111) and analyzed at the molecular level using ECSTM. In a CO_2 environment, high contrast species were observed in the CoPc monolayer, attributed to the adsorption of CO_2 on CoPc, confirming its catalytic conversion during the CO_2RR. ECSTM experiments revealed that the CO_2-bound complex exhibited higher contrast and surface coverage in electrolytes containing Mg^{2+} compared to those without Mg^{2+}. As shown in Fig. 2D, the red bright spots represent active centers, and the white spots indicate adsorbed CO_2, the amount of which can be obtained by

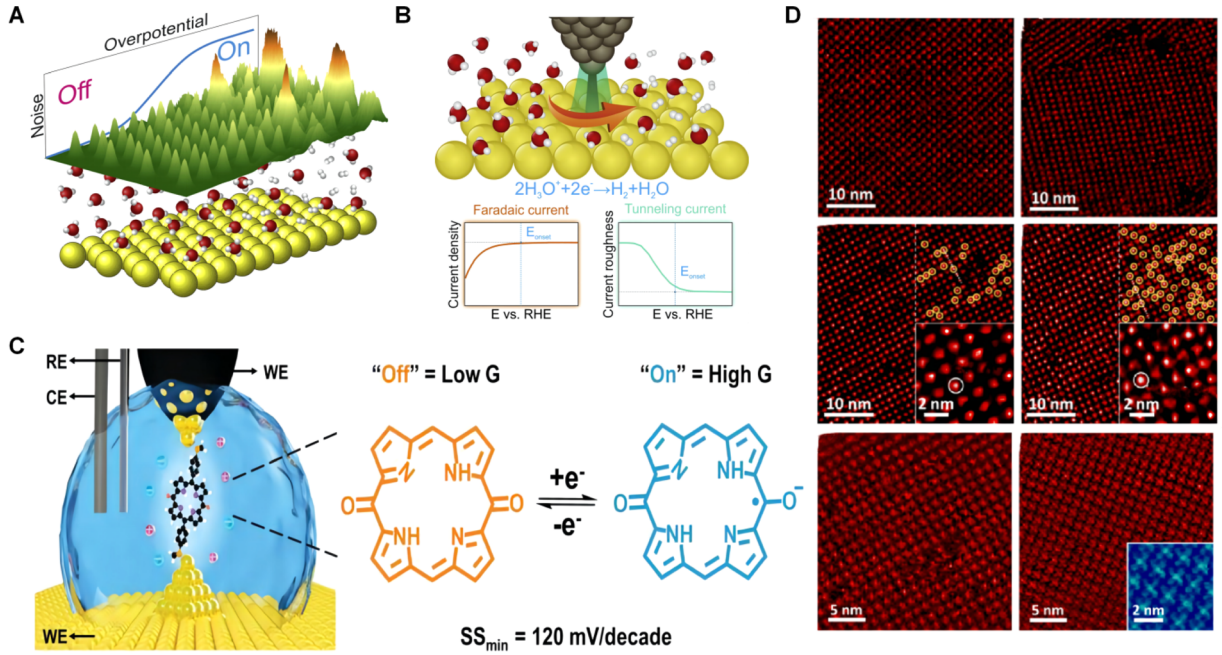

Fig. 2 (A) Monitoring the recorded ECSTM signal noise under reaction conditions. (B) Reaction process diagram. Reproduced from ref. 102 with permission. Copyright 2022, Elsevier. (C) Schematic characterization of a molecular junction using a lab-built ECSTM-BJ instrument. Reproduced from ref. 103 with permission. Copyright 2023, Wiley-VCH GmbH. (D) Section analysis of ECSTM images as marked in panels. Reproduced from ref. 104 with permission. Copyright 2022, American Chemical Society.

measuring the relative height, enabling the observation of the entire catalytic process. Similar to the CO_2RR, the ORR also involves gas adsorption and bond breaking, suggesting that this method can be extended to observe active centers and further improve theoretical analysis in ORR studies. ECSTM should be promoted in the future development of electrocatalysis to facilitate industry advancement.

4.1.2 Electrochemical liquid transmission electron microscopy. Electrochemical liquid transmission electron microscopy (ELECTEM) is a technique that combines the capabilities of transmission electron microscopy (TEM) with the ability to study electrochemical processes in a liquid environment. Unlike traditional TEM, which typically requires a vacuum for sample analysis, ELECTEM allows for real-time observation and analysis of dynamic electrochemical reactions at the nanoscale.[113,114] In ELECTEM, a liquid cell is used to encapsulate the working electrode, counter electrode, and electrolyte solution, forming a small liquid chamber. Liquid cells are typically made of thin and transparent electron-transparent materials like silicon nitride or graphene, allowing the electron beam to pass through and irradiate the sample. By applying an external potential between the working and counter electrodes, electrochemical reactions can be induced at the working electrode surface. The electron beam is then directed to the liquid cell to interact with the sample, and the transmitted electrons are captured by a detector, enabling real-time monitoring of the sample's electrochemical reactions while maintaining high-resolution imaging capabilities.[115,116] ELECTEM has played a crucial role in studying various electrochemical processes including electrodeposition, corrosion, battery reactions, and electrocatalysis. It offers direct observation of morphological and structural transformations within the sample during electrochemical reactions, thereby providing valuable insights into reaction mechanisms and kinetics.[117–120] However, ELECTEM also faces several challenges such as sample drift, electron beam-caused sample damage, and background noise from the liquid. Furthermore, high-energy electron beam can induce radiolysis of the liquid, generating active species that may influence the observed electrochemical reactions.[121] Nevertheless, ELECTEM remains a powerful tool for understanding the fundamental processes of electrochemical reactions in liquid environments. This technology will also play a significant role in the design and optimization of new materials and devices for energy storage, catalysis, and other fields.[122]

One illustrative example of ELECTEM's application is the *in situ* environmental TEM investigation of the competitive processes between sintering and aerosolization.[123] Researchers observed the structural evolution from Pd nanoparticles to single atoms by utilizing the apparatus across temperatures ranging from 100 to 1000 °C. As shown in Fig. 3A, a stable increase in the average particle diameter and a decrease in the particle number were observed from room temperature to 900 °C, indicating that aggregation took place. Upon heating to 1000 °C, both aggregation and aerosolization rates were accelerated to a certain extent. Subsequently, combined *in situ* TEM observation and density functional theory (DFT) calculations demonstrated that sintering dominated at low temperatures (300–900 °C) and aerosolization controlled the process at high temperatures. Their work clearly reveals the atomization process of noble metals such as platinum, palladium, and gold, shedding light on their involvement in various catalysis. In addition to the conventional morphological observations, the

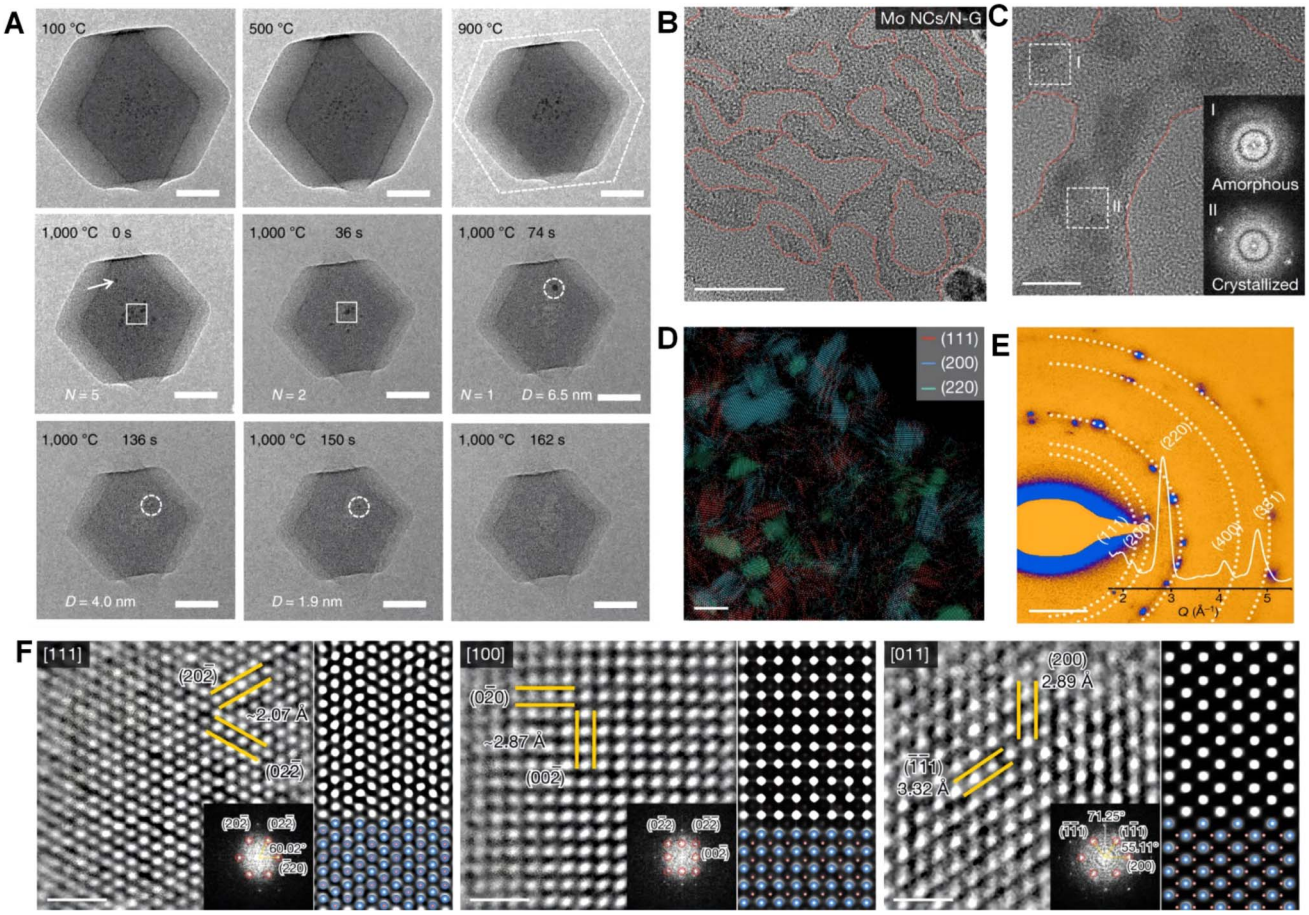

Fig. 3 (A) Pd-NPs@ZIF-8 *in situ* pyrolysed with ETEM under an Ar atmosphere at various temperatures and times. Reproduced from ref. 123 with permission. Copyright 2018, Nature Publishing Group. (B) and (C) HRTEM images of deposited Li_2S on Mo NCs/N-G after potentiostatic discharge at −0.5 V in an electrochemical liquid cell. (D) Li_2S was mainly composed of (111), (200) and (220) crystal planes, represented by red, blue and green, respectively. (E) SAED pattern and the corresponding intensity integration, showing the diffraction peaks of polycrystalline Li_2S. (F) Radial Wiener-filtered HRTEM images and FFT patterns of deposited nanocrystalline Li_2S along the [111], [100] and [011] directions. Reproduced from ref. 124 with permission. Copyright 2023, Nature Publishing Group.

characteristics of TEM enable real-time monitoring of changes in the crystal structure. As shown in Fig. 3B and C, with the increase in voltage, the morphology and structure of the catalyst itself also undergo changes. This observation is further confirmed by the data processing results shown in Fig. 3D and E. The subsequent monitoring of the material's crystal structure revealed the corresponding changes in the structure after applying different voltages, as evident in the high resolution transmission electron microscope (HRTEM) images and fast Fourier transform (FFT) patterns. This has provided researchers with an understanding of how the material's structure changes after applying varying voltages.

4.2 Fourier transform infrared spectroscopy

Fourier transform infrared spectroscopy (FTIR) is a commonly used analytical technique to study the molecular structure and chemical bonds of chemical substances by measuring the absorption, scattering, or transmission of infrared radiation.[125] In FTIR, the sample is exposed to radiation from an infrared light source, and the infrared radiation interacts with the chemical bonds in the sample, leading to the absorption or scattering of energy. By measuring the absorption or scattering of infrared radiation by the sample, information regarding its molecular structure, chemical bonds, and functional groups can be obtained. This information can be used to determine the composition of the sample, detect chemical reactions and changes, and understand the chemical reaction process and kinetics.[126] One of the advantages of FTIR is its high selectivity and sensitivity, allowing for the detection and analysis of various types of chemical substances. Additionally, FTIR is a non-destructive analytical technique, eliminating the need for sample treatment or destruction. Therefore, it is widely applied in various fields including chemistry, pharmaceuticals, materials science, environmental science, and biomedical science. In FTIR experiments, an interferometer is typically used to measure the intensity of infrared radiation absorbed or scattered by the sample. The infrared signal is then transformed into its frequency spectrum representation using Fourier transform algorithms, resulting in the FTIR spectrum of the sample. This spectrum is presented as a graph with the

wavenumber as the *x*-axis and absorption or scattering intensity as the *y*-axis, displaying characteristic absorption peaks and frequencies generated by different chemical bonds in the sample.[127] In recent years, *in situ* FTIR has gained increasing attention in the fields of energy, environment, and catalysis. Particularly in the field of electrocatalysis, this technique is highly valued because of its ability to observe the changes in materials during catalytic processes by applying different potentials, enabling further analysis of the catalytic mechanisms. *In situ* FTIR offers significant advantages over other techniques in studying the microstructure of materials, reaction activity, and investigating reaction mechanisms.[128–130]

While there are many effective ORR catalysts available, further research is needed to enhance catalyst selectivity. In this regard, researchers can utilize the FTIR technique to investigate the reaction process, which is crucial for the design of highly efficient catalysts.[131] The key step in the transition of molecular O_2 to water involves the cleavage of the O–O bond, facilitated by strong adsorption at the active site and charge polarization on the catalyst surface. If O–O cleavage is limited, the ORR proceeds *via* the two-electron pathway to generate hydrogen peroxide. To elucidate the mechanism better, Peter *et al.* employed FTIR spectroscopy to identify the stretching frequencies of different intermediates formed during the ORR process.[131] As shown in Fig. 4A, special peaks corresponding to the adsorbed O_2 molecule and its O–O stretching modes are present around 1429 cm^{-1} and 1080 cm^{-1}, respectively. The peak at 1270 cm^{-1} appears slowly with increasing time, indicating the bending mode vibration of adsorbed *OOH on the catalyst surface. Besides, the peak position corresponding to the O–O stretching mode of the adsorbed O_2 shifts with increasing time, suggesting a change in the strength of the O–O bond during the ORR process (Fig. 4B). The transfer of electrons from Pd back to the O_2 active site weakens the O–O bond, as evidenced by the decrease in the wave number at 200 seconds. Weaker O–O bonds facilitate easier O–O breaking and favor the four-electron transfer mechanism of the ORR. After a certain period, fresh O_2 molecules adsorb on the metal surface, and the same wave number is observed after 250 s, indicating the optimal M–O bond; for details, refer to Fig. 4C and D. In

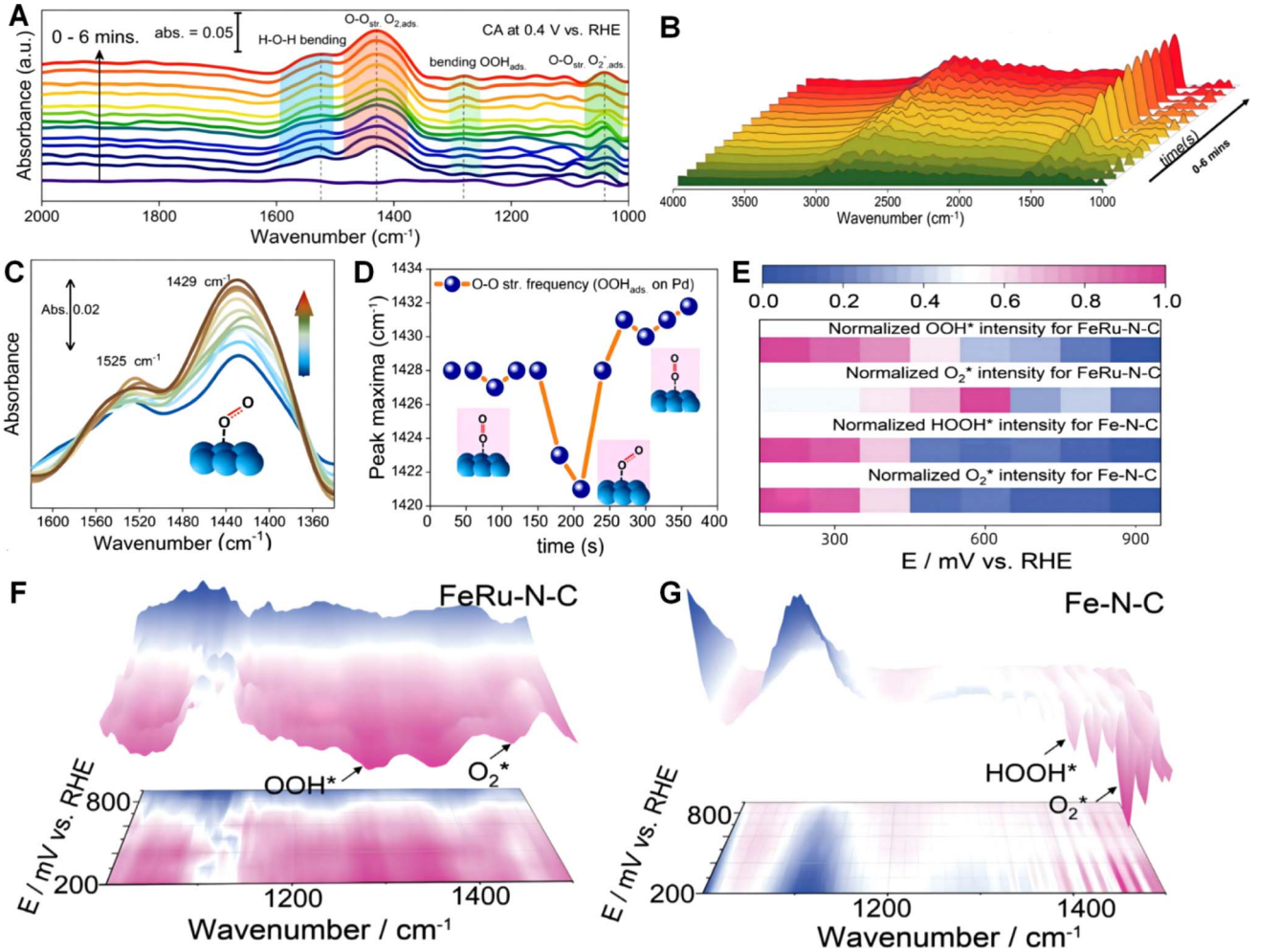

Fig. 4 (A) Comparison of the peak maxima position shifting with time. (B) *In situ* IR spectra showing water formation during the ORR. (C) Zoomed-in peaks around 1400 cm^{-1}. (D) Comparison of the peak maxima position shifting with time. Reproduced from ref. 131 with permission. Copyright 2022, American Chemical Society. (E) O_2, OOH* and HOOH* infrared peak intensity. (F) Three-dimensional *operando* ATR-FTIR on Fe–N–C and (G) FeRu–N–C in oxygen saturated 0.1 M $HClO_4$. Reproduced from ref. 132 with permission. Copyright 2024, Elsevier.

addition to the analytical methods discussed in the previous section, quantitative analysis of the entire catalytic process can also be conducted through infrared spectroscopy, as demonstrated in Fig. 4F and G.[132] The authors initially perform *in situ* attenuated total reflection (ATR) surface-enhanced infrared absorption spectroscopy on the material. By quantifying the infrared peak intensities of O_2, *OOH, and *HOOH across the entire potential range, the study revealed that the catalyst exhibited a high reaction rate, particularly in the low potential region. The low coverage of adsorbed oxygen also indicates efficient acidic ORR kinetics, providing further insights into the reaction mechanism (Fig. 4E). This further highlights the importance of *in situ* FTIR in understanding the catalytic mechanism and processes at a microscopic level, aiding experimental researchers in better understanding the catalysis in the microcosm.

4.3 Raman spectroscopy

In situ Raman spectroscopy serves as a real-time analytical technique for monitoring chemical reactions and physical changes at the surface or interface of materials.[133–135] Unlike traditional Raman spectroscopy, *in situ* Raman spectroscopy investigates structural and physical changes by altering conditions such as temperature, pressure, and voltage.[136,137] In *in situ* Raman experiments, the Raman laser irradiates the sample through an optical system and interacts with the sample through scattered light. The vibrations of molecules and the lattice of the sample cause Raman scattering, producing a Raman scattering spectrum. By measuring the frequency and intensity of the scattered light, information about different chemical bonds or the physical properties of the sample, such as molecular structure, lattice deformation, stress, and phase transitions, can be obtained. *In situ* Raman technology has played an important role in various fields, including catalysis, electrochemistry, battery research, and materials science.[138–140] It can reveal the kinetics and mechanisms of chemical reactions, monitor changes in catalysts, evaluate the electrochemical performance of materials, and study interfacial reactions in batteries. Additionally, *in situ* Raman can be applied to investigate the dynamic processes occurring at solid surfaces and interfaces, such as adsorption, corrosion and dissolution (Fig. 5A). The advantages of *in situ* Raman lie in its ability to provide real-time, non-destructive, and sample-handling-free analytical capabilities. It allows for direct observation of changes in the molecular structure of materials during reactions, and real-time tracking of the progress of chemical reactions or physical changes. Moreover, *in situ* Raman can be combined with other techniques, such as surface-enhanced Raman spectroscopy (SERS) and *in situ* electrochemistry, to further extend its analytical capabilities and application range.[142,143]

For instance, Kaito Homma's research involves the construction and thermochemical conversion of an FePc model catalyst, as well as *in situ* Raman spectroscopy studies of an Fe–N–C catalyst for the ORR, enabling the identification, comparison, and decoupling of multiple coexisting active sites and providing important insights into their pH-dependent activity and corresponding ORR mechanisms.[97] As depicted in Fig. 5B, under alkaline conditions, a superoxide ($*O_2^-$) is determined to be a common key intermediate of the Fe–N_x active sites (for both molecular FePc and thermochemical Fe–N–C), suggesting a non-concerted proton-electron transfer process with the protonation of $*O_2^-$ as the rate-determining step. In contrast, the chemical adsorption of O_2 may constitute the rate-determining step under acidic conditions, where no ORR was immediately detectable (Fig. 5C). *In situ* Raman spectroscopy of the model FePc catalyst reveals the distinct structural switching behaviors of the FeN_4 active sites under different pH conditions. Under alkaline conditions, the spontaneously formed axial hydroxyl ligand at the iron center can stabilize the planar structure. These results provide important insights into the pH-dependent ORR activity/stability of Fe–N–C electrocatalysts. In contrast to previous constant current or constant potential tests, it is also possible to conduct Raman spectroscopy tests by applying varying voltages for a period of time during the testing process. The data obtained from this testing method allow for a more intuitive understanding of the relationship between voltage progression and intermediates. This approach simplifies the analysis of reaction mechanisms during the reaction process.

It is noteworthy that *in situ* infrared and *in situ* Raman technology are two complementary analytical methods, which can bring about many advantages when used in combination. Firstly, both *in situ* infrared technology and *in situ* Raman technology can provide non-destructive real-time monitoring. This means that during the preparation of materials, reaction processes, or operation of catalysts, the changes in the sample can be continuously observed without interfering with the experimental system or collecting offline samples. This real-time monitoring capability helps to reveal complex structural and kinetic processes.[144] Secondly, *in situ* infrared technology and *in situ* Raman technology enable high-sensitivity analysis, capable of detecting minute changes such as the occurrence of adsorbates, surface structure alterations, and variations in reactant and product concentrations. The high sensitivity of these techniques allows researchers to better understand key parameters including reaction mechanisms, catalytic activity, and selectivity.[145] Additionally, *in situ* infrared technology and *in situ* Raman technology provide rich chemical information. Infrared spectroscopy provides information about chemical bond types, bond lengths and bond strengths, while Raman spectroscopy offers insights into chemical bond vibrations and lattice vibrations.[146] By integrating these two techniques, researchers can achieve a more comprehensive and detailed description of the material structure and reaction kinetics.[147] Finally, the synergistic application of *in situ* infrared technology and *in situ* Raman technology contributes to result validation and supplementation. As these two techniques are based on different physical principles, they can mutually validate and complement each other. By comparing and cross-referencing the results of these two techniques, material structures and reaction characteristics can be more accurately determined. This significantly reduces the possibility of misinterpretations that arise from using a single method. For example, researchers have explored the complementarity of surface-enhanced

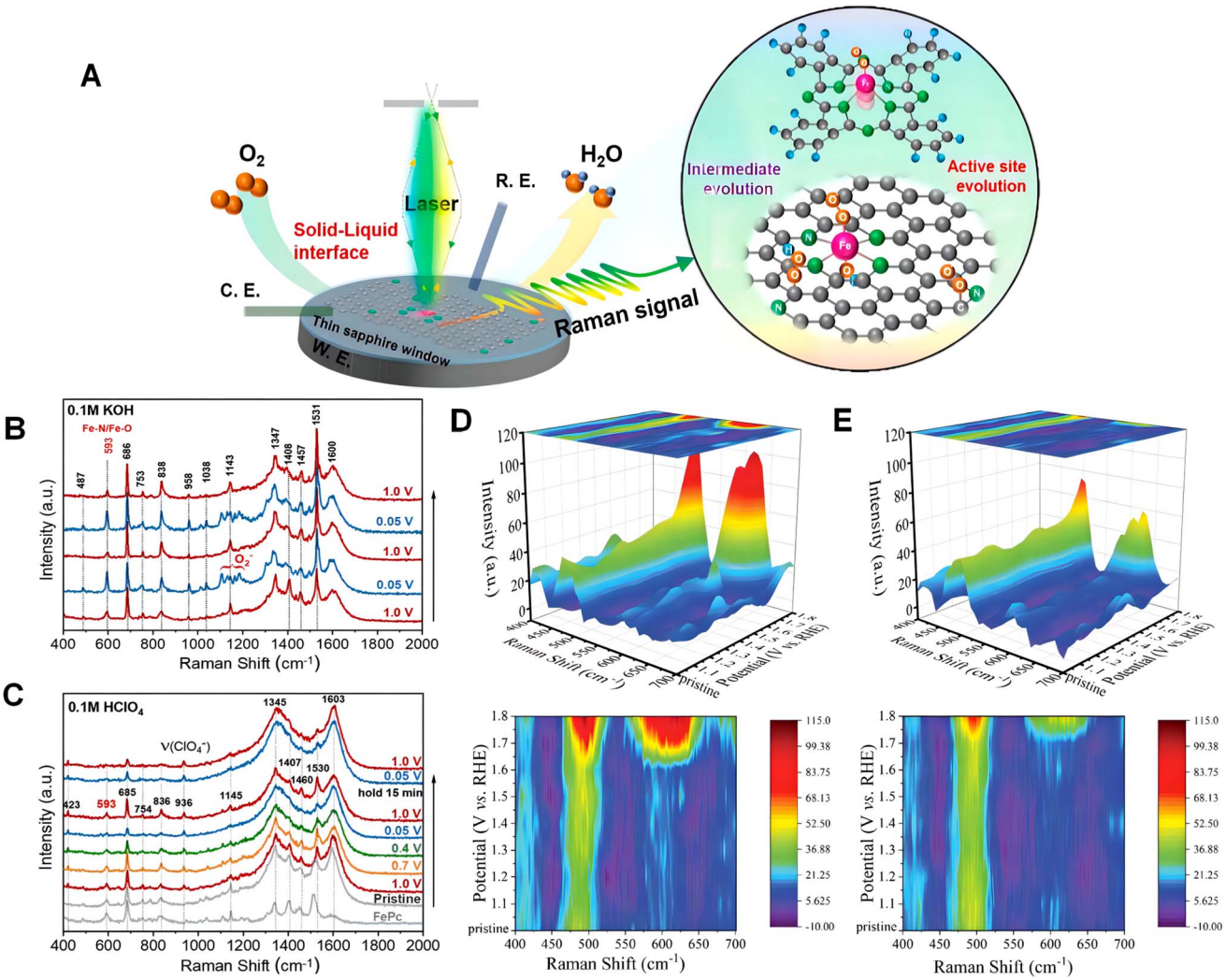

Fig. 5 (A) *In situ* Raman spectroscopy of molecular FePc as a model catalyst and pyrolyzed Fe–N–C catalysts during ORR electrocatalysis. (B) and (C) *In situ* Raman spectroscopy of FePc/C during the ORR in acidic solution and alkaline solution collected with 10 min time intervals. Reproduced from ref. 97 with permission. Copyright 2022, American Chemical Society. (D) *In situ* Raman spectra of F–Fe–CoP (top) and mapping (down). (E) *In situ* Raman spectra of CoP (top) and mapping (down). Reproduced from ref. 141 with permission. Copyright 2023, Wiley-VCH GmbH.

infrared absorption spectroscopy (SEIRAS) and SERS in studying the adsorption behavior of CO on various metal surfaces and its electrochemical reduction process. These studies discovered that infrared and Raman spectroscopy can detect different adsorbates, especially on weakly adsorbing surfaces. This is attributed to the different sensitivities of these techniques to the adsorbate dipole moments and polarizabilities, leading to mismatches in the infrared and Raman intensities when CO is adsorbed at different sites.[148] The above findings indicate the essential and complementary roles of both infrared and Raman spectroscopy techniques in detecting reaction intermediates, offering a more comprehensive understanding of catalytic processes. This is particularly important in the study of reaction mechanisms, intermediates, reaction pathways, electron transfer, and other aspects related to the ORR, providing more informative insights into complex catalytic reactions.[149]

4.4 X-ray absorption spectroscopy

X-ray Absorption Spectroscopy (XAS) is a widely used technique in materials science and chemistry for probing the electronic and structural properties of atoms within a sample. It involves the measurement of the absorption of X-rays by the sample as a function of X-ray energy.[150] XAS can provide valuable information about the local atomic environment, oxidation state, coordination geometry, and electronic structure.[151] XAS experiments are typically performed using synchrotron radiation sources, where the intense and tunable X-ray beams are crucial for obtaining high-quality spectra. The two main types of XAS techniques are X-ray absorption near edge structure (XANES) and extended X-ray absorption fine structure (EXAFS). In XANES, the X-ray energy is scanned within a particular energy range around the absorption edge of the target element.[152,153] The resulting XANES spectrum provides insights into the electronic state, oxidation state, and coordination environment of

the absorbing atom. XANES can be used to study various elements, including transition metals, light elements, and heavy elements. EXAFS, on the other hand, focuses on the fine structure oscillations beyond the absorption edge, which arise due to the X-ray scattering by neighboring atoms in the sample. The resulting EXAFS spectrum provides information about the bond distances, coordination numbers, and Debye–Waller factors of the absorbing atom, making it valuable for detailed studies of local structures around specific elements in a material.[154] Overall, XAS is a powerful technique for analyzing the atomic and electronic structures of materials, and it has applications in various fields, including catalysis, energy storage, materials science, and environmental science.[155–157]

For example, a study aims to investigate the enhanced activity of Cu–Se DAs utilizing *operando* XAS to monitor the electronic and atomic evolution of Cu sites under realistic operating conditions.[158] The operando XANES spectra of Cu–Se DAs at the Cu K-edge under different apply voltages are recorded in Fig. 6A. The changes in the Cu site's local coordination environment can be attributed to the adsorption of the *OOH intermediate, as identified by *in situ* SRIR. The combination of *operando* XAS and *in situ* SRIR results provides in-depth insights into the synergistic catalysis and electronic modulation between Cu and Se sites. Building upon this foundation, monitoring the changes in the crystal structure and fine structure at different potentials by applying varying voltages is more conducive for researchers to study the catalytic systems. As shown in Fig. 6B and C, researchers conduct tests at different voltages to quantitatively analyze the changes in the Co oxidation state. The subsequent EXAFS analysis of variations in Co–Co and Co–N/O bond lengths provided further insights into the relationship between structural changes and the reaction process in catalysis. By further processing the data and using the wavelet transform (WT), the coordination environment of Cu K-edge at different potential also was observed (Fig. 6D). In contrast to the previous methods, wavelet analysis, as depicted in Fig. 6E, focuses more on phase transitions. For example, the transformation of Co-based MOFs to CoOOH during the alkaline OER process is reflected in the wavelet analysis as the emergence of a new phase.

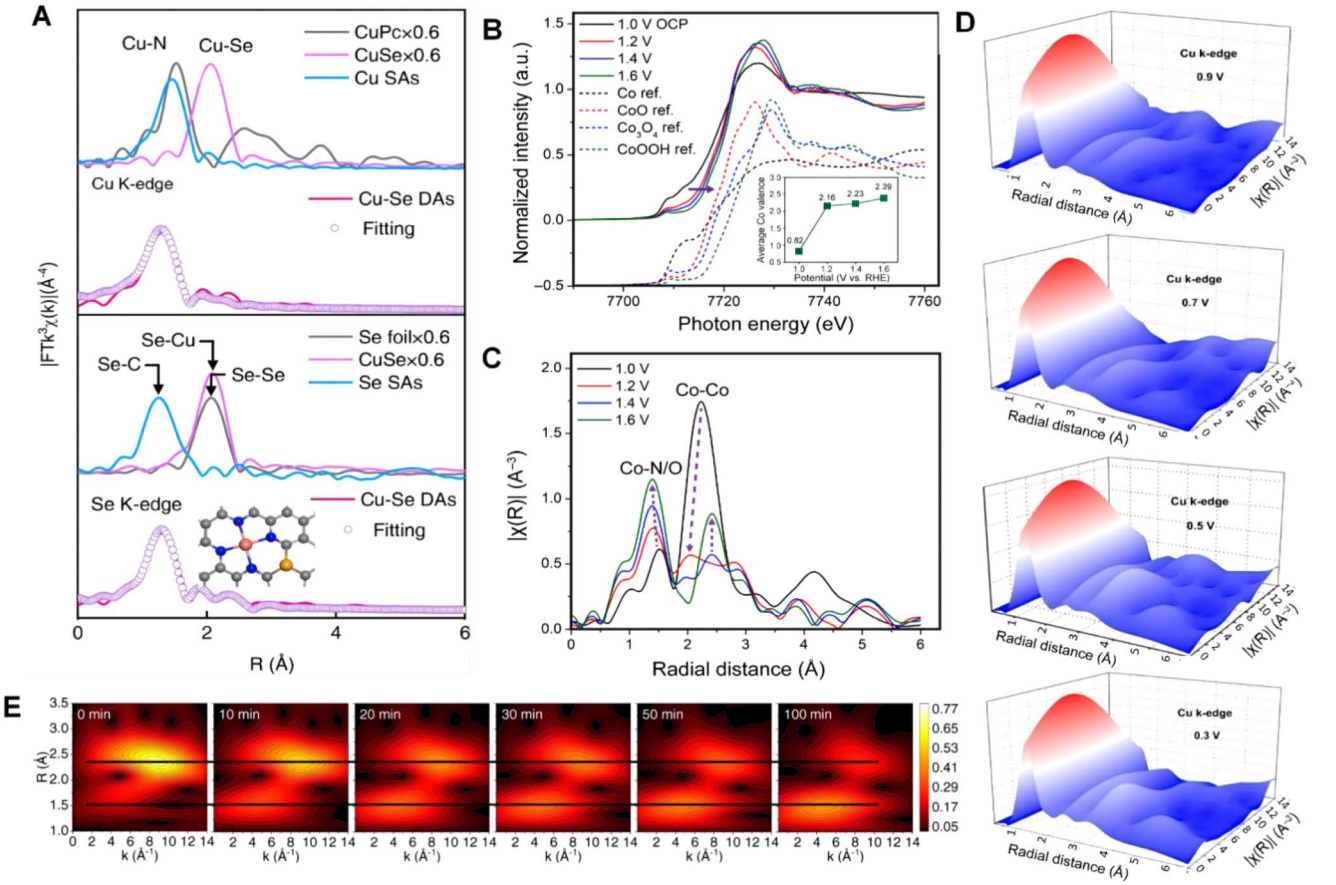

Fig. 6 (A) Fourier-transform EXAFS and fitting curves of Cu–Se DAs and controlled references at Cu and Se K-edges. Reproduced from ref. 158 with permission. Copyright 2023, Wiley-VCH GmbH. (B) and (C) *Operando* XANES spectra of Co_3N/C in a steady state at 1.0 V (OCP), followed by applied oxidative potentials from 1.2 to 1.6 V *vs.* RHE, and comparison with XANES reference spectra (a Y-offset of 0.5 was applied to better show the differences). Reproduced from ref. 159 and 160 with permission. Copyright 2021, American Association for the Advancement of Science. (D) WT contour plots of the Cu K-edge in R space at 0.9–0.3 V *vs.* RHE. Reproduced from ref. 161 with permission. Copyright 2022, Wiley-VCH GmbH. (E) Wavelet analysis of the RRCN sample in *in situ* EXAFS states. Reproduced from ref. 162 with permission. Copyright 2023, Nature Publishing Group.

5 ORR catalyst design

In recent years, there has been rapid development in ORR catalysts. Transition metal catalysts, single-atom catalysts, and carbon-based catalysts developed by researchers now exhibit performance comparable to that of platinum-based catalysts (Fig. 7). This achievement holds significant importance for reducing the use of precious metals and catalyzing commercialization. Furthermore, as mechanistic studies progress, various tuning methods have been proposed to enhance catalyst performance while ensuring stability, thus improving selectivity. Some recently representative catalysts are summarized in Tables 1 and 2.

Table 1 Two-electron ORR catalyst

Catalyst	Electrolyte	Selectivity (%)	Stability	Ref.
$ZnO@ZnO_2$	0.1 M K_2SO_4	95.5	550 cycles	169
NiB_2	0.1 M KOH	99	12 h	170
Co–N/HPC	0.1 M KOH	95	10 h	171
Co HSACs	0.1 M KOH	95	25 h (300 mA cm^{-2})	172
NBO-GQDs	0.1 M KOH	90	12 h	173
ZnCo-ZIF	0.1 M KOH	99	2 h	174
GDYs	0.1 M KOH	95	10 h	175
PD/N–C	0.1 M $HClO_4$	99	10 h	176
$BP/CoSe_2$	0.5 M H_2SO_4	90	5 h (54 mA cm^{-2})	177
PFC-72-Co	0.1 M $HClO_4$	90	4 h	178
F/S-CFs	0.1 M $HClO_4$	99.1	10 h	179
CoIn–N–C	0.1 M $HClO_4$	90	20 000 cycles	21
$PdSe_2$NPs	0.1 M $HClO_4$	95.8	10 h	180

5.1 Two-electron ORR catalysts

The design of two-electron ORR catalysts is an important research direction in the field of electrocatalysis.[195] Several strategies have been proposed for the design and optimization of two-electron ORR catalysts.[196] One approach involves the use of non-precious metal catalysts, which can significantly reduce costs and improve the overall sustainability of electrochemical systems. This includes the development of transition metal-based catalysts such as metal–nitrogen–carbon (M–N–C), metal–phosphorus–carbon (M–P–C), and metal–sulfur–carbon (M–S–C) materials.[197,198] These catalysts often exhibit high catalytic activity towards the ORR and demonstrate two-electron selectivity, which is essential for efficient energy conversion. Another strategy involves manipulating the electronic structure of the catalyst to optimize ORR kinetics. This can be achieved by controlling doping or modifying the catalyst surface and introducing specific elements or functional groups to adjust the electronic properties and enhance oxygen adsorption and activation.[199,200] For example, introducing nitrogen, sulfur, and phosphorus into the carbon framework can create active sites that promote the ORR process. Additionally, the design of hierarchical porous structures and controlled morphologies can improve the mass transfer and accessibility of reactants to active sites. This can enhance the catalytic performance of two-electron ORR catalysts.[201,202] Furthermore, advancements in theoretical modeling and computational simulations play a crucial role in guiding the design of two-electron ORR catalysts. These methods provide valuable insights into reaction mechanisms and enable the screening and prediction of potential candidate catalysts with enhanced activity and selectivity.

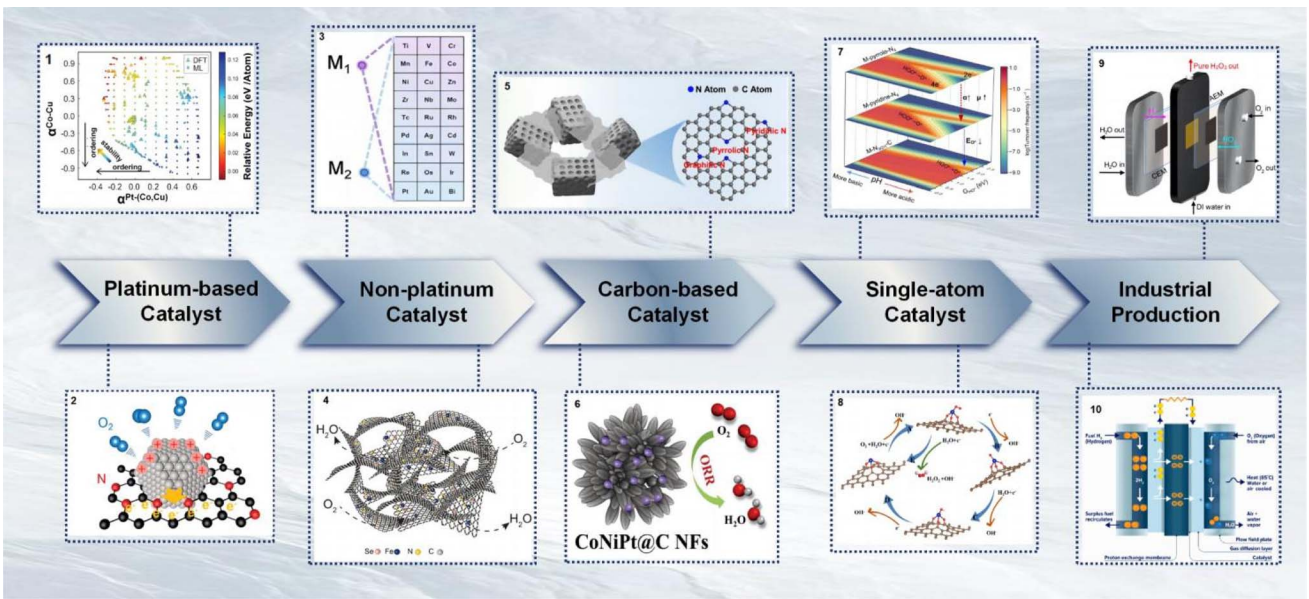

Fig. 7 Modern-developed ORR catalyst. Reproduced from ref. 39, 43, 163–165 and 166–168 with permission. Copyright 2024, Nature Publishing Group, with permission. Copyright 2023, Nature Publishing Group, with permission. Copyright 2022, Nature Publishing Group, with permission. Copyright 2021, Nature Publishing Group, with permission. Copyright 2021, Wiley-VCH GmbH, with permission. Copyright 2024, Wiley-VCH GmbH, with permission. Copyright 2023, Wiley-VCH GmbH, and with permission. Copyright 2024, American Chemical Society.

Table 2 Four-electron ORR catalyst

Catalyst	Electrolyte	Half-wave potential	Stability	Ref.
Fe–B–Co/NC	0.1 M KOH	0.891	5 h	181
OHEA-mAC	0.1 M KOH	0.9	10 000 cycles	182
Pt@Pt–Pt_3Ni	0.1 M $HClO_4$	0.9	50 000 cycles	183
Meso-/micro-FeNSC	0.1 M KOH	0.91	200 h	184
Zr–Zr_3O/NC	0.1 M KOH	0.914	20 000 cycles	185
K–N–C	0.1 M KOH	0.908	10 000 cycles	186
S–Cu-ISA/SNC	0.1 M KOH	0.918	50 h	187
N–Pt/HEA/C	0.1 M $HClO_4$	0.924	100 h	188
FeSA/N,S-PHLC	0.1 M KOH	0.91	882 h	189
FeMo–N_6	0.1 M $HClO_4$	0.84	0.27 h	190
Fe SAC-MOF-5	0.5 M H_2SO_4	0.83	10 000 cycles	191
FeSAs/NSC-vd	0.1 M KOH	0.92	13.8 h	192
Mf-pClNC	0.1 M KOH	0.91	100 000 cycles	193
FeRu–N–C	0.1 M $HClO_4$	0.86	50 000 cycles	194

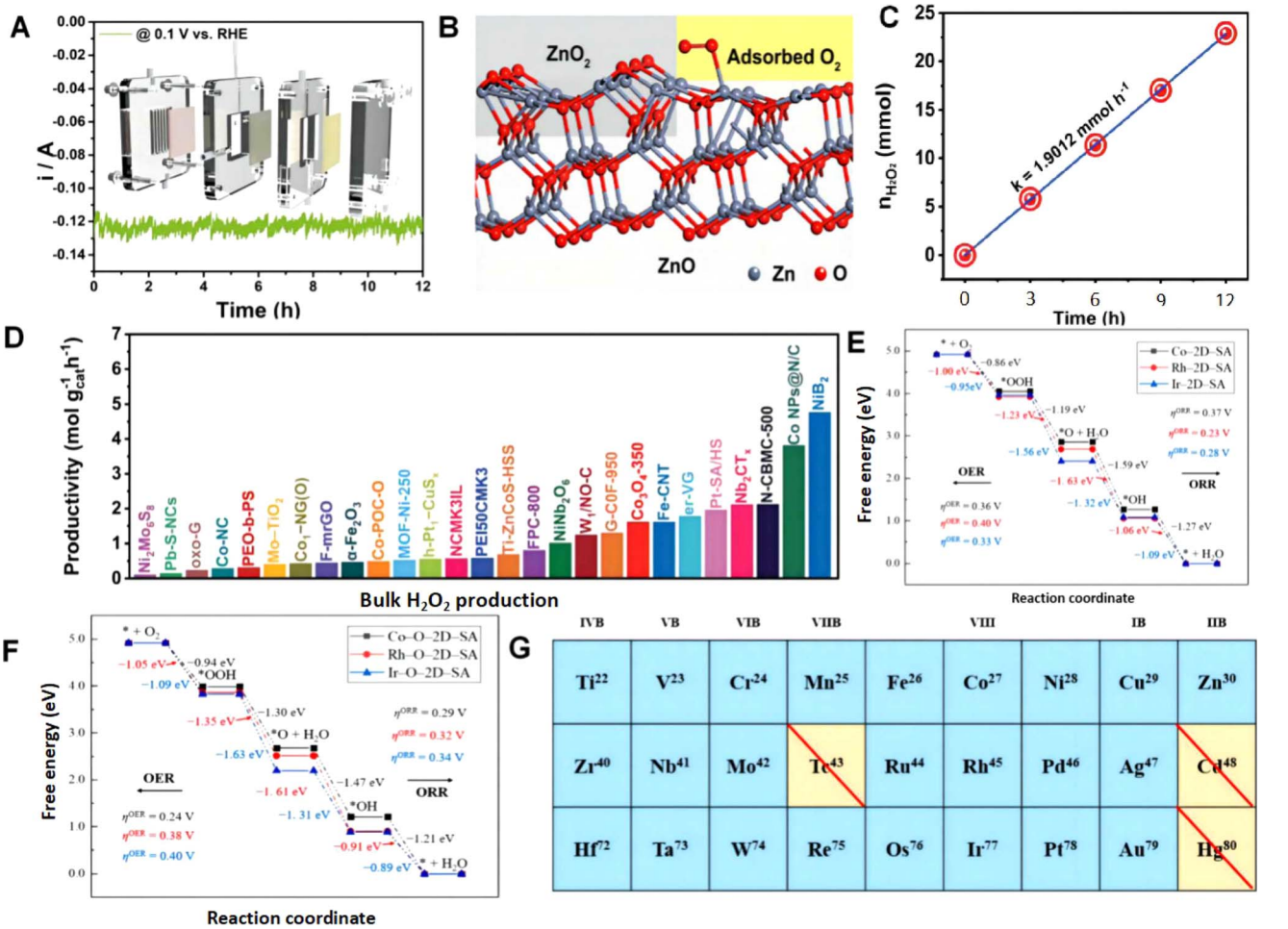

Fig. 8 (A) *I*–*T* curves of ZnO@ZnO_2 @ 0.1 V *vs.* RHE. (B) Adsorption model of O_2 molecules on ZnO@ZnO_2. Reproduced from ref. 169 with permission. Copyright 2023, Royal Society of Chemistry. (C) Moles of H_2O_2 generated by NiB_2 as a function of electrolysis time under the condition of continuous O_2 in the gas diffusion electrode. (D) Comparison of bulk H_2O_2 production of NiB_2 with previously reported electrocatalysts. Reproduced from ref. 170 with permission. Copyright 2022, Wiley-VCH GmbH. Gibbs free energy plots of the ORR and OER on (E) Co–, Rh–, and Ir–2D–SA as well as (F) Co–, Rh–, and Ir–O–2D–SA. (G) Considered transition metals for the calculation of ORR and OER performance. Reproduced from ref. 203 with permission. Copyright 2021, Elsevier.

5.1.1 Transition metal catalysts. Zn is commonly used in various catalytic reactions. A ZnO@ZnO_2 catalyst is synthesized by *in situ* growth of ZnO_2 octahedra on the ZnO (101) crystal surface.[169] As depicted in Fig. 8A, this catalyst exhibits close to 100% selectivity towards H_2O_2 production during O_2 reduction, with a high yield of 5.47 mol g_{cat}^{-1} h^{-1} at 0.1 V *vs.* RHE and a faradaic efficiency of 95.5%. Experimental tests and DFT calculations confirmed that Zn atoms at the heterogeneous interface act as active sites. Benefiting from the specific chemical environment of adjacent ZnO and ZnO_2, these Zn atoms can lower the *OOH and *O binding energies, thereby promoting excellent two-electron ORR activity, refer to Fig. 8B. This study reveals the surface structure of transition metal oxide electrocatalysts and the real active sites during operation and achieves a green and sustainable H_2O_2 synthesis process. Besides single transition metal catalysts, doping with heteroatoms or other transition metals is also a very effective tuning method. This is attributed to the interactions between metal atoms, which provide a richer array of active sites. The catalyst obtained several amorphous nickel boride (NiB_2) nanosheets with different electronic structures by varying the composition ratio between Ni and B.[170] Active studies show that optimized NiB_2 is an efficient electrocatalyst for the electrochemical reduction of O_2 to H_2O_2, providing close to 99% maximum selectivity at 0.4 V *vs.* RHE and over 93% H_2O_2 selectivity over a wide potential range of 0.2 to 0.6 V *vs.* RHE. Remarkably, even after continuous testing at 0.4 V *vs.* RHE for 12 hours, the activity remains stable with negligible current loss. Impressively, when applied to a gas diffusion electrode, a sustained H_2O_2 production rate of 4.753 mol g_{cat}^{-1} h^{-1} was achieved, stable for at least 12 hours, with approximately 93% high faradaic efficiency, refer to Fig. 8C, and the performance exhibited by these catalysts ranks at the top among similar catalysts, refer to Fig. 8D for details. Further *in situ* and *ex situ* studies combined with computational analysis revealed that the electronic structure of the amorphous NiB_2 phase not only has a close-to-optimal ΔG_{*OOH} value but also reduces the electron transfer capability of the surface, thereby enhancing catalytic activity and selectivity. The findings of this work not only establish amorphous NiB_2 as a new benchmark catalyst for alkaline two-electron ORR electrocatalysis but also provide new mechanistic insights and rational design strategies for economical, efficient, and stable transition metal (TM) electrocatalysts. As shown in Fig. 8E and F, researchers speculate that M-2D-SA and M-O-2D-SA (M = Co, Rh, and Ir) could also have potential catalytic activity for the ORR and OER, and they also systematically studied the catalytic activity of M-2D-SA and M-O-2D-SA (M = 3d, 4d, and 5d transition metals) for the ORR and OER using DFT calculations (Fig. 8G).[203] It is first demonstrated that most catalysts have good thermodynamic and electrochemical stability. Then, a strong scaling relationship between ΔG_{*OOH}, ΔG_{*O}, and ΔG_{*OH} was established for M-2D-SA and M-O-2D-SA, indicating that ΔG_{*OH} can serve as a good descriptor for activity. Consequently, volcano plots of η values *versus* ΔG_{*OH} were constructed for the ORR and OER, and characteristic descriptors are introduced to study the influence of intermediate free energies. These achievements provide theoretical support for M-2D-SA and M-O-2D-SA as dual-functional electrocatalysts for the ORR and OER.

It can be seen that with the development of two-electron ORR catalysts based on transition metals, researchers have gradually begun to develop and report catalysts composed of multiple transition metals. Transition metals possess abundant d-electron energy levels, enabling them to participate in electron transfer and structural changes in chemical reactions, thereby promoting catalytic reactions. These d-electron energy levels also endow transition metals with higher catalytic activity and selectivity.[204] Furthermore, transition metal catalysts exhibit tunability, allowing for the adjustment of catalytic activity and selectivity by changing the composition, structure, and surface properties of the transition metal. This tunability enables transition metal catalysts to adapt to different reaction conditions and substrate requirements, thereby improving catalytic efficiency and product quality. The modulation of electron transfer and selective changes is precisely what is needed for two-electron ORR catalysts. Therefore, investigating the correlation between the transition metal electronic structure and ORR selectivity is of utmost importance for catalyst design and the understanding of reaction mechanisms.[205] This research process requires advanced characterization techniques to help researchers gain a deeper understanding, and we also emphasize the importance of characterization techniques in research. Studying different types of metal combinations or using machine learning for combination screening remains a direction for further research in the future.[206,207]

5.1.2 Surface modified catalysts. A study reports on the edge effect of carbon-supported single-atom catalysts (SACs) on the pathway of the ORR, finding that the two-electron ORR is more favorable on edge-loaded Co–N_4 atomic sites compared to basal-loaded Co–N_4 atomic sites. DFT calculations show that the edge-loaded Co–N_4 atomic sites are thermodynamically more favorable for the two-electron ORR than the basal sites.[171] In Fig. 9A, atomically dispersed Co–N_4 motifs were immobilized on carbon substrates with different edge-to-volume ratios. When the Co–N_4 sites are fixed on hierarchical porous carbon (HPC), the obtained Co–N/HPC catalyst exhibited abundant edge-active sites and showed up to 95% selectivity for the two-electron ORR in alkaline media, while the basal Co–N_4 dominated graphene flakes (Co–N/GFs) show a four-electron pathway towards the ORR. Furthermore, in the subsequent stability tests, the catalyst maintained a high selectivity for hydrogen peroxide over a 10 hour testing period, refer to Fig. 9B for details. In addition to conventional single-atom modifications, catalysts featuring atomically dispersed atoms connected to the support through specific chemical bonds exhibit superior catalytic performance. This is attributed to the distinct presence of active sites and structures in such catalysts. Some researchers also focus on utilizing single-atom modification to enhance the selectivity for two-electron reactions.[172] They rationally develop highly efficient single-atom catalysts (HSACs) for the two-electron ORR through DFT prediction and experimental validation. In contrast to traditional metal-embedded SACs, the HSACs consist of atomically dispersed molecules, covalent bonds, and carriers, forming a well-defined active site structure

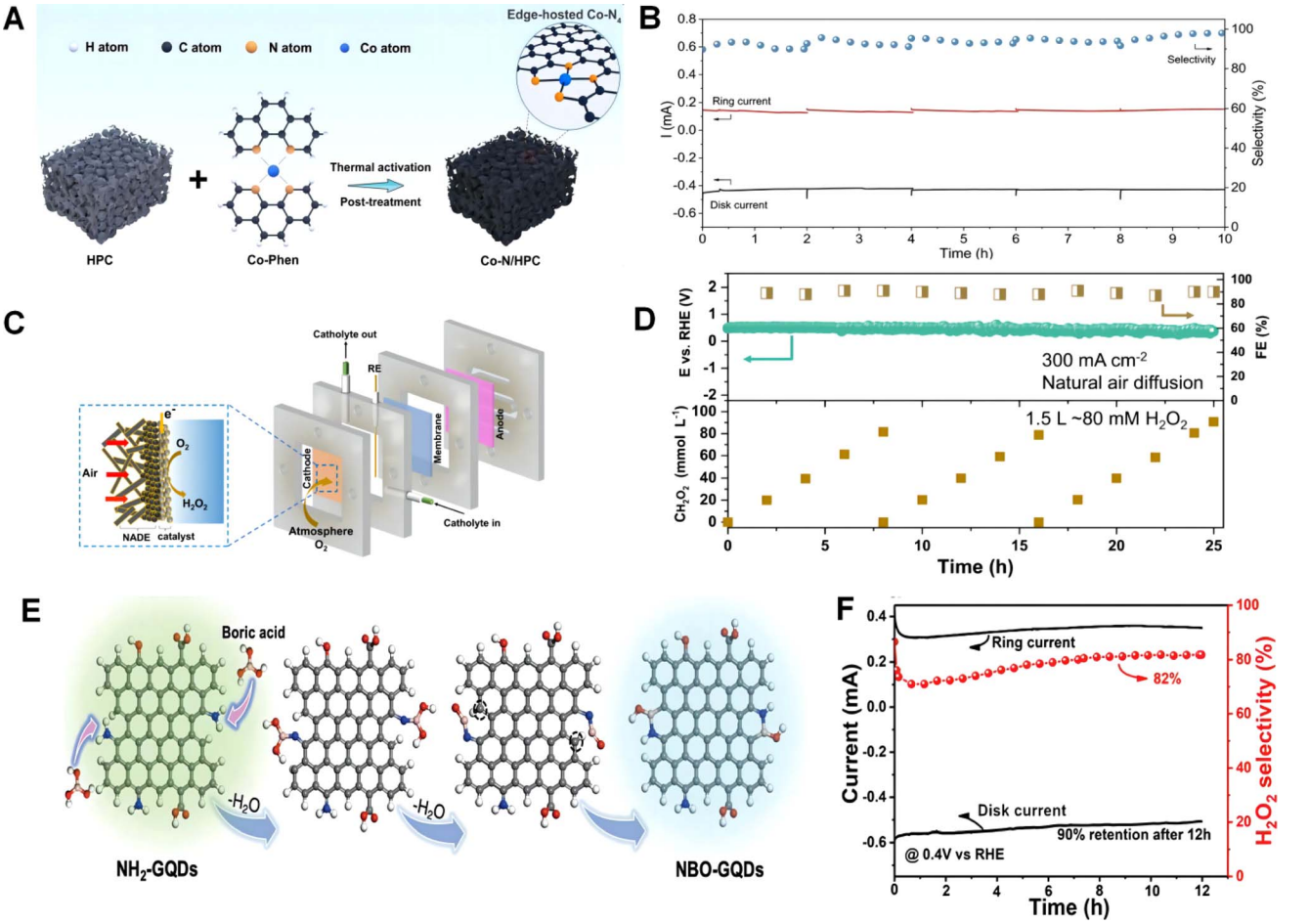

Fig. 9 (A) Schematic illustration of the fabrication procedure of the Co–N/HPC catalyst from hierarchically porous carbon (HPC) and Co-Phen. (B) Stability evaluation of Co–N/HPC *via* a chronoamperometric test at a fixed disk potential of 0.5 V *vs.* RHE of 0.5 V *vs.* RHE. Reproduced from ref. 171 with permission. Copyright 2022, Wiley-VCH GmbH. (C) Schematic illustration of the air-breathing flow cell configuration with natural air diffusion electrode. (D) Stability test of the Co HSACs under 300 mA cm^{-2} in 0.5 M KOH for practically producing 80 mM H_2O_2 solution. Reproduced from ref. 172 with permission. Copyright 2023, Nature Publishing Group. (E) Schematic of the synthesis of NBO-GQDs. (F) The stability test of NBO-G/CNTs at a fixed disk potential of 0.4 V *vs.* RHE. Reproduced from ref. 173 with permission. Copyright 2023, Wiley-VCH GmbH.

that correlates directly with their catalytic performance (Fig. 9C). DFT calculations play an important role in screening MPc candidate molecules and predicting the modulation of the heterogeneous electron structure by axial coordination pairs. In Fig. 9D, the catalyst exhibits up to 95% selectivity for the two-electron ORR and an onset potential of 0.85 V *vs.* RHE in H-cell experiments and could produce H_2O_2 at a current density of 300 mA cm^{-2}. In addition to single atoms, growing quantum dots on a support is also a way to modify the surface of the catalyst. The work involved the design and synthesis of N, B, OH-doped graphene quantum dots (NBO-GQDs) with a high density of N, B, OH groups, refer to Fig. 9E. NBO-GQDs were formed by functionalizing GQDs with NH_2 groups and reacting with H_3BO_3 to form a hexatomic heterocycle structure containing N, B, and OH.[173] In Fig. 9F, when NBO-GQDs are dispersed on a conductive carbon substrate and tested in a rotating disk electrode setup in alkaline solution, their selectivity for H_2O_2 exceeds 90% at potentials ranging from 0.7–0.8 V *vs.* RHE. After 12 hours of stability testing, the selectivity remains at 90% of the initial value. In a flow cell setup, the H_2O_2 production rate reaches 709 mmol $g_{catalyst}^{-1}$ h^{-1}, outperforming most reported carbon-based and metal-based electrocatalysts.

Surface modification can alter the surface properties of catalysts, such as electronic structure and types and quantities of active sites, thereby regulating the rate and selectivity of catalytic reactions. Moreover, surface modification can also alter the reaction mechanism of catalysts. The rate and selectivity of catalytic reactions depend on the adsorption, dissociation, and recombination processes of reactants on the catalyst surface. Surface modification can modify the energy barriers and rates of these steps, thereby controlling the reaction paths and product distributions of catalytic reactions. This is crucial for researchers to study and understand reaction mechanisms.[164] Just as in the aforementioned three studies, whether it is surface modification, development of edges as active sites, or utilization of single atoms to enhance two-electron selectivity, all of them cannot avoid the adjustment of the electronic

structure to alter the strength of adsorption of oxygen and its reaction intermediates.[208–211]

5.1.3 Pore regulation strategy. A ZnCo-ZIF nanocube electrocatalyst with a Zn : Co ratio of 9 : 1 and exposed {001} facets is prepared for the two-electron ORR (Fig. 10A).[174] Experimental results and DFT calculations indicate that H_2O_2 dissociation and the two-electron ORR pathway are more favorable kinetically than the four-electron ORR pathway, as shown in Fig. 10B. This is due to its unique cubic structure as well as its excellent pore structure. Moreover, compared to ZnCo-ZIF-R3 with {110} facets, the exposed {001} facets in ZnCo-ZIF-C3 are energetically favored for the two-electron ORR process. In Fig. 10C, the rational design of composition and morphology makes ZnCo-ZIF an excellent two-electron ORR electrocatalyst with a selectivity close to 100% and an H_2O_2 production rate of 4.3 mol g_{cat}^{-1} h^{-1}. This study provides a strategy for developing superior two-electron ORR catalysts through the modulation of structural morphology. A series of N/C catalysts with different pore structures but similar surface states or properties are prepared.[212] In Fig. 10D, using these reliable pore structure models, they investigated the effects of the Brunauer–Emmett–Teller specific surface area and micropore surface fraction on

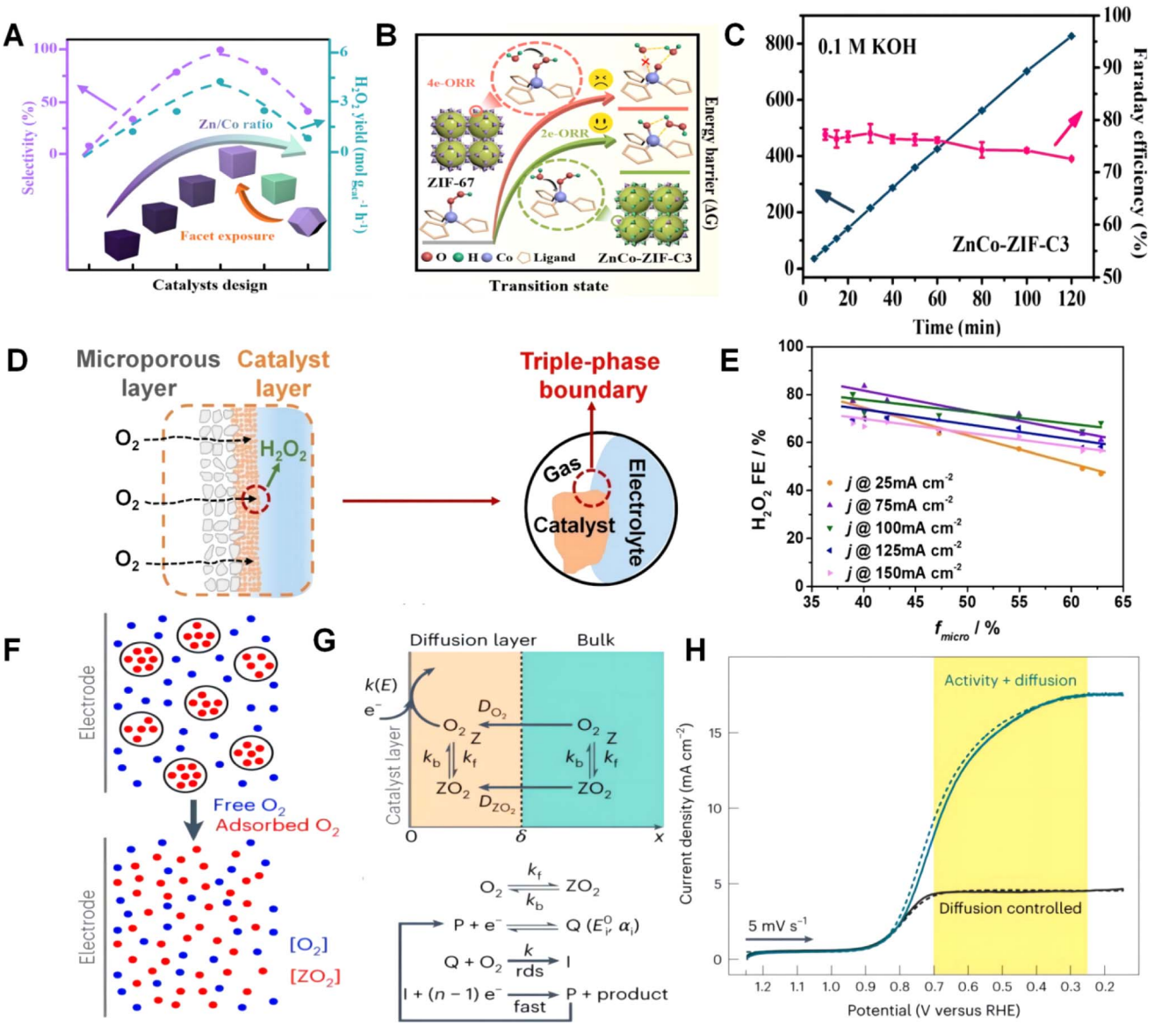

Fig. 10 (A) Two-electron ORR selectivity and H_2O_2 yield of ZnCo-ZIFs with different Zn/Co ratios and crystal facet exposure and (B) binding mode difference of water molecules in the transition states of two-electron and four-electron ORR routes. (C) H_2O_2 concentration *versus* time at a current density of 70 mA cm^{-2} in a neutral electrolyte. Reproduced from ref. 174 with permission. Copyright 2023, American Chemical Society. (D) Schematic depiction of the FC setup. (E) Plots of H_2O_2 FE against the micropore surface fraction under RRDE and FC test conditions, respectively, for N/C-*x*% CO_2 catalysts (*x*% in the range of 3–75%). Reproduced from ref. 212 with permission. Copyright 2022, Elsevier. (F) ORR catalytic electrokinetic model. (G) Reaction equations for electrodynamic modeling. (H) RDE voltammograms collected in O_2 saturated phosphate buffered aqueous solution at a scan rate of 5 mV s^{-1} and an electrode rotation rate of 1600 rpm. Reproduced from ref. 213 with permission. Copyright 2023, Nature Publishing Group.

ORR activity and selectivity in both RRDE and flow cell (FC) test systems. Their experimental results demonstrate that the influence of the pore structure on oxygen reduction activity is consistent in both RRDE and FC test systems. And the results show a positive correlation with the specific surface area. However, the impact of the pore structure on reaction selectivity is inconsistent at the RRDE and FC levels: at the RRDE level, the selectivity of the two-electron process is independent of micropore content, while at the FC level, the selectivity of the two-electron process shows a negative correlation with micropore content. The inconsistency is attributed to the different electrode motion states in the solution phase and working condition tests, as shown in Fig. 10E, leading to different residence times of the two-electron products in the micropores. This work reveals the impact of the pore structure on two-electron ORR activity and selectivity, which is helpful for the design of carbon-based catalysts for electrochemical synthesis of H_2O_2. The research confirms that a nanoporous crystal with hydrophobic internal surfaces and hydrophilic external surfaces can improve the ORR catalytic performance of Pt/C electrocatalysts by increasing O_2 supply refer to Fig. 10F.[213] The addition of an appropriate concentration of zeolite (6.7 vol%) leads to a 3.8–3.9-fold increase in ORR current in acidic and neutral electrolyte solutions, surpassing previously reported values, as shown in Fig. 10H. Their work focuses on utilizing microporous water to achieve high concentrations of gas in solution on the electrode, which may facilitate catalysis at enhanced current densities due to reduced mass transfer limitations, refer to Fig. 10G. This provides a platform for obtaining intrinsic catalytic properties over a wide potential range. This provides significant guidance for the design of ORR catalysts in terms of their structure.

The pore structure of catalysts has a significant impact on catalytic performance. Different pore structures can provide different lattice or surface sites, and this leads to distinct affinity and activity towards adsorbed reactants.[15] In addition, the pore structure morphology influences the mass transfer performance of catalysts.[214] During catalysis, reactants need to diffuse and transfer to active sites on the catalyst surface. The structure morphology can affect the pore structure and grain size of the catalyst, thereby influencing the mass transfer rate and effectiveness during catalytic reactions. Controlling mass transfer and adsorption strength is crucial for the study of ORR catalysts. Hence, utilizing machine learning or theoretical calculations to screen and design structures for efficient catalysts is a promising research direction in the future.[39,215,216]

5.2 Four-electron ORR catalysts

The successful development of efficient four-electron ORR catalysts holds significant importance for various applications, such as fuel cells and metal–air batteries. When designing four-electron ORR catalysts, several key factors need to be considered.[217,218] Firstly, the catalyst material must exhibit high activity towards the ORR. This can be achieved by incorporating transition metals or metal-containing compounds with desirable redox properties. Catalysts based on Pt or its alloys such as Pt-based nanoparticles or Pt-based core–shell structures have demonstrated excellent performance in the four-electron ORR due to their high catalytic activity.[219–221] Secondly, the catalyst material should have a large surface area to facilitate the electrochemical reaction. This can be achieved by utilizing nanomaterials such as nanoparticles or nanowires, which provide a high surface-to-volume ratio. The increased surface area enhances the interaction of the catalyst with oxygen, thereby promoting catalytic activity.[222] Furthermore, the catalyst material should exhibit good stability and long-term durability to endure the harsh conditions of electrochemical reactions. This can be accomplished by incorporating stabilizing agents or supporting the catalyst on robust materials such as carbon nanotubes or graphene. In addition to material considerations, the design of the catalyst's structure and morphology plays a critical role in enhancing its four-electron ORR activity. For instance, hierarchical or porous structures can facilitate improved mass transport and accessibility of reactants to the active sites, and this can enhance catalytic performance. Similarly, controlling the size, shape, and composition of the catalyst nanoparticles can also influence their electrochemical activity towards the four-electron ORR.[223] Overall, the design of an efficient catalyst for the four-electron ORR requires a multidisciplinary approach, integrating knowledge from materials science, electrochemistry, and catalysis. By carefully considering the aforementioned factors and continuously exploring novel materials and structural designs, it is possible to develop highly efficient and stable four-electron ORR catalysts, contributing to the advancement of clean energy technologies.

5.2.1 Heteroatom coordination modulation. The use of transition metals in two-electron catalysts and metals such as Fe and Co in four-electron catalysts is advantageous for stronger oxygen and intermediate adsorption. On one hand, the metals can enhance intermediate adsorption facilitates the occurrence of four-electron processes. On the other hand, in acidic environments, catalysts represented by Fe–N–C exhibit better activity. For example, a facile and scalable molten salt pyrolysis strategy for the preparation of Pt alloy-embedded M–N–C catalysts is proposed.[224] In this work, Pt alloy nanoparticles were embedded in N-doped graphene nanosheets, which also dispersed a large number of M–N_x active sites, refer to Fig. 11A. This adjustment effectively increases the electrochemical surface area, enhances mass transfer, and better promotes the reaction process. In Fig. 11B and C, the results show that the obtained low Pt catalyst exhibits a mass activity of 1.29 A mg_{Pt}^{-1} at 0.9 V *vs.* RHE and demonstrated excellent durability. Experimental and theoretical results validate the unique structure–activity relationship between the nanoalloy and M–N–C components, where their synergistic interactions promoted the enhancement of catalytic performance. Fe–N–C is a commonly encountered metal-heteroatom hybrid combination, where B, P, and S display properties similar to N and exhibit superior metal monomer binding compared to N. Researchers proposed a novel method of hetero-atomic pair coordination regulation, which directly solves the problem of inappropriate adsorption behavior of *OOH intermediates due to the symmetric coordination structure around the Fe site.[225] As a proof-of-concept experiment, engineered Fe catalysts (Fe–B–Co/NC) are

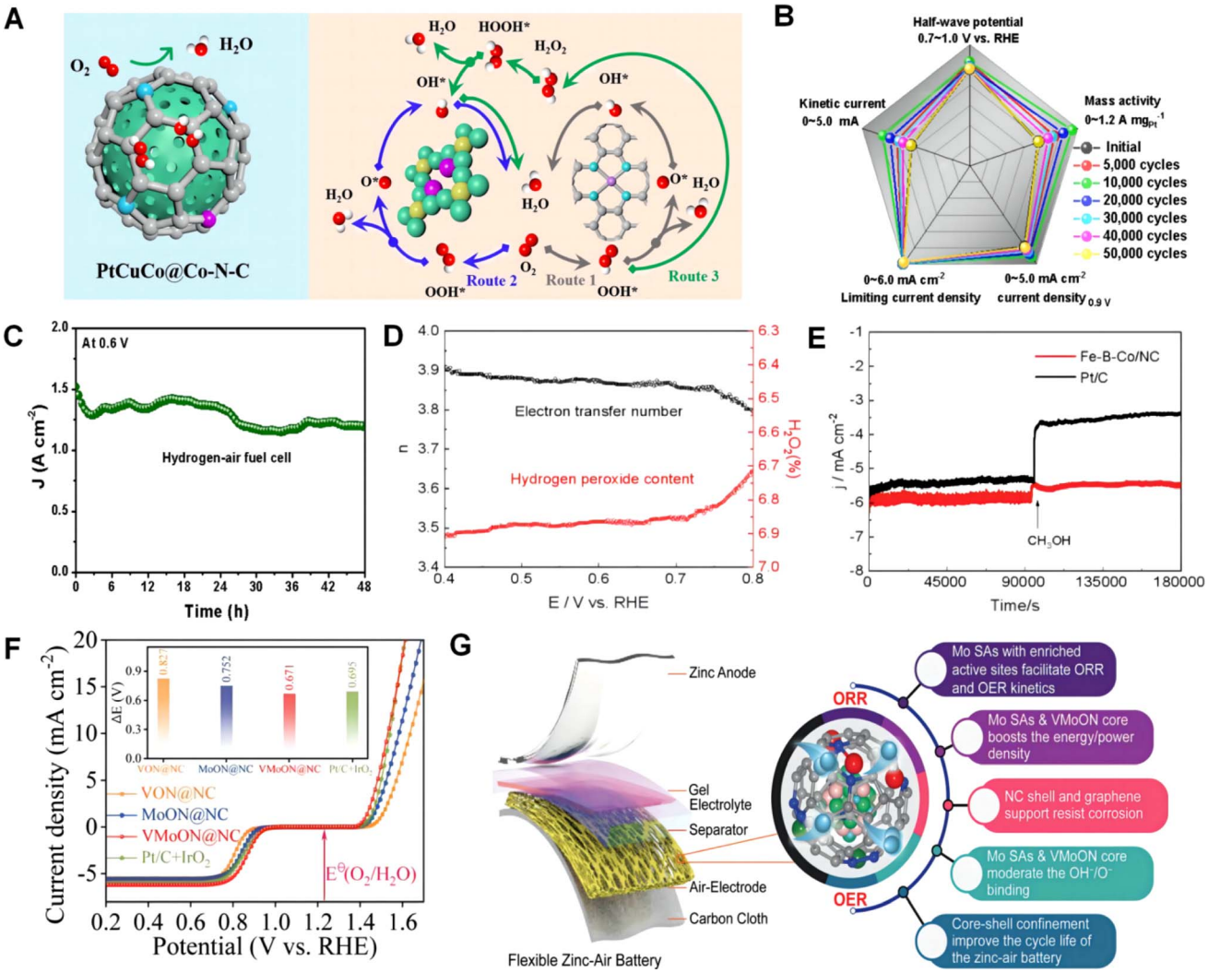

Fig. 11 (A) Schematic diagram of the ORR pathways of PtCuCo@Co–N–C. (B) Other activity changes of PtCuCo@Co–N–C before and after 50 000 cycles. (C) Stability test of a hydrogen–air fuel cell at a voltage of 0.6 V *vs.* RHE. Reproduced from ref. 224 with permission. Copyright 2021, Wiley-VCH GmbH. (D) The electron transfer number and hydrogen peroxide content of Fe–B–Co/NC during the reaction process. (E) Current time chronoamperometric responses of Fe–B–Co/NC and Pt/C. Reproduced from ref. 225 with permission. Copyright 2023, Wiley-VCH GmbH. (F) Overall polarization curves within the ORR and OER potential window of the as-obtained catalysts. (G) 3D superstructures with superior Mo anchoring and numerous electroactive sites are utilized to deliver an unprecedented peak power density in ZABs, along with a long cycle life. Reproduced from ref. 226 with permission. Copyright 2023, Wiley-VCH GmbH.

reported using a "heteroatom co-ligand coordination modulation" strategy, possessing asymmetric coordination and optimally filled anti-bonding Fe sites. *In situ* EIS and SR-FTIR techniques demonstrated that the optimized Fe sites could accelerate O–O bond dissociation of OOH, rapidly forming *O intermediates, thereby achieving efficient electrocatalytic ORR activity and pathways. The outstanding Fe–B–Co/NC catalyst exhibits excellent ORR catalytic activity with a half-wave potential of 0.891 V *vs.* RHE and an ultra-high mass activity of 12.26 A mg_{metal}^{-1}. In Fig. 11D, the Fe–B–Co/NC catalyst demonstrates the highest four-electron ORR pathway efficiency, reaching ≥ 93% for H_2O generation, as well as the excellent stability (Fig. 11E). This study proposes a strategy by simultaneously achieving the desired anti-bonding orbital electronic conditions and optimizing the adsorption strength of oxygen-containing intermediates. This work provides new insights for the design of future ORR catalytically active sites. Another way of adjustment is to replace metals for performance tuning. Metals such as Mo, Ce, and La exhibit high catalytic potentials compared to commonly used ORR metal catalysts like Fe and Co. Researchers reported a nano-sized (2.3 ± 0.6 nm) vanadium–molybdenum oxide encapsulated in a nitrogen-doped carbon shell, exhibiting the excellent ORR performance.[226] In the synthesis process, the core provides individual Mo atoms, which are anchored on the N-doping sites in the shell, resulting in Mo-based SACs exhibiting active OER sites in a pyrrolic-N environment and active ORR sites in a pyridinic-N environment, refer to Fig. 11G. Zinc–air batteries using these dual-functional Mo single-atom catalysts exhibit high power density (376.4 mW cm^{-2}) and a long cycling life of over 630 hours, significantly outperforming noble metal-based air batteries (Fig. 11F). Such single-atom catalysts hold promise in

addressing the poor performance of various metal–air batteries, significantly improving the kinetics of the ORR and OER.

From the above, it can be seen that selecting appropriate metal doping or combinations can achieve the development of efficient catalysts.[227] However, besides transition metals and noble metals, whether other metals also exhibit high selectivity and efficiency in four-electron ORR catalysis has been less studied. This provides a new direction for future researchers.[22,228,229]

5.2.2 Regulating structural morphology. Controlling the structural morphology of catalysts by starting with the selection of active center metals is an effective means of regulation, as mentioned in the preceding article. For example, catalysts designed with a conical shape are beneficial for the desorption and adsorption of products, or the sharp tip effect can be utilized to enhance catalytic performance. A simple strategy is employed to construct *in situ* ordered high-entropy alloy nanoparticles within a novel two-dimensional nitrogen-doped mesoporous carbon sandwich-like framework.[182] XRD analysis and atomic-resolution images from transmission electron microscopy confirmed the formation of a chemically ordered L_{12} phase in the high-entropy alloy, as shown in Fig. 12A. Experimental results and theoretical calculations demonstrated that the ordered-phase high-entropy alloy catalyst exhibits superior performance in the ORR compared to the disordered-phase high-entropy alloy. This is attributed to the ordered division of labor among the metal sites and the strong structural stability, which facilitated electron transfer and maintained the integrity of the catalyst structure before and after catalysis. In Fig. 12B and C, the ordered high-entropy alloy catalyst possessed a significantly high half-wave potential (0.90 V *vs.* RHE) and excellent durability (a degradation of only 0.01 V *vs.* RHE after 10 000 cycles). The results show that the performance of ordered high-entropy alloys is superior to that of disordered high-entropy alloys. A catalyst is designed and anisotropic mesoporous Pt@Pt–Pt_3Ni core–shell framework nanowires (CSFWs) are synthesized.[183] The mesoporous Pt@Pt–Pt_3Ni CSFWs combined the advantages of the 1D ultrafine atomic-scale serrated Pt nanowire (with a diameter of approximately 3 nm) core and 3D open Pt–Pt_3Ni framework shell

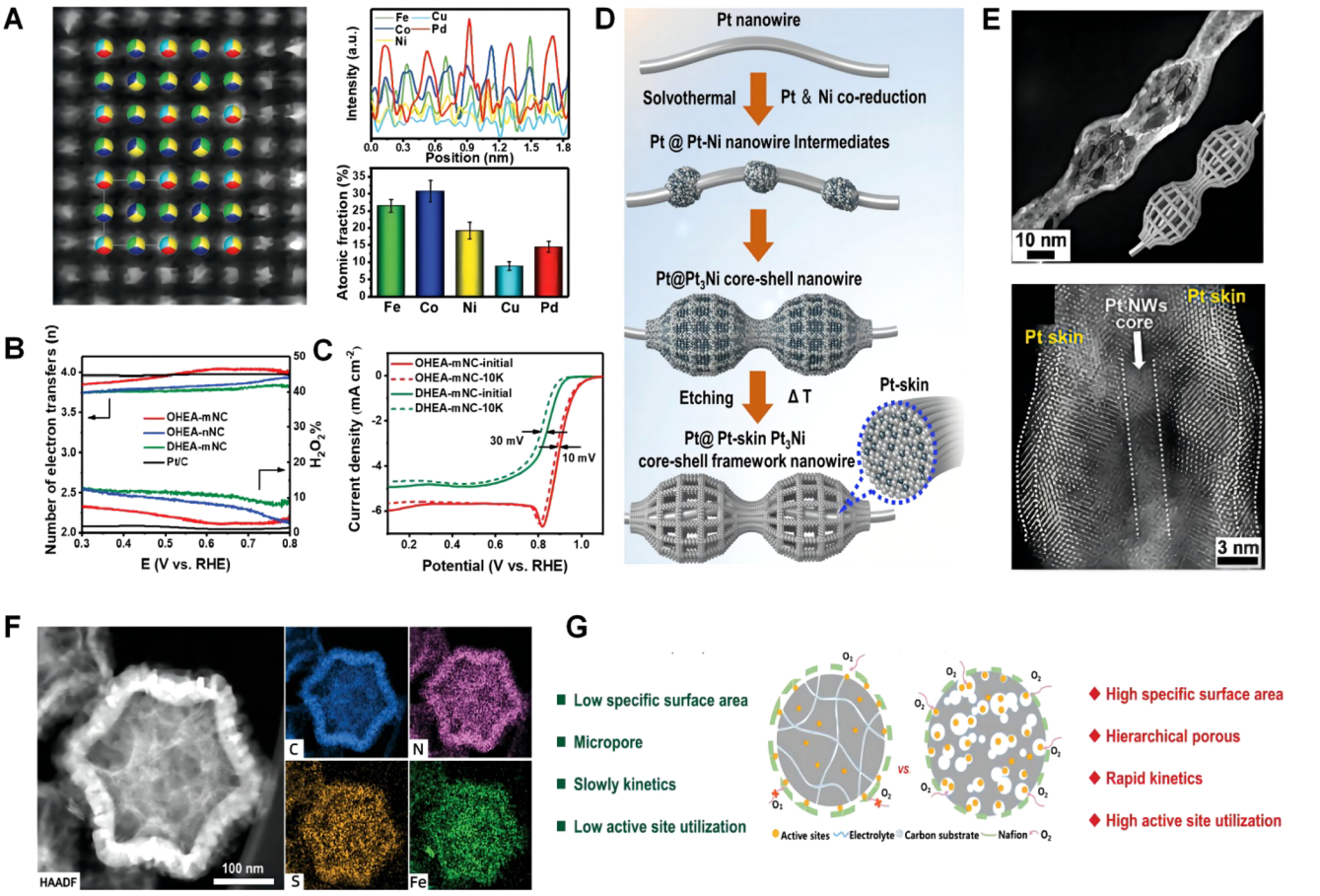

Fig. 12 (A) Schematic illustration of the chemical species on each site, superposed on the HAADF image along the [100] zone axis. (B) Electron transfer number (*n*) and H_2O_2 yield of electrocatalysts calculated from RRDE curves from 0.3 to 0.8 V *vs.* RHE. (C) Comparative ORR activities of OHEA-mNC and DHEA-mNC catalysts before and after 10 000 potential cycles. Reproduced from ref. 182 with permission. Copyright 2022, Wiley-VCH GmbH. (D) Schematic illustration of the preparation of mesoporous Pt@Pt_3Ni CSFWs. (E) HAADF-STEM and HRTEM images. Reproduced from ref. 183 with permission. Copyright 2023, Nature Publishing Group. (F) HAADF-STEM image and corresponding energy-dispersive spectroscopic elemental mapping (C, N, S, and Fe). (G) Schematic illustration of the effect of the lager specific surface area and hierarchical porous structure on the exposure of active sites and mass transfer. Reproduced from ref. 184 with permission. Copyright 2023, Wiley-VCH GmbH.

(with lattice strain), and the catalyst achieves high ORR activity, stability, and Pt utilization efficiency, refer to Fig. 12D. The mesoporous structure within the 3D open Pt–Pt_3Ni framework shell provided highly exposed surfaces, and this can maximize the utilization of Pt atoms and accelerate reactant transport, as shown in Fig. 12E. As anticipated, the mesoporous Pt@Pt–Pt_3Ni CSFW catalyst exhibits excellent electrocatalytic performance for the ORR in hydrogen fuel cell technologies. It demonstrates high mass activity (6.69 A mg^{-1}) and specific activity (8.42 mA cm^{-2} at 0.9 V *vs.* RHE). The catalyst also exhibits exceptional stability, with less than 3% activity degradation after 50 000 cycles. This is a nano-emulsion-induced polymerization self-assembly method to prepare hierarchical meso/microporous N/S co-doped carbon nanocages using atomically dispersed Fe–N_4 (meso/micro-FeNSC) as an efficient ORR nanoreactor, as shown in Fig. 12F.[184] The hierarchical meso/microporous structure, large specific surface area, and interconnect channels were crucial for maximizing the utilization of Fe–N_4 sites and ensuring rapid mass transfer, refer to Fig. 12G. This structure maximized the unique nanoscale architecture of Fe–N_4 sites, and meso/micro-FeNSC exhibited excellent electrocatalytic activity for the ORR, with a half-wave potential of 0.91 V *vs.* RHE, a kinetic mass-specific activity of 68.65 A g^{-1}, good four-electron selectivity, excellent methanol tolerance, and long-term durability. Moreover, zinc–air batteries based on meso/micro-FeNSC showed advantages such as high-power density, large capacity, and superior cycling stability, surpassing Pt/C catalysts.

As can be seen from the previous discussion, the so-called morphological structure aims to ultimately increase the specific surface area, enhance the interaction with oxygen, and further improve the reaction activity and four-electron ORR efficiency.[230] However, it does not necessarily mean that simply increasing the specific surface area is always beneficial for catalytic activity. Therefore, the key to designing catalysts lies in finding the optimal balance between the structure and catalytic performance. This may involve utilizing theoretical calculations or machine learning to screen for the optimal structure.[231–233]

5.2.3 Composite materials. In addition to the regulation of active centers and morphologies, the use of composite materials in the four-electron ORR has gained popularity among researchers in recent years. The combinations of organic and inorganic materials, carbon-based materials with cyanides, and metals with semiconductor materials have been explored to achieve synergistic effects and enhance catalytic performance.

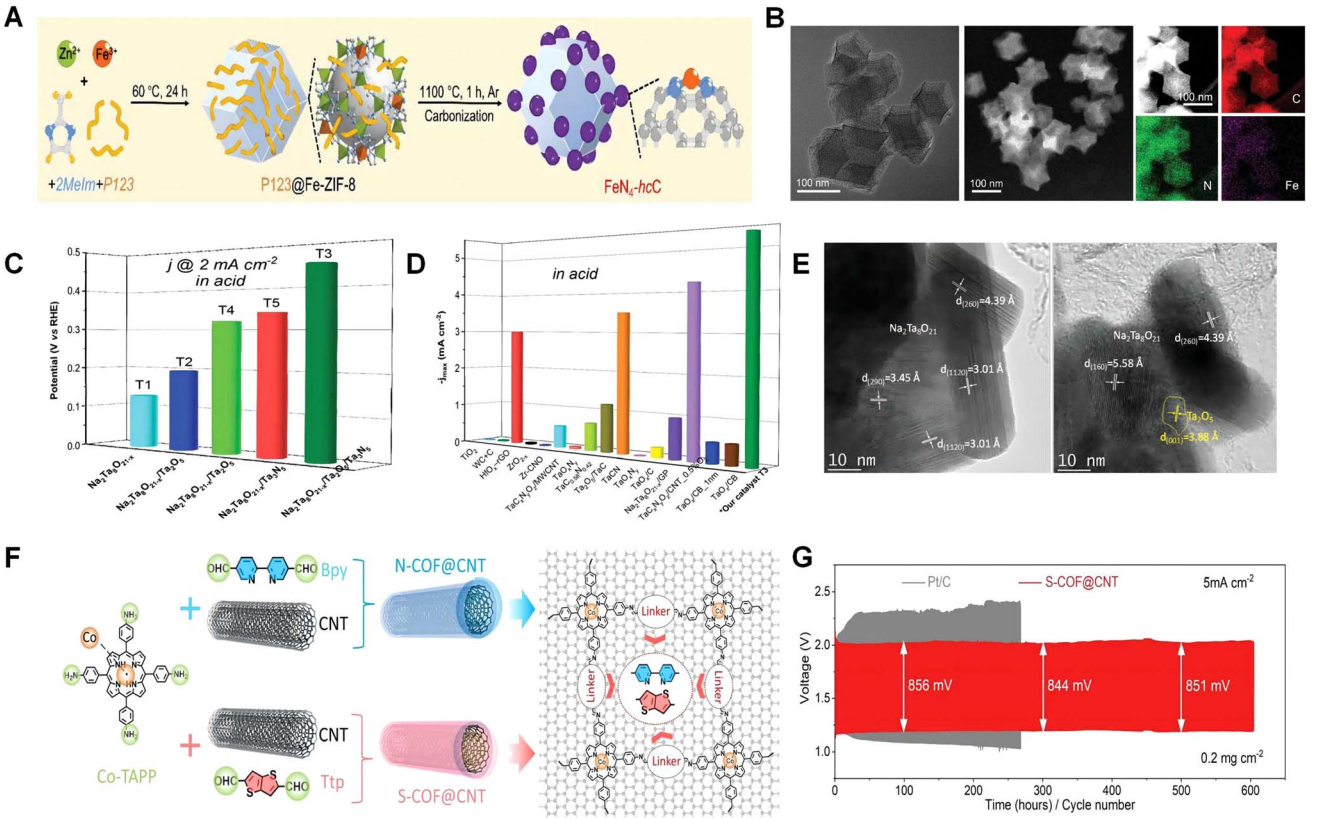

Fig. 13 (A) Schematic illustration of the synthesis of FeN_4-hcC. (B) TEM, HAADF-STEM images, and HAADF-STEM. Reproduced from ref. 234 with permission. Copyright 2023, Wiley-VCH GmbH. (C) Comparisons of the potential at a current density of 2 mA cm^{-2} in acidic medium for samples T1–T5 with different crystal compositions. (D) Comparisons of the maximum current density of T3 with the reported representative catalysts. (E) HRTEM images of the four representative Ta-based catalysts. Reproduced from ref. 235 with permission. Copyright 2020, Wiley-VCH GmbH. (F) Synthetic routes of N–COF@CNT and S–COF@CNT. Galvanostatic cycling curves of the ZABs assembled with S–COF@CNT and Pt/C electrocatalysts. (G) Galvanostatic cycling curves of the ZABs assembled with S–COF@CNT and Pt/C electrocatalysts. Reproduced from ref. 236 with permission. Copyright 2023, Wiley-VCH GmbH.

In Fig. 13A, a highly curved porous carbon material that successfully supports single metal FeN_4 sites is prepared and exhibits excellent oxygen reduction catalytic performance.[234] The research results show that compared to planar carbon materials, highly curved carbon materials can form more FeN_4 active sites and have better ORR activity and stability, refer to Fig. 13B. Furthermore, the study also finds that the curvature of carbon materials has a significant impact on the catalytic activity and stability of FeN_4 sites, with higher curvature resulting in higher catalytic activity of FeN_4 sites. It demonstrates how to design the phase composition and structure of nitrogen-doped graphene-supported Ta-based oxide materials to achieve composite catalysts with excellent ORR activity, stability, and methanol tolerance in acidic and alkaline media, as shown in Fig. 13E.[235] DFT calculations of the work function of Ta-based catalytic phases show that electron transfer between nanocrystals leads to the formation of charge accumulation layers at the interface. This phenomenon promotes the activation of O_2 molecules and enhances the performance of the ORR, refer to Fig. 13C and D for details. This type of mixed catalyst exhibits great flexibility and can be used in fuel cells, such as those combined with proton or anion membranes, and metal–air batteries. A highly efficient electrocatalyst system, COF@CNT, assembled from molecular units for the ORR is proposed.[236] The assembly process combined with the modification of carbon nanotubes induced the formation of COF nanomaterials with highly spin-active cobalt sites. Experimental results demonstrate that the material exhibits excellent ORR performance, refer to Fig. 13F. Specifically, S–COF@CNT displays an impressive onset potential of 0.87 V *vs.* RHE, a Tafel slope of 45.2 mV dec^{-1}, an $E_{1/2}$ of 0.77 V *vs.* RHE, and a J of 5.41 mA cm^{-2}. While some of these metrics are not as good as those of Pt/C (20% wt%), they outperform those of all the comparative samples, molecular units, and other COF electrocatalysts. The exceptional performance is attributed to the optimized electronic configuration and constrained charge behavior of the composite material, which helps regulate the adsorption strength of oxygen intermediates and thereby promotes oxygen electrocatalysis. These results highlight the potential of the reticular chemistry strategy in designing and synthesizing efficient non-platinum-based electrocatalysts, refer to Fig. 13G for details. Moreover, this work provides significant insights into improving electrochemical activity through orbital interactions and charge behavior. This may provide valuable guidance for designing high-performance catalysts in the future.

As studied, the relationship between a carrier and a catalyst is not only a simple loading interaction, but also a means to modify the electronic structure or electron transfer rate of the catalyst by tuning the carrier, thereby enhancing the stability of the catalyst.[237] It may be difficult to adjust the structural curvature of the catalyst, but the morphology of the carrier can be relatively easily modified, such as carbon nanotubes, carbon nanospheres, and carbon nanosheets with different curvatures. Therefore, indirectly adjusting the catalyst by manipulating the carrier is a convenient method and also provides new directions for future research.[238–240]

5.3 Regulatable catalysts

A regulatable ORR catalyst refers to a type of catalyst that can adjust its catalytic activity for the ORR by changing the proportion of different raw materials, synthesis temperature, coordination environment of active centers, and morphology. This allows for the catalytic process of the ORR to be selectively tuned from four-electron to two-electron or from two-electron to four-electron based on specific requirements. This type of regulatable catalyst is of great significance for future industrial production of catalysts.[241] For example, by adjusting the production parameters, different performance ORR catalysts can be obtained using the same production process.[242] This also promotes the study of the ORR process, enhancing our understanding of aspects such as electron transfer in reaction mechanisms.[243]

Some researchers utilize the strategy of heteroatom doping (P and S) to optimize the electronic structure and N doping content/configuration of the N-doped hollow mesoporous carbon sphere (N-HMCS) carbon framework, resulting in the redistribution of charges and enhanced adsorption of O_2 molecules, refer to Fig. 14A.[244] This led to improved ORR activity by activating adjacent carbon sites and effectively increasing/decreasing the binding energy of *OOH. Therefore, the selectivity for the four-electron ORR is greatly enhanced, as shown in Fig. 14B. The efficient ORR selectivity changes with the doping system. Electrochemical tests in 0.1 M KOH showed that compared to N-HMCS samples, N, P-HMCS and N, S-HMCS exhibited higher E_{on} and $E_{1/2}$ values, refer to Fig. 14C. In addition, N, P co-doping and N, S co-doping trigger different ORR pathways. In the voltage range of 0–0.8 V *vs.* RHE, N, P-HMCS tends to favor the two-electron ORR (an average electron transfer number of 2.22), while N, S-HMCS tends to favor the four-electron ORR (an average electron transfer number of 3.72), refer to Fig. 14D for details. Researchers conducted an in-depth systematic study on SACs for the ORR, refer to Fig. 14E.[245] Through a "materials design-*in situ* spectroscopy-theoretical calculation" integrated research approach, they revealed the importance of the molecular structure (first and second coordination domains) of single-atom catalysts in regulating the selectivity of the reaction. Unlike the focus on the metal center in previous studies, this work demonstrates that the coordination environment of single-atom catalysts plays a significant role in regulating the electronic structure of active sites and the adsorption stability of intermediates and even promotes the transformation of the true active adsorption site from the metal center to the surrounding carbon atoms. This enables a significant control of ORR selectivity from ideal four-electron to two-electron, refer to Fig. 14F and G for details. This research also perfectly explains the differences in ORR selectivity reported in numerous literature studies on single-atom catalysts and the catalyst can achieve regulation of electron transfer in catalysts. Other research has discovered that the main group metal Bi can efficiently catalyze the ORR, with metallic Bi selectively reducing O_2 to H_2O_2, while single-atom site Bi/NC reduces O_2 to H_2O.[246] By finely controlling the thermal decomposition of metal–organic frameworks as shown in Fig. 14H, researchers synthesized controllable carbon-supported Bi

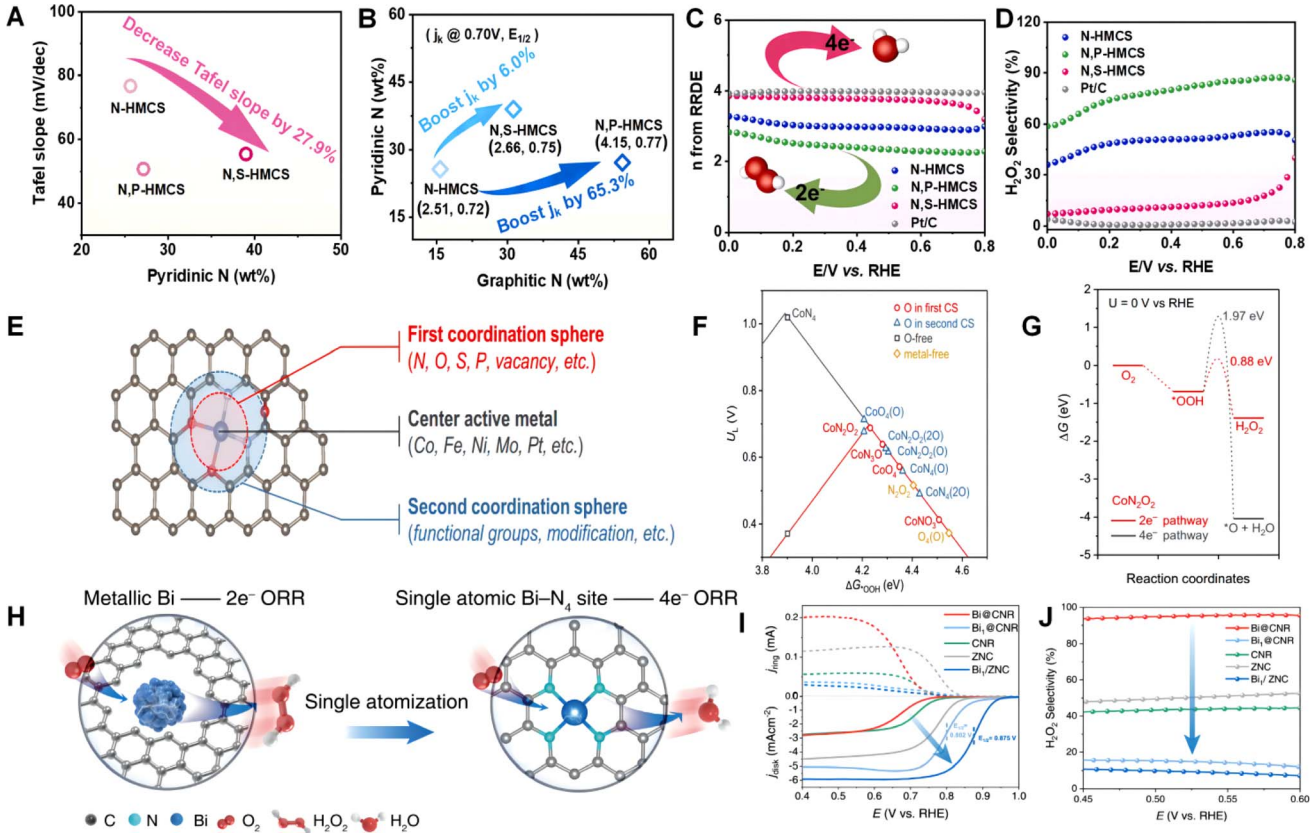

Fig. 14 (A) Relationship between the Tafel slope and pyridinic N proportion, and (B) relationship between ORR activities (j_k @0.70 V *vs.* RHE and $E_{1/2}$) and N (pyridinic N and graphitic N) proportions. (C) Electron-transfer number. (D) H_2O_2 selectivity. Reproduced from ref. 244 with permission. Copyright 2023, Royal Society of Chemistry. (E) Schematic of SACs, highlighting the first and second coordination spheres and center active metal. (F) Computed activity volcano plots of the ORR *via* the two-electron (red color) or four-electron (black) pathway for SACs with varied configurations. (G) Free energy diagram for the two-electron (red) or four-electron (black) ORR pathway on the CoN_2O_2 moiety. Reproduced from ref. 245 with permission. Copyright 2021, American Chemical Society. (H) Schematic illustration of the metallic Bi-catalyzed two-electron ORR and single-atomic site Bi–N_4 catalyzed four-electron ORR. (I) Polarization curves (solid lines) and simultaneous H_2O_2 detection current at the ring electrode (dashed lines) at 1600 rpm in 0.1 M KOH for Bi1@CNR, Bi1/ZNC, and the reference samples. (J) Calculated selectivity of the above catalysts at various potentials. Reproduced from ref. 246 with permission. Copyright 2023, Elsevier.

nanoparticles as catalysts and demonstrated that metal Bi can catalytically reduce O_2 to H_2O_2 efficiently (selectivity > 96% with a kinetic current density of 3.8 mA cm^{-2} at 0.65 V *vs.* RHE) and stably (2% decay over 10 hours of electrolysis). Theoretical calculations showed that the stronger O–O bond and appropriate *OOH adsorption on the p-region surface of metal Bi facilitate the preservation of the O–O bond and efficient generation of H_2O_2. More surprisingly, after atomizing Bi metal, the nitrogen-doped carbon-supported Bi single-atom material reversed the selectivity of the Bi metal ORR, exhibiting lower ΔG_{*O} and small four-electron ORR overpotential, demonstrating excellent four-electron activity (a half-wave potential of 0.875 V *vs.* RHE), refer to Fig. 14J for details.

Regulatable ORR catalysts are a type of catalyst that can control the activity and selectivity of the ORR by adjusting factors such as the material composition, morphology, and coordination environment of active centers. The controllable catalysts not only have practical applications but also contribute significantly to the study of mechanisms. A profound understanding and knowledge of the ORR mechanism are prerequisites for successfully controlling the selectivity of catalysts.[247] This aligns with the earlier discussion on the need to enhance understanding and research on the mechanism. Furthermore, this will provide better guidance for the design of more efficient catalysts for the two-electron or four-electron ORR. Significant progress has been made in this research direction, with great potential for further development in the future.[248,249]

6 Industrial production and device applications

In recent years, research on how to apply discoveries and inventions to the real world, including large-scale testing and evaluation of products and processes, has been increasingly valued. Therefore, more and more researchers are focusing on the application and performance of their catalysts in devices.[250,251] The two processes of the ORR, the two-electron pathway and the four-electron pathway, have different device application scenarios. The two-electron process was not valued in the early years. However, in recent years, hydrogen peroxide as a green oxidant has begun to be widely used in various

scenarios. Therefore, the preparation of hydrogen peroxide on a large scale with high selectivity through the electrocatalytic ORR has received attention from researchers. Unlike the application of the two-electron ORR, the four-electron ORR is mainly used in fuel cells and metal–air batteries.[252] However, the reduction of the overpotential of the reaction, improvement of the reaction rate, and enhancement of the performance and efficiency of fuel cells are the problems that researchers are facing now.[253]

6.1 Industrial preparation of hydrogen peroxide

The primary industrial application of the two-electron process is the synthesis of hydrogen peroxide. H_2O_2 is an important green oxidant widely used in industrial and household settings, including pulp/textile bleaching, wastewater treatment, chemical synthesis, and disinfection.[258] However, traditional methods of H_2O_2 production are energy-intensive, leading to high economic costs and environmental concerns due to the use of toxic organic solvents.[248,259] The electrochemical two-electron ORR stands out as a promising route for clean H_2O_2 production due to its mild aqueous conditions and the ability to be powered by green electricity, aligning with the principles of green chemistry. Furthermore, in recent years, the utilization of *in situ* generated hydrogen peroxide to react with substrates for the degradation or the production of high-value-added chemicals has also been increasingly emphasized. For instance, combining the production of H_2O_2 with AOP for plastic depolymerization has gained attention as a method to achieve plastic degradation.

To achieve the large-scale industrial application of electrochemical hydrogen peroxide synthesis, reactor design is crucial to ensure performance and economic viability. A well-designed reactor can facilitate the reaction, promote H_2O_2 generation, and minimize its decomposition. The mass transport of O_2 to the cathode vicinity is a key factor to consider in reactor design. Commonly used reactors include PEM electrolysis reactors and solid-state electrolyte fuel cells.[23,260]

6.1.1 Proton exchange membrane electrolysis. The PEM electrolysis reactor is designed based on membrane electrode assembly, where the anode and cathode catalysts come into direct contact with the ion exchange membrane. During the reaction, the anode oxidizes to serve as a source of protons, which are transferred through the ion exchange membrane to the cathode to drive the production of H_2O_2.[260] The generated hydrogen peroxide dissolves in the electrolyte solution within the reaction chamber. Typically, the yield of hydrogen peroxide

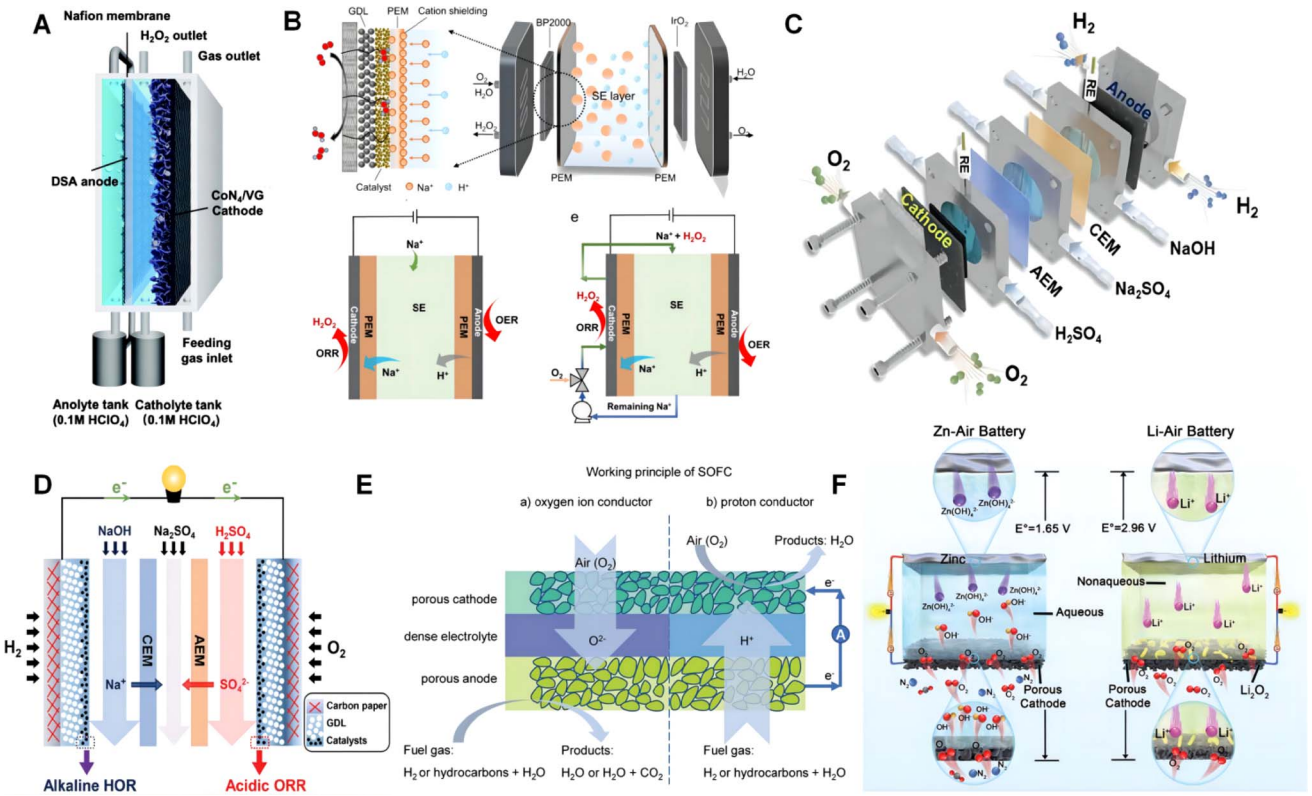

Fig. 15 (A) Schematic of the flow cell setup utilizing CoN_4/VG as the cathode. Reproduced from ref. 254 with permission. Copyright 2022, Royal Society of Chemistry. (B) Schematic illustration of reducing O_2 to H_2O_2 in our SE cell with a double-PEM configuration. Reproduced from ref. 255 with permission. Copyright 2022, Nature Publishing Group. (C) Schematic illustration of the CF-FC system with 2.0 M H_2SO_4 and 4.0 M NaOH as the catholyte and anolyte, respectively. (D) Schematic illustration of the CF-FC consisting of an acidic ORR chamber (0.5 M H_2SO_4). Reproduced from ref. 17 with permission. Copyright 2024, Wiley-VCH GmbH. (E) Working principle of the SOFC with an oxygen-ion conductor electrolyte (SOFC). Reproduced from ref. 256 with permission. Copyright 2022, Wiley-VCH GmbH. (F) Reproduced from ref. 257 with permission. Copyright 2024, Wiley-VCH GmbH.

can be controlled by adjusting reaction conditions such as temperature and current density. However, traditional PEM systems suffer from low transport efficiency and issues affecting charge transfer, prompting researchers to modify conventional PEM electrolysis cells.[261]

In this study, as shown in Fig. 15A, the researchers modified commercially available flow cell reactors and employed them for continuous electrochemical testing.[254] Due to its layered porous structure and self-standing characteristics, the CoN_4/VG composite material facilitated rapid O_2 and charge transfer, and these overcome the stagnation typically observed in conventional gas diffusion electrode (GDE) setups by constructing a hydrophobic gas diffusion layer (GDL) on the back of the VG component. This modification achieved a record high hydrogen peroxide production rate of 4000 mmol $g_{catalyst}^{-1}$ h^{-1} at a constant concentration (approximately 1100 ppm), equivalent to an energy consumption of 3.81 W h g^{-1}, representing the most energy-efficient design for acid-mediated H_2O_2 electrosynthesis.

6.1.2 Solid-state electrolyte fuel cells. Solid-state electrolyte fuel cells consist of a dual-membrane device composed of solid electrolytes, where separate streams of H_2 and oxygen O_2 are transported to the anode and cathode separated by porous solid electrolytes. Through electrochemical processes, H^+ and HO_2^- are generated and transported to the solid electrolyte layer, combining to form a pure H_2O_2 solution. This device introduces H_2 and O_2 in a pure state to accelerate the reaction, while the dual membranes prevent direct contact with liquid water to avoid flooding.[208,209]

In order to design more efficient electrolysis cells, a device is designed and a SE reactor is developed.[255] As shown in Fig. 15B, the SE reactor differs from traditional PEM-MEA fuel cell designs, as it utilizes three chambers separated by two PEMs to fully exploit this cation effect and achieve high-performance H_2O_2 production. Throughout the entire cell voltage range, the H_2O_2 faradaic efficiency remains above 85%, reaching a maximum of 96% at 5 and 20 mA cm^{-2}, significantly higher than that of traditional MEA unit configurations. In contrast, reactors without alkali metal cations require higher transport potentials and exhibit much lower H_2O_2 FE under high current density conditions.

6.2 Applications of four-electron ORR devices

The application of the four-electron ORR in practical scenarios is primarily focused on energy supply, especially in fuel cells and metal–air batteries. In the context of four-electron ORR applications, this mechanism involves the reduction of oxygen molecules to water through a four-electron transfer process, which is highly desirable for efficient energy conversion.[262] This process is crucial for achieving high energy efficiency and power density in electrochemical devices. Therefore, the application of four-electron transfer in the ORR within electrochemical devices contributes to the advancement of energy conversion and storage technologies. By understanding and optimizing the mechanisms involved in this process, researchers and engineers can develop more efficient and sustainable energy solutions for a wide range of industrial and consumer applications.[263]

6.2.1 Fuel cells. Existing fuel cells are mainly divided into proton exchange membrane fuel cells (PEMFCs), phosphoric acid fuel cells (PAFCs), molten carbonate fuel cells (MCFCs), alkaline fuel cells (AFC), and solid oxide fuel cells (SOFCs). However, PAFCs operate at high temperatures around 150–200 °C, making it challenging to manage liquid electrolytes under high-temperature conditions. In MCFCs, corrosion and leakage issues during long-term operation significantly reduce the lifespan of the cells, while AFCs suffer from low cell density, limiting the utility of these types of fuel cells. As a result, current research focuses on PEMFCs and SOFCs.[264]

PEMFCs, essentially a reverse of water electrolysis, consist of an anode, cathode, and proton exchange membrane. The anode serves as the site for hydrogen fuel oxidation, while the cathode serves for oxidant reduction, both containing catalysts for accelerating electrode reactions, with the proton exchange membrane as the electrolyte. During operation, it acts as a direct current source, with the anode as the negative pole and the cathode as the positive pole.[65]

In H_2–O_2 fuel cells, the ORR at the cathode directly controls the overall performance and energy conversion efficiency. While platinum-based catalysts can accelerate the slow ORR, their high cost hinders their widespread application in H_2–O_2 fuel cells. Addressing this issue, as shown in Fig. 15C and D, a novel Coupled Flow Fuel Cell (CF-FC) that integrates acidic ORR and alkaline HOR is proposed.[17] Unlike traditional H_2–O_2 fuel cells using either acidic or alkaline media throughout, the newly developed CF-FC features additional H^+ and OH^- electrochemical neutralization capacities, significantly increasing the theoretical OCV to 2.057 V *vs.* RHE (compared to the traditional H_2–O_2 fuel cell's theoretical OCV of 1.229 V *vs.* RHE).

SOFCs utilize solid oxide oxygen ion (O^{2-}) conductors as electrolytes, facilitating O^{2-} transfer and the separation of air and fuel. Compared to other types of fuel cells, SOFCs exhibit strong fuel adaptability (Fig. 15E). SOFCs can use carbon monoxide, hydrocarbons, and other fuels, and their electrode and electrolyte materials are ceramics, significantly reducing fuel cell costs. Solid structures have the advantages of low manufacturing and maintenance costs, no electrode poisoning, no leakage corrosion, and long service life. And SOFC systems have promising applications in large centralized power supply, medium-scale distributed power, and small household cogeneration, as fixed power stations, and as power sources for ships and vehicles, offering broad prospects in both stationary and mobile power applications.[265]

6.2.2 Metal–air batteries. Metal–air batteries are a type of semi-storage and semi-fuel cell that offer excellent rate performance, high energy density, and low-carbon sustainability. They are considered a new generation of energy storage and conversion devices. Renowned scholar Leclanché developed the world's first metal–air battery in 1868, and since then, various types of metal–air batteries have been developed.[266]

Most metal–air batteries primarily involve oxygen (along with carbon dioxide, nitrogen, *etc.*) in the positive electrode

reactions. The charging and discharging processes are based on the ORR and OER occurring in the positive electrode region. With the continuous growth in energy demand, efficient energy storage systems have become an urgent need for clean and renewable energy sources.[267] However, metal–air batteries still face challenges due to their limited theoretical energy density, which can hinder their development. Through research, it has been found that by altering the cathode material, metal–air batteries may significantly enhance energy density. During discharge, the battery undergoes electrochemical reactions between the metal and O_2 to form discharge products, typically in the form of metal peroxides/superoxides or metal hydroxides (in aqueous solutions). The specific process is illustrated in Fig. 15F. Currently, the widely used metal electrodes in metal–air batteries are lithium, sodium, potassium, magnesium, aluminum, zinc, and iron. Among them, lithium is a relatively common choice, yet it is plagued by serious issues, including safety concerns, gradual decomposition of lithium, and susceptibility to moisture and CO_2.[268] Compared to other metal–air batteries, zinc–air battery technology is relatively mature and exhibits excellent performance.[269] However, zinc–air batteries face challenges such as inherent dendritic growth and morphological changes in the zinc electrode, as well as electrode failure. Other metal–air batteries like magnesium–air, aluminum–air, and iron–air batteries suffer from low coulombic efficiency, high costs, and slow ORR kinetics.[270] In the future, metal–air battery technology will continue to face numerous challenges. Firstly, the energy density of metal–air batteries needs to be enhanced, which can be achieved through designing novel electrode structures and optimizing catalysts and electrolytes to achieve higher energy storage and output. Furthermore, the high material costs of metal–air batteries pose a barrier to meeting practical applications and market competitiveness. Reducing battery costs, enhancing production efficiency, and optimizing manufacturing processes are essential steps to lower the costs and enhance their market viability.[271] Overall, metal–air batteries hold considerable promise as a pivotal technology in the field of energy storage in the future, and this provides reliable and efficient energy solutions for renewable energy applications, electric vehicles, and small electronic devices.[272,273]

7 Summary and outlook

The development of ORR catalysts has made significant progress until today, thanks to the importance of ORR catalysts. For example, the ORR four-electron process is highly significant in zinc–air batteries and fuel cells. Moreover, hydrogen peroxide produced by the two-electron process is an industrially valuable chemical product and raw material. Nowadays, with the advancement of various catalysts such as iron–nitrogen, cobalt–nitrogen, and platinum-based catalysts, the design of ORR catalysts has entered a new stage. However, we are also facing numerous challenges, such as the need for the development of *in situ* characterization techniques and new catalysts, as well as the application of devices and industries, all of which require researchers' efforts.

7.1 Quest for advanced characterization techniques

With the continuous advancement in catalyst design and synthesis technology, there is a growing need to comprehend the performance and reaction mechanisms of ORR catalysts with greater efficiency and precision. To gain insights into these reaction mechanisms, it is imperative to employ advanced characterization techniques for validation. The specific characterization techniques can be classified as follows. By utilizing *in situ*/atomic scale characterization techniques such as *in situ* spectroscopy, atomic force microscopy, *etc.*, researchers can observe the surface structure of the catalyst, as well as the generation and transformation of intermediates during the ORR in real time. These techniques facilitate the observation of dynamic changes in the catalyst and offer detailed insights into the catalytic mechanism, thereby providing more precise guidance for catalyst optimization design. Furthermore, employing high-resolution surface chemical analysis techniques, like X-ray photoelectron spectroscopy and scanning electron microscopy, enables a comprehensive understanding of the surface composition, atomic structure, and chemical state of ORR catalysts. These analytical results play a pivotal role in understanding critical factors such as the active sites of the catalyst and interfacial interactions. Moreover, studying the electronic and proton conductivity performance reveals the efficiency and rate of electron and ion transfer within ORR catalysts. This knowledge is essential for understanding the dynamic response of the catalyst and its polarization behavior and optimizing its electrochemical performance. By integrating various scale characterization techniques such as electrochemical *in situ* spectroscopy and electron microscopy-computational simulation, researchers can comprehensively unveil the structure, morphology, and surface activity of ORR catalysts. This holistic approach aids in gaining a thorough understanding of the catalyst's performance and reaction mechanism. It is anticipated that with the continuous progress in science and technology, more *in situ* characterization techniques will be developed to enable researchers to delve deeper into mechanisms or catalyst design.

7.2 Quest for ORR catalysts

In recent years, the development of ORR catalysts has been thriving, and various catalysts have been developed. However, ORR catalysts still face many difficulties and challenges. Firstly, catalysts still suffer from the problem of trade-offs between selectivity and stability, thus making the development of highly selective and stable catalysts an urgent issue to be addressed. Secondly, the majority of existing catalyst raw materials are expensive, and the synthesis process is cumbersome and does not align with the principles of green chemistry. Therefore, from both economic and environmental perspectives, developing inexpensive and non-polluting catalysts is the next challenge for researchers. Finally, most of the existing catalysts are tested in laboratory environments, which limits the speed of translating laboratory techniques into practical results. Therefore, researchers should strive to simulate real environments as

much as possible when testing catalyst performance in order to develop catalysts that can achieve high efficiency and stability in practical environments.

7.3 Quest for theoretical calculation

The application of theoretical calculations in the field of ORR catalysts holds significant future prospects. Through theoretical calculations, a deep understanding of key properties such as the electronic structure, surface adsorption capabilities, and reaction kinetics of ORR catalysts can be achieved, and these can provide guidance for catalyst design and optimization. However, there are still many challenges in the use of theoretical calculations in the design and catalysis of ORR catalysts. For instance, predicting active sites through energy and electronic structure calculations can identify highly active ORR catalyst active sites, and this can guide the synthesis and development of new catalysts; theoretical calculations can reveal the electron transfer, bond-breaking, and bond-forming steps of ORR catalysts, which helps researchers to further understand the catalytic mechanism and design high-performance catalysts; with the advancement of computer technology and computational methods, the application of theoretical calculations in ORR catalyst research will become more widespread and robust. Additionally, when combined with experimental approaches, theoretical calculations can provide crucial information about material properties, catalytic mechanisms, and design guidance, collectively advancing ORR catalyst research.

7.4 Quest for devices

Whether in-depth research on mechanisms and reaction kinetics or the design and development of various catalysts, the ultimate goal is their application in practical production. The practical application of the ORR can be divided into two parts: industrial production represented by the two-electron ORR and energy device development represented by the four-electron ORR. In recent years, both these aspects have seen rapid development; however, numerous challenges and difficulties persist for future progress. Firstly, for the synthesis of hydrogen peroxide through the two-electron ORR, existing catalysts still suffer from low current density, which does not meet the requirements for industrial production. Moreover, ensuring that hydrogen peroxide does not further decompose during production and increasing yield are also significant challenges. Secondly, there is still a lack of understanding and research on the two-electron ORR process and development. For instance, through the *in situ* generation of hydrogen peroxide in the ORR, utilizing *in situ* generated hydrogen peroxide to react with other substrates can produce high-value-added chemicals. A representative example is that the reaction of hydrogen peroxide with ethylene produces ethylene glycol or epoxyethane. For the application of the four-electron ORR, it is primarily used in the energy sector, such as in fuel cells and metal–air batteries. However, existing devices suffer from low energy efficiency. Therefore, these devices need performance and efficiency enhancements through technological innovation and optimization. The integration of new materials, refinement of reaction mechanisms, and enhancement of catalyst activity can lead to superior performance in ORR devices for energy conversion. Additionally, economic costs pose a significant barrier. As devices mature technologically and costs decrease, their economic feasibility in commercial applications will improve. This, in turn, will incentivize businesses and institutions to increase investments in the research and production of ORR devices, thereby boosting their market penetration. In conclusion, with continuous technological advancements and wider applications, ORR devices hold significant prospects for development in energy conversion and environmental protection.

7.5 Quest for mechanical learning

In recent years, machine learning has captured the sustainable interest of researchers due to its advantages of fast execution speed, flexibility, and user-friendliness. However, this popularity also raises concerns about the potential misuse or misinterpretation of "black-box" results, which can lead to significant discrepancies between predicted outcomes and actual results. To address this issue, it is crucial for researchers to develop more accurate models for prediction. On one hand, researchers must enhance their understanding of the underlying reaction processes. By simplifying the reaction processes and data as much as possible, the models can better comprehend the processes and improve prediction accuracy. On the other hand, researchers can leverage cutting-edge technologies like deep learning to build models. Deep learning, a subfield within machine learning research, constructs artificial neural networks to mimic the human brain. Unlike traditional machine learning, deep learning utilizes extensive neural networks for training, which is particularly vital for developing complex catalysis models for predictions.

Data availability

Data availability is not applicable to this article, as no new data were created or analyzed in this article.

Author contributions

The manuscript was written through contributions of all authors. All authors have given approval to the final version of the manuscript.

Conflicts of interest

The authors declare no conflict of interest.

Acknowledgements

S. Z. is thankful for financial support from the National Natural Science Foundation of China (grant no. 22373027). This work was jointly supported by the Fundamental Research Funds for the Central Universities 2023ZKPYHH05.

References

1 C. Wei, Z. Feng, G. G. Scherer, J. Barber, Y. Shao-Horn and Z. J. Xu, Cations in Octahedral Sites: A Descriptor for Oxygen Electrocatalysis on Transition-Metal Spinels, *Adv. Mater.*, 2017, **29**, 1606800.

2 W. Xia, A. Mahmood, Z. Liang, R. Zou and S. Guo, Earth-Abundant Nanomaterials for Oxygen Reduction, *Angew. Chem., Int. Ed.*, 2016, **55**, 2650–2676.

3 Y. Nie, L. Li and Z. Wei, Recent advancements in Pt and Pt-free catalysts for oxygen reduction reaction, *Chem. Soc. Rev.*, 2015, **44**, 2168–2201.

4 J. Hwang, R. R. Rao, L. Giordano, Y. Katayama, Y. Yu and Y. Shao-Horn, Perovskites in catalysis and electrocatalysis, *Science*, 2017, **358**, 751–756.

5 N. S. Lewis and D. G. Nocera, Powering the Planet: Chemical Challenges in Solar Energy Utilization, *Proc. Natl. Acad. Sci. U. S. A.*, 2006, **103**, 15729–15735.

6 J. H. Montoya, L. C. Seitz, P. Chakthranont, A. Vojvodic, T. F. Jaramillo and J. K. Nørskov, Materials for Solar Fuels and Chemicals, *Nat. Mater.*, 2017, **16**, 70–81.

7 H. Huang, M. Sun, S. Li, S. Zhang, Y. Lee, Z. Li, J. Fang, C. Chen, Y.-X. Zhang, Y. Wu, Y. Che, S. Qian, W. Zhu, C. Tang, Z. Zhuang, L. Zhang and Z. Niu, Enhancing H_2O_2 Electrosynthesis at Industrial-Relevant Current in Acidic Media on Diatomic Cobalt Sites, *J. Am. Chem. Soc.*, 2024, **146**, 9434–9443.

8 J. Liu, H. Xu, J. Zhu and D. Cheng, Understanding the Pathway Switch of the Oxygen Reduction Reaction from Single- to Double-/Triple-Atom Catalysts: A Dual Channel for Electron Acceptance–Backdonation, *JACS Au*, 2023, **3**, 3031–3044.

9 J.-W. Chen, Z. Zhang, H.-M. Yan, G.-J. Xia, H. Cao and Y.-G. Wang, Pseudo-adsorption and Long-range Redox Coupling During Oxygen Reduction Reaction on Single Atom Electrocatalyst, *Nat. Commun.*, 2022, **13**, 1734.

10 X. Zhang, J. Liu, R. Li, X. Jian, X. Gao, Z. Lu and X. Yue, Machine Learning Screening of High-Performance Single-atom Electrocatalysts for Two-electron Oxygen Reduction Reaction, *J. Colloid Interface Sci.*, 2023, **645**, 956–963.

11 I. C. Man, H.-Y. Su, F. Calle-Vallejo, H. A. Hansen, J. I. Martínez, N. G. Inoglu, J. Kitchin, T. F. Jaramillo, J. K. Nørskov and J. Rossmeisl, Universality in Oxygen Evolution Electrocatalysis on Oxide Surfaces, *ChemCatChem*, 2011, **3**, 1159–1165.

12 Z. W. Seh, J. Kibsgaard, C. F. Dickens, I. Chorkendorff, J. K. Nørskov and T. F. Jaramillo, Combining Theory and Experiment in Electrocatalysis: Insights into Materials Design, *Science*, 2017, **355**, eaad4998.

13 L. Shi, X. Lin, F. Liu, Y. Long, R. Cheng, C. Tan, L. Yang, C. Hu, S. Zhao and D. Liu, Geometrically Deformed Iron-Based Single-Atom Catalysts for High-Performance Acidic Proton Exchange Membrane Fuel Cells, *ACS Catal.*, 2022, **12**, 5397–5406.

14 M. Liu, X. Wang, S. Cao, X. Lu, W. Li, N. Li and X.-H. Bu, Ferredoxin-Inspired Design of S-Synergized Fe–Fe Dual-Metal Center Catalysts for Enhanced Electrocatalytic Oxygen Reduction Reaction, *Adv. Mater.*, 2024, 2309231.

15 J. Li, W. Xia, X. Xu, D. Jiang, Z.-X. Cai, J. Tang, Y. Guo, X. Huang, T. Wang, J. He, B. Han and Y. Yamauchi, Selective Etching of Metal–Organic Frameworks for Open Porous Structures: Mass-Efficient Catalysts with Enhanced Oxygen Reduction Reaction for Fuel Cells, *J. Am. Chem. Soc.*, 2023, **145**, 27262–27272.

16 W. Yao, A. Hu, J. Ding, N. Wang, Z. Qin, X. Yang, K. Shen, L. Chen and Y. Li, Hierarchically Ordered Macro–Mesoporous Electrocatalyst with Hydrophilic Surface for Efficient Oxygen Reduction Reaction, *Adv. Mater.*, 2023, **35**, 2301894.

17 L. Shi, D. Liu, X. Lin, R. Cheng, F. Liu, C. Kim, C. Hu, J. Qiu, R. Amal and L. Dai, Stable and High-performance Flow H_2-O_2 Fuel Cells with Coupled Acidic Oxygen Reduction and Alkaline Hydrogen Oxidation Reactions, *Adv. Mater.*, 2024, 2314077.

18 Z. Zhou, Y. Kong, H. Tan, Q. Huang, C. Wang, Z. Pei, H. Wang, Y. Liu, Y. Wang, S. Li, X. Liao, W. Yan and S. Zhao, Cation-Vacancy-Enriched Nickel Phosphide for Efficient Electrosynthesis of Hydrogen Peroxides, *Adv. Mater.*, 2022, **34**, 2106541.

19 S. Ding, B. Xia, M. Li, F. Lou, C. Cheng, T. Gao, Y. Zhang, K. Yang, L. Jiang, Z. Nie, H. Guan, J. Duan and S. Chen, An abnormal Size Effect Enables Ampere-level O_2 Electroreduction to Hydrogen Peroxide in Neutral Electrolytes, *Energy Environ. Sci.*, 2023, **16**, 3363–3372.

20 B.-H. Lee, H. Shin, A. S. Rasouli, H. Choubisa, P. Ou, R. Dorakhan, I. Grigioni, G. Lee, E. Shirzadi, R. K. Miao, J. Wicks, S. Park, H. S. Lee, J. Zhang, Y. Chen, Z. Chen, D. Sinton, T. Hyeon, Y.-E. Sung and E. H. Sargent, Supramolecular Tuning of Supported Metal Phthalocyanine Catalysts for Hydrogen Peroxide Electrosynthesis, *Nat. Catal.*, 2023, **6**, 234–243.

21 J. Du, G. Han, W. Zhang, L. Li, Y. Yan, Y. Shi, X. Zhang, L. Geng, Z. Wang, Y. Xiong, G. Yin and C. Du, CoIn Dual-atom Catalyst for Hydrogen Peroxide Production via Oxygen Reduction Reaction in acid, *Nat. Commun.*, 2023, **14**, 4766.

22 S. Chen, T. Luo, X. Li, K. Chen, J. Fu, K. Liu, C. Cai, Q. Wang, H. Li, Y. Chen, C. Ma, L. Zhu, Y.-R. Lu, T.-S. Chan, M. Zhu, E. Cortés and M. Liu, Identification of the Highly Active Co–N_4 Coordination Motif for Selective Oxygen Reduction to Hydrogen Peroxide, *J. Am. Chem. Soc.*, 2022, **144**, 14505–14516.

23 C. Xia, Y. Xia, P. Zhu, L. Fan and H. Wang, Direct Electrosynthesis of Pure Aqueous H_2O_2 Solutions Up to 20% by Weight Using a Solid Electrolyte, *Science*, 2019, **366**, 226–231.

24 M. Liu, X. Wang, S. Cao, X. Lu, W. Li, N. Li and X.-H. Bu, Ferredoxin-Inspired Design of S-Synergized Fe–Fe Dual-Metal Center Catalysts for Enhanced Electrocatalytic Oxygen Reduction Reaction, *Adv. Mater.*, 2024, **36**, 2309231.

25 X. Zhao and Y. Liu, Origin of Selective Production of Hydrogen Peroxide by Electrochemical Oxygen Reduction, *J. Am. Chem. Soc.*, 2021, **143**, 9423–9428.

26 Z. Jiang, W. Sun, H. Shang, W. Chen, T. Sun, H. Li, J. Dong, J. Zhou, Z. Li, Y. Wang, R. Cao, R. Sarangi, Z. Yang, D. Wang, J. Zhang and Y. Li, Atomic Interface Effect of a Single Atom Copper Catalyst for Enhanced Oxygen Reduction Reactions, *Energy Environ. Sci.*, 2019, **12**, 3508–3514.

27 Z. Wang, X. Jin, C. Zhu, Y. Liu, H. Tan, R. Ku, Y. Zhang, L. Zhou, Z. Liu, S.-J. Hwang and H. J. Fan, Atomically Dispersed Co_2–N_6 and Fe–N_4 Costructures Boost Oxygen Reduction Reaction in Both Alkaline and Acidic Media, *Adv. Mater.*, 2021, **33**, 2104718.

28 T. Wang, Y. Zhang, B. Huang, B. Cai, R. R. Rao, L. Giordano, S.-G. Sun and Y. Shao-Horn, Enhancing Oxygen Reduction Electrocatalysis by Tuning Interfacial Hydrogen Bonds, *Nat. Catal.*, 2021, **4**, 753–762.

29 S. Yang, A. Verdaguer-Casadevall, L. Arnarson, L. Silvioli, V. Čolić, R. Frydendal, J. Rossmeisl, I. Chorkendorff and I. E. L. Stephens, Toward the Decentralized Electrochemical Production of H_2O_2: A Focus on the Catalysis, *ACS Catal.*, 2018, **8**, 4064–4081.

30 R. Ding, Y. Chen, P. Chen, R. Wang, J. Wang, Y. Ding, W. Yin, Y. Liu, J. Li and J. Liu, Machine Learning-Guided Discovery of Underlying Decisive Factors and New Mechanisms for the Design of Nonprecious Metal Electrocatalysts, *ACS Catal.*, 2021, **11**, 9798–9808.

31 Z. Fang, S. Li, Y. Zhang, Y. Wang, K. Meng, C. Huang and S. Sun, The DFT and Machine Learning Method Accelerated the Discovery of DMSCs with High ORR and OER Catalytic Activities, *J. Phys. Chem. Lett.*, 2024, **15**, 281–289.

32 Y. Jiao, Y. Zheng, M. Jaroniec and S. Z. Qiao, Design of Electrocatalysts for Oxygen- and Hydrogen-involving Energy Conversion Reactions, *Chem. Soc. Rev.*, 2015, **44**, 2060–2086.

33 H. Li, S. Kelly, D. Guevarra, Z. Wang, Y. Wang, J. A. Haber, M. Anand, G. T. K. K. Gunasooriya, C. S. Abraham, S. Vijay, J. M. Gregoire and J. K. Nørskov, Analysis of the Limitations in the Oxygen Reduction Activity of Transition Metal Oxide Surfaces, *Nat. Catal.*, 2021, **4**, 463–468.

34 B. Liu, F. Liu, D. Lu, S. Zhang, C. Zhang, Z. Gao, L. Shi, Y. Liu, J. X. Shi, L. Zhang, S. Zhao and D. Liu, Metal-organic Framework Assembly Derived Hierarchically Ordered Porous Carbon for Oxygen Reduction in Both Alkaline and Acidic Media, *Chem. Eng. J.*, 2022, **430**, 132762.

35 G. Liu, A. J. Shih, H. Deng, K. Ojha, X. Chen, M. Luo, I. T. McCrum, M. T. M. Koper, J. Greeley and Z. Zeng, Site-specific Reactivity of Stepped Pt Surfaces Driven by Stress Release, *Nature*, 2024, **626**, 1005–1010.

36 C.-X. Zhao, J.-N. Liu, J. Wang, D. Ren, B.-Q. Li and Q. Zhang, Recent Advances of Noble-metal-free Bifunctional Oxygen Reduction and Evolution Electrocatalysts, *Chem. Soc. Rev.*, 2021, **50**, 7745–7778.

37 P. Cui, L. Zhao, Y. Long, L. Dai and C. Hu, Carbon-Based Electrocatalysts for Acidic Oxygen Reduction Reaction, *Angew. Chem., Int. Ed.*, 2023, **62**, e202218269.

38 S. Liu, Y. Zhang, B. Ge, F. Zheng, N. Zhang, M. Zuo, Y. Yang and Q. Chen, Constructing Graphitic-Nitrogen-Bonded Pentagons in Interlayer-Expanded Graphene Matrix toward Carbon-Based Electrocatalysts for Acidic Oxygen Reduction Reaction, *Adv. Mater.*, 2021, **33**, 2103133.

39 Y. Xia, X. Zhao, C. Xia, Z.-Y. Wu, P. Zhu, J. Y. Kim, X. Bai, G. Gao, Y. Hu, J. Zhong, Y. Liu and H. Wang, Highly Active and Selective Oxygen Reduction to H_2O_2 on Boron-doped Carbon for High Production Rates, *Nat. Commun.*, 2021, **12**, 4225.

40 Y. Zhao, D. P. Adiyeri Saseendran, C. Huang, C. A. Triana, W. R. Marks, H. Chen, H. Zhao and G. R. Patzke, Oxygen Evolution/Reduction Reaction Catalysts: From In Situ Monitoring and Reaction Mechanisms to Rational Design, *Chem. Rev.*, 2023, **123**, 6257–6358.

41 S. C. Perry, D. Pangotra, L. Vieira, L.-I. Csepei, V. Sieber, L. Wang, C. Ponce de León and F. C. Walsh, Electrochemical Synthesis of Hydrogen Peroxide from Water and Oxygen, *Nat. Rev. Chem*, 2019, **3**, 442–458.

42 J. K. Nørskov, J. Rossmeisl, A. Logadottir, L. Lindqvist, J. R. Kitchin, T. Bligaard and H. Jónsson, Origin of the Overpotential for Oxygen Reduction at a Fuel-Cell Cathode, *J. Phys. Chem. B*, 2004, **108**, 17886–17892.

43 A. Kulkarni, S. Siahrostami, A. Patel and J. K. Nørskov, Understanding Catalytic Activity Trends in the Oxygen Reduction Reaction, *Chem. Rev.*, 2018, **118**, 2302–2312.

44 P. M. Attia, A. Grover, N. Jin, K. A. Severson, T. M. Markov, Y.-H. Liao, M. H. Chen, B. Cheong, N. Perkins, Z. Yang, P. K. Herring, M. Aykol, S. J. Harris, R. D. Braatz, S. Ermon and W. C. Chueh, Closed-loop Optimization of Fast-charging Protocols for Batteries with Machine Learning, *Nature*, 2020, **578**, 397–402.

45 R. Ding, R. Wang, Y. Ding, W. Yin, Y. Liu, J. Li and J. Liu, Designing AI-Aided Analysis and Prediction Models for Nonprecious Metal Electrocatalyst-Based Proton-Exchange Membrane Fuel Cells, *Angew. Chem., Int. Ed.*, 2020, **59**, 19175–19183.

46 M. Suvarna and J. Pérez-Ramírez, Embracing Data Science in Catalysis Research, *Nat. Catal.*, 2024, **7**, 624–635.

47 H. Xu, D. Cheng, D. Cao and X. C. Zeng, Revisiting the Universal Principle for the Rational Design of Single-atom Electrocatalysts, *Nat. Catal.*, 2024, **7**, 207–218.

48 S. Palkovits, A Primer about Machine Learning in Catalysis – A Tutorial with Code, *ChemCatChem*, 2020, **12**, 3995–4008.

49 H. Ma, Y. Jiao, W. Guo, X. Liu, Y. Li and X. Wen, Machine Learning Predicts Atomistic Structures of Multielement Solid Surfaces for Heterogeneous Catalysts in Variable Environments, *The Innovation*, 2024, **5**, 100571.

50 C. M. Clausen, O. A. Krysiak, L. Banko, J. K. Pedersen, W. Schuhmann, A. Ludwig and J. Rossmeisl, A Flexible Theory for Catalysis: Learning Alkaline Oxygen Reduction on Complex Solid Solutions within the Ag–Pd–Pt–Ru Composition Space, *Angew. Chem., Int. Ed.*, 2023, **62**, e202307187.

51 N. I. Rinehart, R. K. Saunthwal, J. Wellauer, A. F. Zahrt, L. Schlemper, A. S. Shved, R. Bigler, S. Fantasia and S. E. Denmark, A Machine-learning Tool to Predict Substrate-adaptive Conditions for Pd-catalyzed C–N Couplings, *Science*, 2023, **381**, 965–972.

52 X. Ge, A. Sumboja, D. Wuu, T. An, B. Li, F. W. T. Goh, T. S. A. Hor, Y. Zong and Z. Liu, Oxygen Reduction in Alkaline Media: From Mechanisms to Recent Advances of Catalysts, *ACS Catal.*, 2015, **5**, 4643–4667.
53 M. Zeng, S. Yuan, D. Huang and Z. Cheng, Accelerated Design of Catalytic Water-Cleaning Nanomotors via Machine Learning, *ACS Appl. Mater. Interfaces*, 2019, **11**, 40099–40106.
54 M. Dan, X. Zhang, Y. Yang, J. Yang, F. Wu, S. Zhao and Z.-Q. Liu, Dual-axial Engineering on Atomically Dispersed Catalysts for Ultrastable Oxygen Reduction in Acidic and Alkaline Solutions, *Proc. Natl. Acad. Sci. U. S. A.*, 2024, **121**, e2318174121.
55 S. Zhou, L. Shi, Y. Li, T. Yang and S. Zhao, Metal-Organic Framework-Based Electrocatalysts for Acidic Water Splitting, *Adv. Funct. Mater.*, 2024, 2400767.
56 Z. Wu, X. Liu, H. Li, Z. Sun, M. Cao, Z. Li, C. Fang, J. Zhou, C. Cao, J. Dong, S. Zhao and Z. Chen, A Semiconductor-electrocatalyst Nano Interface Constructed for Successive Photoelectrochemical Water Oxidation, *Nat. Commun.*, 2023, **14**, 2574.
57 M. Wu, G. Zhang, W. Wang, H. Yang, D. Rawach, M. Chen and S. Sun, Electronic Metal–Support Interaction Modulation of Single-Atom Electrocatalysts for Rechargeable Zinc–Air Batteries, *Small Methods*, 2022, **6**, 2100947.
58 K. J. J. Mayrhofer, D. Strmcnik, B. B. Blizanac, V. Stamenkovic, M. Arenz and N. M. Markovic, Measurement of Oxygen Reduction Activities via the Rotating Disc Electrode Method: From Pt Model Surfaces to Carbon-supported High Surface Area Catalysts, *Electrochim. Acta*, 2008, **53**, 3181–3188.
59 Y. Li, B. Jia, Y. Fan, K. Zhu, G. Li and C.-Y. Su, Bimetallic Zeolitic Imidazolite Framework Derived Carbon Nanotubes Embedded with Co Nanoparticles for Efficient Bifunctional Oxygen Electrocatalyst, *Adv. Energy Mater.*, 2018, **8**, 1702048.
60 T. Y. Ma, S. Dai, M. Jaroniec and S. Z. Qiao, Metal–Organic Framework Derived Hybrid Co3O4-Carbon Porous Nanowire Arrays as Reversible Oxygen Evolution Electrodes, *J. Am. Chem. Soc.*, 2014, **136**, 13925–13931.
61 J. Scholz, M. Risch, K. A. Stoerzinger, G. Wartner, Y. Shao-Horn and C. Jooss, Rotating Ring–Disk Electrode Study of Oxygen Evolution at a Perovskite Surface: Correlating Activity to Manganese Concentration, *J. Phys. Chem. C*, 2016, **120**, 27746–27756.
62 F. Dalton, ECS Classics: Historical Origins of the Rotating Ring-Disk Electrode, *Electrochem. Soc. Interface*, 2016, **25**, 50.
63 D. M. R. de Rooij, Electrochemical Methods: Fundamentals and Applications, *Anti-Corros. Methods Mater.*, 2003, **50**, 5.
64 L. Zhang, H. Li and J. Zhang, Kinetics of Oxygen Reduction Reaction on Three Different Pt Surfaces of Pt/C Catalyst Analyzed by Rotating Ring-disk Electrode in Acidic Solution, *J. Power Sources*, 2014, **255**, 242–250.
65 C. Wei, R. R. Rao, J. Peng, B. Huang, I. E. L. Stephens, M. Risch, Z. J. Xu and Y. Shao-Horn, Recommended Practices and Benchmark Activity for Hydrogen and Oxygen Electrocatalysis in Water Splitting and Fuel Cells, *Adv. Mater.*, 2019, **31**, 1806296.
66 Y. Garsany, O. A. Baturina, K. E. Swider-Lyons and S. S. Kocha, Experimental Methods for Quantifying the Activity of Platinum Electrocatalysts for the Oxygen Reduction Reaction, *Anal. Chem.*, 2010, **82**, 6321–6328.
67 S. Treimer, A. Tang and D. C. Johnson, A Consideration of the Application of Koutecký-Levich Plots in the Diagnoses of Charge-Transfer Mechanisms at Rotated Disk Electrodes, *Electroanalysis*, 2002, **14**, 165–171.
68 W. Sheng, M. Myint, J. G. Chen and Y. Yan, Correlating the Hydrogen Evolution Reaction Activity in Alkaline Electrolytes with the Hydrogen Binding Energy on Monometallic Surfaces, *Energy Environ. Sci.*, 2013, **6**, 1509–1512.
69 S. Jung, C. C. L. McCrory, I. M. Ferrer, J. C. Peters and T. F. Jaramillo, Benchmarking Nanoparticulate Metal Oxide Electrocatalysts for the Alkaline Water Oxidation Reaction, *J. Mater. Chem. A*, 2016, **4**, 3068–3076.
70 C. Wei, S. Sun, D. Mandler, X. Wang, S. Z. Qiao and Z. J. Xu, Approaches for Measuring the Surface Areas of Metal Oxide Electrocatalysts for Determining Their Intrinsic Electrocatalytic Activity, *Chem. Soc. Rev.*, 2019, **48**, 2518–2534.
71 C. Wei and Z. J. Xu, The Comprehensive Understanding of as an Evaluation Parameter for Electrochemical Water Splitting, *Small Methods*, 2018, **2**, 1800168.
72 K.-H. Wu, J. Zhang, M. Amdad Ali and S. Zhao, Rotating Ring-disc Electrode Method: Assessing Transient Chemical Interaction of Redox Intermediate with Electrode Surface, *J. Electroanal. Chem.*, 2023, **939**, 117317.
73 D. Voiry, M. Chhowalla, Y. Gogotsi, N. A. Kotov, Y. Li, R. M. Penner, R. E. Schaak and P. S. Weiss, Best Practices for Reporting Electrocatalytic Performance of Nanomaterials, *ACS Nano*, 2018, **12**, 9635–9638.
74 C. C. L. McCrory, S. Jung, I. M. Ferrer, S. M. Chatman, J. C. Peters and T. F. Jaramillo, Benchmarking Hydrogen Evolving Reaction and Oxygen Evolving Reaction Electrocatalysts for Solar Water Splitting Devices, *J. Am. Chem. Soc.*, 2015, **137**, 4347–4357.
75 C. C. L. McCrory, S. Jung, J. C. Peters and T. F. Jaramillo, Benchmarking Heterogeneous Electrocatalysts for the Oxygen Evolution Reaction, *J. Am. Chem. Soc.*, 2013, **135**, 16977–16987.
76 S. Anantharaj, S. R. Ede, K. Karthick, S. Sam Sankar, K. Sangeetha, P. E. Karthik and S. Kundu, Precision and Correctness in the Evaluation of Electrocatalytic Water Splitting: Revisiting Activity Parameters with a Critical Assessment, *Energy Environ. Sci.*, 2018, **11**, 744–771.
77 J. N. Hausmann, S. Mebs, H. Dau, M. Driess and P. W. Menezes, Oxygen Evolution Activity of Amorphous Cobalt Oxyhydroxides: Interconnecting Precatalyst Reconstruction, Long-Range Order, Buffer-Binding, Morphology, Mass Transport, and Operation Temperature, *Adv. Mater.*, 2022, **34**, 2207494.

78 I. Mondal, J. N. Hausmann, G. Vijaykumar, S. Mebs, H. Dau, M. Driess and P. W. Menezes, Nanostructured Intermetallic Nickel Silicide (Pre)Catalyst for Anodic Oxygen Evolution Reaction and Selective Dehydrogenation of Primary Amines, *Adv. Energy Mater.*, 2022, **12**, 2200269.

79 L. Yu, S. Sun, H. Li and Z. J. Xu, Effects of Catalyst Mass Loading on Electrocatalytic Activity: An Example of Oxygen Evolution Reaction, *Fundam. Res.*, 2021, **1**, 448–452.

80 M. B. Stevens, C. D. M. Trang, L. J. Enman, J. Deng and S. W. Boettcher, Reactive Fe-Sites in Ni/Fe (Oxy)Hydroxide Are Responsible for Exceptional Oxygen Electrocatalysis Activity, *J. Am. Chem. Soc.*, 2017, **139**, 11361–11364.

81 W. Chen, B. Wu, Y. Wang, W. Zhou, Y. Li, T. Liu, C. Xie, L. Xu, S. Du, M. Song, D. Wang, Y. liu, Y. Li, J. Liu, Y. Zou, R. Chen, C. Chen, J. Zheng, Y. Li, J. Chen and S. Wang, Deciphering the Alternating Synergy Between Interlayer Pt Single-atom and NiFe Layered Double Hydroxide for Overall Water Splitting, *Energy Environ. Sci.*, 2021, **14**, 6428–6440.

82 S. Anantharaj, P. E. Karthik and S. Noda, The Significance of Properly Reporting Turnover Frequency in Electrocatalysis Research, *Angew. Chem., Int. Ed.*, 2021, **60**, 23051–23067.

83 S. Anantharaj and S. Kundu, Do the Evaluation Parameters Reflect Intrinsic Activity of Electrocatalysts in Electrochemical Water Splitting?, *ACS Energy Lett.*, 2019, **4**, 1260–1264.

84 H. Jiang, Q. He, X. Li, X. Su, Y. Zhang, S. Chen, S. Zhang, G. Zhang, J. Jiang, Y. Luo, P. M. Ajayan and L. Song, Tracking Structural Self-Reconstruction and Identifying True Active Sites toward Cobalt Oxychloride Precatalyst of Oxygen Evolution Reaction, *Adv. Mater.*, 2019, **31**, 1805127.

85 M. Li, Z. Zhao, T. Cheng, A. Fortunelli, C.-Y. Chen, R. Yu, Q. Zhang, L. Gu, B. V. Merinov, Z. Lin, E. Zhu, T. Yu, Q. Jia, J. Guo, L. Zhang, W. A. Goddard, Y. Huang and X. Duan, Ultrafine Jagged Platinum Nanowires Enable Ultrahigh Mass Activity for the Oxygen Reduction Reaction, *Science*, 2016, **354**, 1414–1419.

86 Q. Huang, B. Xia, M. Li, H. Guan, M. Antonietti and S. Chen, Single-zinc Vacancy Unlocks High-Rate H_2O_2 Electrosynthesis From Mixed Dioxygen Beyond Le Chatelier principle, *Nat. Commun.*, 2024, **15**, 4157.

87 S. Zaman and S. Chen, A Perspective on Inaccurate Measurements in Oxygen Reduction and Carbon Dioxide Reduction Reactions, *J. Catal.*, 2023, **421**, 221–227.

88 Y. Hu, Y. Fan, L. Li, J. Zhou, Z. Hu, J.-Q. Wang, J. Dong, S. Zhao and L. Zhang, Modulating 3d Charge State via Halogen Ions in Neighboring Molecules of Metal–Organic Frameworks for Improving Water Oxidation, *Small*, 2024, 2400042.

89 T. Yang, Z. Chen, Y. Yang and S. Zhao, Anion-exchange Membrane Fuel Cells with Ionomerless Cathodes, *Joule*, 2024, **8**, 287–290.

90 Y.-J. Wu, J.-Z. Zheng, X. Zhou, T.-X. Tu, Y. Liu, P.-F. Zhang, L. Tan and S. Zhao, Cationic Defect-Enriched Hydroxides as Anodic Catalysts for Efficient Seawater Electrolysis, *Inorg. Chem. Front.*, 2023, **10**, 2444–2456.

91 Z. Pei, H. Tan, J. Gu, L. Lu, X. Zeng, T. Zhang, C. Wang, L. Ding, P. J. Cullen, Z. Chen and S. Zhao, A Polymeric Hydrogel Electrocatalyst for Direct Water Oxidation, *Nat. Commun.*, 2023, **14**, 818.

92 W.-K. Han, J.-X. Wei, K. Xiao, T. Ouyang, X. Peng, S. Zhao and Z.-Q. Liu, Activating Lattice Oxygen in Layered Lithium Oxides through Cation Vacancies for Enhanced Urea Electrolysis, *Angew. Chem., Int. Ed.*, 2022, **61**, e202206050.

93 P. Zhang, H.-C. Chen, H. Zhu, K. Chen, T. Li, Y. Zhao, J. Li, R. Hu, S. Huang, W. Zhu, Y. Liu and Y. Pan, Inter-site Structural Heterogeneity Induction of Single Atom Fe Catalysts for Robust Oxygen Reduction, *Nat. Commun.*, 2024, **15**, 2062.

94 M. Kato, Y. Iguchi, T. Li, Y. Kato, Y. Zhuang, K. Higashi, T. Uruga, T. Saida, K. Miyabayashi and I. Yagi, Structural Transformation of Pt–Ni Nanowires as Oxygen Reduction Electrocatalysts to Branched Nanostructures during Potential Cycles, *ACS Catal.*, 2022, **12**, 259–264.

95 J. Yang, W. Liu, M. Xu, X. Liu, H. Qi, L. Zhang, X. Yang, S. Niu, D. Zhou, Y. Liu, Y. Su, J.-F. Li, Z.-Q. Tian, W. Zhou, A. Wang and T. Zhang, Dynamic Behavior of Single-Atom Catalysts in Electrocatalysis: Identification of Cu-N3 as an Active Site for the Oxygen Reduction Reaction, *J. Am. Chem. Soc.*, 2021, **143**, 14530–14539.

96 M. Tong, F. Sun, G. Xing, C. Tian, L. Wang and H. Fu, Potential Dominates Structural Recombination of Single Atom Mn Sites for Promoting Oxygen Reduction Reaction, *Angew. Chem., Int. Ed.*, 2023, **62**, e202314933.

97 J. Wei, D. Xia, Y. Wei, X. Zhu, J. Li and L. Gan, Probing the Oxygen Reduction Reaction Intermediates and Dynamic Active Site Structures of Molecular and Pyrolyzed Fe–N–C Electrocatalysts by In Situ Raman Spectroscopy, *ACS Catal.*, 2022, **12**, 7811–7820.

98 Y. Lee, J. Theerthagiri, A. Min, C. J. Moon and M. Y. Choi, Dual-laser Pulse-patterned α-$Co(OH)_2$/rGO Heterointerface for Accelerated Water Oxidation and Surface Phase-transition via In situ Raman spectroscopy, *EcoMat*, 2023, **5**, e12417.

99 W. Zhao, G. Xu, W. Dong, Y. Zhang, Z. Zhao, L. Qiu and J. Dong, Progress and Perspective for In Situ Studies of Oxygen Reduction Reaction in Proton Exchange Membrane Fuel Cells, *Advanced Science*, 2023, **10**, 2300550.

100 M. Liu, J. Zhang, H. Su, Y. Jiang, W. Zhou, C. Yang, S. Bo, J. Pan and Q. Liu, In Situ Modulating Coordination Fields of Single-atom Cobalt Catalyst for Enhanced Oxygen Reduction Reaction, *Nat. Commun.*, 2024, **15**, 1675.

101 J. Qin, H. Liu, P. Zou, R. Zhang, C. Wang and H. L. Xin, Altering Ligand Fields in Single-Atom Sites through Second-Shell Anion Modulation Boosts the Oxygen Reduction Reaction, *J. Am. Chem. Soc.*, 2022, **144**, 2197–2207.

102 M. Lunardon, T. Kosmala, C. Durante, S. Agnoli and G. Granozzi, Atom-by-atom Identification of Catalytic Active Sites in Operando Conditions by Quantitative Noise Detection, *Joule*, 2022, **6**, 617–635.

103 Y. Li, W. Xu, Y.-L. Zou, J. Li, T. Gao, R. Huang, L. Chen, Z. Xiao, J. Shi, Y. Yang and W. Hong, Redox-Mediated Single-Molecule Transistor with A Subthreshold Swing Down To 120 mV Decade−1, *Adv. Funct. Mater.*, 2023, **33**, 2302985.

104 Y.-Q. Wang, X.-H. Dan, X. Wang, Z.-Y. Yi, J. Fu, Y.-C. Feng, J.-S. Hu, D. Wang and L.-J. Wan, Probing the Synergistic Effects of Mg^{2+} on CO_2 Reduction Reaction on CoPc by In Situ Electrochemical Scanning Tunneling Microscopy, *J. Am. Chem. Soc.*, 2022, **144**, 20126–20133.

105 J. Tersoff and D. R. Hamann, Theory and Application for the Scanning Tunneling Microscope, *Phys. Rev. Lett.*, 1983, **50**, 1998–2001.

106 G. Binnig and H. Rohrer, Scanning tunneling microscopy, *Surf. Sci.*, 1983, **126**, 236–244.

107 G. Binnig, H. Rohrer, C. Gerber and E. Weibel, Surface Studies by Scanning Tunneling Microscopy, *Phys. Rev. Lett.*, 1982, **49**, 57–61.

108 Y.-G. Kim, A. Javier, J. H. Baricuatro, D. Torelli, K. D. Cummins, C. F. Tsang, J. C. Hemminger and M. P. Soriaga, Surface Reconstruction of Pure-Cu Single-crystal Electrodes under CO-Reduction Potentials in Alkaline Solutions: A Study by Seriatim ECSTM-DEMS, *J. Electroanal. Chem.*, 2016, **780**, 290–295.

109 T. Kosmala, A. Baby, M. Lunardon, D. Perilli, H. Liu, C. Durante, C. Di Valentin, S. Agnoli and G. Granozzi, Operando Visualization of the Hydrogen Evolution Reaction with Atomic-scale Precision at Different Metal–graphene Interfaces, *Nat. Catal.*, 2021, **4**, 850–859.

110 X. Wang, Z.-F. Cai, D. Wang and L.-J. Wan, Molecular Evidence for the Catalytic Process of Cobalt Porphyrin Catalyzed Oxygen Evolution Reaction in Alkaline Solution, *J. Am. Chem. Soc.*, 2019, **141**, 7665–7669.

111 H. Feng, X. Xu, Y. Du and S. X. Dou, Application of Scanning Tunneling Microscopy in Electrocatalysis and Electrochemistry, *Electrochem. Energy Rev.*, 2021, **4**, 249–268.

112 J. H. K. Pfisterer, Y. Liang, O. Schneider and A. S. Bandarenka, Direct Instrumental Identification of Catalytically Active Surface Sites, *Nature*, 2017, **549**, 74–77.

113 S. E. Balaghi, S. Mehrabani, Y. Mousazade, R. Bagheri, A. S. Sologubenko, Z. Song, G. R. Patzke and M. M. Najafpour, Mechanistic Understanding of Water Oxidation in the Presence of a Copper Complex by In Situ Electrochemical Liquid Transmission Electron Microscopy, *ACS Appl. Mater. Interfaces*, 2021, **13**, 19927–19937.

114 S. Hwang, X. Chen, G. Zhou and D. Su, In Situ Transmission Electron Microscopy on Energy-Related Catalysis, *Adv. Energy Mater.*, 2020, **10**, 1902105.

115 B. He, Y. Zhang, X. Liu and L. Chen, In situ Transmission Electron Microscope Techniques for Heterogeneous Catalysis, *ChemCatChem*, 2020, **12**, 1853–1872.

116 S. Hwang, X. Chen, G. Zhou and D. Su, In Situ Transmission Electron Microscopy on Energy-Related Catalysis, *Adv. Energy Mater.*, 2020, **10**, 1902105.

117 V. Beermann, M. E. Holtz, E. Padgett, J. F. de Araujo, D. A. Muller and P. Strasser, Real-time Imaging of Activation and Degradation of Carbon Supported Octahedral Pt–Ni Alloy Fuel Cell Catalysts at the Nanoscale Using In Situ Electrochemical Liquid Cell STEM, *Energy Environ. Sci.*, 2019, **12**, 2476–2485.

118 W. Wang, H. Yan, U. Anand and U. Mirsaidov, Visualizing the Conversion of Metal–Organic Framework Nanoparticles into Hollow Layered Double Hydroxide Nanocages, *J. Am. Chem. Soc.*, 2021, **143**, 1854–1862.

119 G. Zhao, Y. Yao, W. Lu, G. Liu, X. Guo, A. Tricoli and Y. Zhu, Direct Observation of Oxygen Evolution and Surface Restructuring on Mn_2O_3 Nanocatalysts Using In Situ and Ex Situ Transmission Electron Microscopy, *Nano Lett.*, 2021, **21**, 7012–7020.

120 G.-Z. Zhu, S. Prabhudev, J. Yang, C. M. Gabardo, G. A. Botton and L. Soleymani, In Situ Liquid Cell TEM Study of Morphological Evolution and Degradation of Pt–Fe Nanocatalysts During Potential Cycling, *J. Phys. Chem. C*, 2014, **118**, 22111–22119.

121 R. Yang, L. Mei, Y. Fan, Q. Zhang, H.-G. Liao, J. Yang, J. Li and Z. Zeng, Fabrication of Liquid Cell for In Situ Transmission Electron Microscopy of Electrochemical Processes, *Nat. Protoc.*, 2023, **18**, 555–578.

122 N. Ortiz Peña, D. Ihiawakrim, M. Han, B. Lassalle-Kaiser, S. Carenco, C. Sanchez, C. Laberty-Robert, D. Portehault and O. Ersen, Morphological and Structural Evolution of Co_3O_4 Nanoparticles Revealed by In Situ Electrochemical Transmission Electron Microscopy during Electrocatalytic Water Oxidation, *ACS Nano*, 2019, **13**, 11372–11381.

123 S. Wei, A. Li, J.-C. Liu, Z. Li, W. Chen, Y. Gong, Q. Zhang, W.-C. Cheong, Y. Wang, L. Zheng, H. Xiao, C. Chen, D. Wang, Q. Peng, L. Gu, X. Han, J. Li and Y. Li, Direct Observation of Noble Metal Nanoparticles Transforming to Thermally Stable Single Atoms, *Nat. Nanotechnol.*, 2018, **13**, 856–861.

124 S. Zhou, J. Shi, S. Liu, G. Li, F. Pei, Y. Chen, J. Deng, Q. Zheng, J. Li, C. Zhao, I. Hwang, C.-J. Sun, Y. Liu, Y. Deng, L. Huang, Y. Qiao, G.-L. Xu, J.-F. Chen, K. Amine, S.-G. Sun and H.-G. Liao, Visualizing Interfacial Collective Reaction Behaviour of Li–S Batteries, *Nature*, 2023, **621**, 75–81.

125 P. Z. Araujo, C. B. Mendive, L. A. G. Rodenas, P. J. Morando, A. E. Regazzoni, M. A. Blesa and D. Bahnemann, FT-IR–ATR As a Tool to Probe Photocatalytic Interfaces, *Colloids Surf., A*, 2005, **265**, 73–80.

126 R. Nakamura and Y. Nakato, Primary Intermediates of Oxygen Photoevolution Reaction on TiO_2 (Rutile) Particles, Revealed by in Situ FTIR Absorption and Photoluminescence Measurements, *J. Am. Chem. Soc.*, 2004, **126**, 1290–1298.

127 H. Su, W. Zhou, W. Zhou, Y. Li, L. Zheng, H. Zhang, M. Liu, X. Zhang, X. Sun, Y. Xu, F. Hu, J. Zhang, T. Hu, Q. Liu and S. Wei, In situ Spectroscopic Observation of Dynamic-coupling Oxygen on Atomically Dispersed Iridium Electrocatalyst for Acidic Water Oxidation, *Nat. Commun.*, 2021, **12**, 6118.

128 D. Bagchi, S. Sarkar, A. K. Singh, C. P. Vinod and S. C. Peter, Potential- and Time-Dependent Dynamic Nature of an Oxide-Derived PdIn Nanocatalyst during Electrochemical CO_2 Reduction, *ACS Nano*, 2022, **16**, 6185–6196.

129 Z. Xu, Z. Liang, W. Guo and R. Zou, In Situ/Operando Vibrational Spectroscopy for the Investigation of Advanced Nanostructured Electrocatalysts, *Coord. Chem. Rev.*, 2021, **436**, 213824.

130 S. Nayak, I. J. McPherson and K. A. Vincent, Adsorbed Intermediates in Oxygen Reduction on Platinum Nanoparticles Observed by In Situ IR Spectroscopy, *Angew. Chem., Int. Ed.*, 2018, **57**, 12855–12858.

131 S. Mondal, D. Bagchi, M. Riyaz, S. Sarkar, A. K. Singh, C. P. Vinod and S. C. Peter, In Situ Mechanistic Insights for the Oxygen Reduction Reaction in Chemically Modulated Ordered Intermetallic Catalyst Promoting Complete Electron Transfer, *J. Am. Chem. Soc.*, 2022, **144**, 11859–11869.

132 L. Li, J. Zhu, F. Kong, Y. Wang, C. Kang, M. Xu, C. Du and G. Yin, Tailoring Atomic Strain Environment for High-performance Acidic Oxygen Reduction by Fe-Ru Dual Atoms Communicative Effect, *Matter*, 2024, **7**, 1517–1532.

133 J.-C. Dong, X.-G. Zhang, V. Briega-Martos, X. Jin, J. Yang, S. Chen, Z.-L. Yang, D.-Y. Wu, J. M. Feliu, C. T. Williams, Z.-Q. Tian and J.-F. Li, In situ Raman Spectroscopic Evidence for Oxygen Reduction Reaction Intermediates at Platinum Single-crystal Surfaces, *Nat. Energy*, 2019, **4**, 60–67.

134 C. Hess, New Advances In Using Raman Spectroscopy for the Characterization of Catalysts and Catalytic Reactions, *Chem. Soc. Rev.*, 2021, **50**, 3519–3564.

135 J. Langer, D. Jimenez de Aberasturi, J. Aizpurua, R. A. Alvarez-Puebla, B. Auguié, J. J. Baumberg, G. C. Bazan, S. E. J. Bell, A. Boisen, A. G. Brolo, J. Choo, D. Cialla-May, V. Deckert, L. Fabris, K. Faulds, F. J. García de Abajo, R. Goodacre, D. Graham, A. J. Haes, C. L. Haynes, C. Huck, T. Itoh, M. Käll, J. Kneipp, N. A. Kotov, H. Kuang, E. C. Le Ru, H. K. Lee, J.-F. Li, X. Y. Ling, S. A. Maier, T. Mayerhöfer, M. Moskovits, K. Murakoshi, J.-M. Nam, S. Nie, Y. Ozaki, I. Pastoriza-Santos, J. Perez-Juste, J. Popp, A. Pucci, S. Reich, B. Ren, G. C. Schatz, T. Shegai, S. Schlücker, L.-L. Tay, K. G. Thomas, Z.-Q. Tian, R. P. Van Duyne, T. Vo-Dinh, Y. Wang, K. A. Willets, C. Xu, H. Xu, Y. Xu, Y. S. Yamamoto, B. Zhao and L. M. Liz-Marzán, Present and Future of Surface-Enhanced Raman Scattering, *ACS Nano*, 2020, **14**, 28–117.

136 X. Wang, S.-C. Huang, S. Hu, S. Yan and B. Ren, Fundamental Understanding and Applications of Plasmon-enhanced Raman Spectroscopy, *Nat. Rev. Phys.*, 2020, **2**, 253–271.

137 H. Zhang, S. Duan, P. M. Radjenovic, Z.-Q. Tian and J.-F. Li, Core–Shell Nanostructure-Enhanced Raman Spectroscopy for Surface Catalysis, *Acc. Chem. Res.*, 2020, **53**, 729–739.

138 C. Tang, C. Wei, Y. Fang, B. Liu, X. Song, Z. Bian, X. Yin, H. Wang, Z. Liu, G. Wang, X. Xiao and X. Duan, Electrocatalytic Hydrogenation of Acetonitrile to Ethylamine in Acid, *Nat. Commun.*, 2024, **15**, 3233.

139 Y. Liu, L. Li, L. Wang, N. Li, X. Zhao, Y. Chen, T. Sakthivel and Z. Dai, Janus Electronic State of Supported Iridium Nanoclusters for Sustainable Alkaline Water Electrolysis, *Nat. Commun.*, 2024, **15**, 2851.

140 J.-W. Zhao, K. Yue, H. Zhang, S.-Y. Wei, J. Zhu, D. Wang, J. Chen, V. Y. Fominski and G.-R. Li, The Formation of Unsaturated IrO_x in $SrIrO_3$ by Cobalt-doping for Acidic Oxygen Evolution Reaction, *Nat. Commun.*, 2024, **15**, 2928.

141 D. Xu, S. Liu, M. Zhang, L. Xu, H. Gao and J. Yao, Manipulating the Dynamic Self-Reconstruction of CoP Electrocatalyst Driven by Charge Transport and Ion Leaching, *Small*, 2023, **19**, 2300201.

142 E. M. van Schrojenstein Lantman, T. Deckert-Gaudig, A. J. G. Mank, V. Deckert and B. M. Weckhuysen, Catalytic Processes Monitored at the Nanoscale with Tip-enhanced Raman spectroscopy, *Nat. Nanotechnol.*, 2012, **7**, 583–586.

143 J.-H. Zhong, X. Jin, L. Meng, X. Wang, H.-S. Su, Z.-L. Yang, C. T. Williams and B. Ren, Probing the Electronic and Catalytic Properties of a Bimetallic Surface with 3 nm Resolution, *Nat. Nanotechnol.*, 2017, **12**, 132–136.

144 H.-L. Wang, E.-M. You, R. Panneerselvam, S.-Y. Ding and Z.-Q. Tian, Advances of Surface-Enhanced Raman and IR Spectroscopies: From Nano/Microstructures to Macro-Optical Design, *Light: Sci. Appl.*, 2021, **10**, 161.

145 X. Chen, X.-T. Wang, J.-B. Le, S.-M. Li, X. Wang, Y.-J. Zhang, P. Radjenovic, Y. Zhao, Y.-H. Wang, X.-M. Lin, J.-C. Dong and J.-F. Li, Revealing the Role of interfacial Water andKey Intermediates at Ruthenium Surfaces in the Alkaline Hydrogen Evolution Reaction, *Nat. Commun.*, 2023, **14**, 5289.

146 H. Zhang, C. Xu, X. Zhan, Y. Yu, K. Zhang, Q. Luo, S. Gao, J. Yang and Y. Xie, Mechanistic Insights into CO_2 Conversion Chemistry of Copper Bis-(terpyridine) Molecular Electrocatalyst Using Accessible Operando Spectrochemistry, *Nat. Commun.*, 2022, **13**, 6029.

147 J. Dong, Y. Liu, J. Pei, H. Li, S. Ji, L. Shi, Y. Zhang, C. Li, C. Tang, J. Liao, S. Xu, H. Zhang, Q. Li and S. Zhao, Continuous Electroproduction of Formate via CO_2 Reduction on Local Symmetry-Broken Single-atom Catalysts, *Nat. Commun.*, 2023, **14**, 6849.

148 X. Chang, S. Vijay, Y. Zhao, N. J. Oliveira, K. Chan and B. Xu, Understanding the Complementarities of Surface-enhanced Infrared and Raman Spectroscopies in CO Adsorption and Electrochemical Reduction, *Nat. Commun.*, 2022, **13**, 2656.

149 Y. Liu, C. Li, C. Tan, Z. Pei, T. Yang, S. Zhang, Q. Huang, Y. Wang, Z. Zhou, X. Liao, J. Dong, H. Tan, W. Yan, H. Yin, Z.-Q. Liu, J. Huang and S. Zhao, Electrosynthesis of Chlorine from Seawater-Like Solution Through Single-Atom Catalysts, *Nat. Commun.*, 2023, **14**, 2475.

150 J. Als-Nielsen and D. McMorrow, in *Elements of Modern X-ray Physics*, 2011, pp. 1–28, DOI: **10.1002/9781119998365.ch1**.

151 J. J. Rehr, J. J. Kas, F. D. Vila, M. P. Prange and K. Jorissen, Parameter-free Calculations of X-ray Spectra with FEFF9, *Phys. Chem. Chem. Phys.*, 2010, **12**, 5503–5513.

152 J. J. Rehr and A. L. Ankudinov, Progress in the Theory and Interpretation of XANES, *Coord. Chem. Rev.*, 2005, **249**, 131–140.

153 G. T. Seidler, D. R. Mortensen, A. J. Remesnik, J. I. Pacold, N. A. Ball, N. Barry, M. Styczinski and O. R. Hoidn, A Laboratory-based Hard X-ray Monochromator for High-resolution X-ray Emission Spectroscopy and X-ray Absorption Near Edge Structure Measurements, *Rev. Sci. Instrum.*, 2014, **85**, 113906.

154 A. Williams, Laboratory X-ray Spectrometer for EXAFS and XANES Measurements, *Rev. Sci. Instrum.*, 1983, **54**, 193–197.

155 D. Wang, J. Zhou, Y. Hu, J. Yang, N. Han, Y. Li and T.-K. Sham, In Situ X-ray Absorption Near-Edge Structure Study of Advanced $NiFe(OH)_x$ Electrocatalyst on Carbon Paper for Water Oxidation, *J. Phys. Chem. C*, 2015, **119**, 19573–19583.

156 Z. Cai, D. Zhou, M. Wang, S.-M. Bak, Y. Wu, Z. Wu, Y. Tian, X. Xiong, Y. Li, W. Liu, S. Siahrostami, Y. Kuang, X.-Q. Yang, H. Duan, Z. Feng, H. Wang and X. Sun, Introducing Fe^{2+} into Nickel–Iron Layered Double Hydroxide: Local Structure Modulated Water Oxidation Activity, *Angew. Chem., Int. Ed.*, 2018, **57**, 9392–9396.

157 T. Kaito, H. Tanaka, H. Mitsumoto, S. Sugawara, K. Shinohara, H. Ariga, H. Uehara, S. Takakusagi and K. Asakura, In Situ X-ray Absorption Fine Structure Analysis of PtCo, PtCu, and PtNi Alloy Electrocatalysts: The Correlation of Enhanced Oxygen Reduction Reaction Activity and Structure, *J. Phys. Chem. C*, 2016, **120**, 11519–11527.

158 Z. Sun, H. Zhang, L. Cao, X. Liu, D. Wu, X. Shen, X. Zhang, Z. Chen, S. Ru, X. Zhu, Z. Xia, Q. Luo, F. Xu and T. Yao, Understanding Synergistic Catalysis on Cu-Se Dual Atom Sites via Operando X-ray Absorption Spectroscopy in Oxygen Reduction Reaction, *Angew. Chem., Int. Ed.*, 2023, **62**, e202217719.

159 D. Cao, D. Liu, S. Chen, O. A. Moses, X. Chen, W. Xu, C. Wu, L. Zheng, S. Chu, H. Jiang, C. Wang, B. Ge, X. Wu, J. Zhang and L. Song, Operando X-ray Spectroscopy Visualizing the Chameleon-Like Structural Reconstruction on an Oxygen Evolution Electrocatalyst, *Energy Environ. Sci.*, 2021, **14**, 906–915.

160 R. Zeng, Y. Yang, X. Feng, H. Li, L. M. Gibbs, F. J. DiSalvo and H. D. Abruña, Nonprecious Transition Metal Nitrides as Efficient Oxygen Reduction Electrocatalysts for Alkaline Fuel Cells, *Sci. Adv.*, 2022, **8**, eabj1584.

161 G. Xing, M. Tong, P. Yu, L. Wang, G. Zhang, C. Tian and H. Fu, Reconstruction of Highly Dense $Cu-N_4$ Active Sites in Electrocatalytic Oxygen Reduction Characterized by Operando Synchrotron Radiation, *Angew. Chem., Int. Ed.*, 2022, **61**, e202211098.

162 D. Liu, T. Ding, L. Wang, H. Zhang, L. Xu, B. Pang, X. Liu, H. Wang, J. Wang, K. Wu and T. Yao, In Situ Constructing Atomic Interface in Ruthenium-based Amorphous Hybrid-structure Towards Solar Hydrogen Evolution, *Nat. Commun.*, 2023, **14**, 1720.

163 P. Yin, X. Niu, S.-B. Li, K. Chen, X. Zhang, M. Zuo, L. Zhang and H.-W. Liang, Machine-learning-accelerated Design of High-performance Platinum Intermetallic Nanoparticle Fuel Cell Catalysts, *Nat. Commun.*, 2024, **15**, 415.

164 W. Peng, J. Liu, X. Liu, L. Wang, L. Yin, H. Tan, F. Hou and J. Liang, Facilitating Two-electron Oxygen Reduction with Pyrrolic Nitrogen Sites for Electrochemical Hydrogen Peroxide Production, *Nat. Commun.*, 2023, **14**, 4430.

165 B.-W. Zhang, T. Zheng, Y.-X. Wang, Y. Du, S.-Q. Chu, Z. Xia, R. Amal, S.-X. Dou and L. Dai, Highly Efficient and Selective Electrocatalytic Hydrogen Peroxide Production on Co-O-C Active Centers on Graphene Oxide, *Commun. Chem.*, 2022, **5**, 43.

166 G. Lin, Q. Ju, Y. Jin, X. Qi, W. Liu, F. Huang and J. Wang, Suppressing Dissolution of Pt-Based Electrocatalysts through the Electronic Metal–Support Interaction, *Adv. Energy Mater.*, 2021, **11**, 2101050.

167 Y. Pan, J. Gao, Y. Li, E. Lv, U. Khan, X. Yang, J. Yao, A. Nairan and Q. Zhang, Constructing Nitrogen-Doped Carbon Hierarchy Structure Derived from Metal-Organic Framework as High-Performance ORR Cathode Material for Zn-Air Battery, *Small*, 2024, **20**, 2304594.

168 D. Zhang, Z. Wang, F. Liu, P. Yi, L. Peng, Y. Chen, L. Wei and H. Li, Unraveling the pH-Dependent Oxygen Reduction Performance on Single-Atom Catalysts: From Single- to Dual-Sabatier Optima, *J. Am. Chem. Soc.*, 2024, **146**, 3210–3219.

169 Y. Zhou, L. Xu, J. Wu, W. Zhu, T. He, H. Yang, H. Huang, T. Cheng, Y. Liu and Z. Kang, The Operation Active Sites of O_2 Reduction to H_2O_2 over ZnO, *Energy Environ. Sci.*, 2023, **16**, 3526–3533.

170 J. Wu, M. Hou, Z. Chen, W. Hao, X. Pan, H. Yang, W. Cen, Y. Liu, H. Huang, P. W. Menezes and Z. Kang, Composition Engineering of Amorphous Nickel Boride Nanoarchitectures Enabling Highly Efficient Electrosynthesis of Hydrogen Peroxide, *Adv. Mater.*, 2022, **34**, 2202995.

171 Y. Tian, M. Li, Z. Wu, Q. Sun, D. Yuan, B. Johannessen, L. Xu, Y. Wang, Y. Dou, H. Zhao and S. Zhang, Edge-hosted Atomic $Co-N_4$ Sites on Hierarchical Porous Carbon for Highly Selective Two-electron Oxygen Reduction Reaction, *Angew. Chem., Int. Ed.*, 2022, **61**, e202213296.

172 W. Fan, Z. Duan, W. Liu, R. Mehmood, J. Qu, Y. Cao, X. Guo, J. Zhong and F. Zhang, Rational Design of Heterogenized Molecular Phthalocyanine Hybrid Single-atom Electrocatalyst Towards Two-electron Oxygen Reduction, *Nat. Commun.*, 2023, **14**, 1426.

173 M. Fan, Z. Wang, K. Sun, A. Wang, Y. Zhao, Q. Yuan, R. Wang, J. Raj, J. Wu, J. Jiang and L. Wang, NBOH Site-Activated Graphene Quantum Dots for Boosting Electrochemical Hydrogen Peroxide Production, *Adv. Mater.*, 2023, **35**, 2209086.

174 C. Zhang, L. Yuan, C. Liu, Z. Li, Y. Zou, X. Zhang, Y. Zhang, Z. Zhang, G. Wei and C. Yu, Crystal Engineering Enables

Cobalt-Based Metal–Organic Frameworks as High-Performance Electrocatalysts for H2O2 Production, *J. Am. Chem. Soc.*, 2023, **145**, 7791–7799.

175 Y. Guo, R. Zhang, S. Zhang, H. Hong, P. Li, Y. Zhao, Z. Huang and C. Zhi, Steering sp-Carbon Content in Graphdiynes for Enhanced Two-Electron Oxygen Reduction to Hydrogen Peroxide, *Angew. Chem., Int. Ed.*, 2024, **63**, e202401501.

176 C. Zhang, W. Shen, K. Guo, M. Xiong, J. Zhang and X. Lu, A Pentagonal Defect-Rich Metal-Free Carbon Electrocatalyst for Boosting Acidic O_2 Reduction to H_2O_2 Production, *J. Am. Chem. Soc.*, 2023, **145**, 11589–11598.

177 Y.-R. Zheng, S. Hu, X.-L. Zhang, H. Ju, Z. Wang, P.-J. Tan, R. Wu, F.-Y. Gao, T. Zhuang, X. Zheng, J. Zhu, M.-R. Gao and S.-H. Yu, Black Phosphorous Mediates Surface Charge Redistribution of $CoSe_2$ for Electrochemical H_2O_2 Production in Acidic Electrolytes, *Adv. Mater.*, 2022, **34**, 2205414.

178 X. Zhao, Q. Yin, X. Mao, C. Cheng, L. Zhang, L. Wang, T.-F. Liu, Y. Li and Y. Li, Theory-guided Design of Hydrogen-bonded Cobaltoporphyrin Frameworks for Highly Selective Electrochemical H_2O_2 Production in Acid, *Nat. Commun.*, 2022, **13**, 2721.

179 F. Xiang, X. Zhao, J. Yang, N. Li, W. Gong, Y. Liu, A. Burguete-Lopez, Y. Li, X. Niu and A. Fratalocchi, Enhanced Selectivity in the Electroproduction of H_2O_2 via F/S Dual-Doping in Metal-Free Nanofibers, *Adv. Mater.*, 2023, **35**, 2208533.

180 Z. Yu, S. Lv, Q. Yao, N. Fang, Y. Xu, Q. Shao, C.-W. Pao, J.-F. Lee, G. Li, L.-M. Yang and X. Huang, Low-Coordinated Pd Site within Amorphous Palladium Selenide for Active, Selective, and Stable H_2O_2 Electrosynthesis, *Adv. Mater.*, 2023, **35**, 2208101.

181 Q. An, X. Zhang, C. Yang, H. Su, W. Zhou, M. Liu, X. Zhang, X. Sun, S. Bo, F. Yu, J. Jiang, K. Zheng and Q. Liu, Engineering Unsymmetrically Coordinated Fe Sites via Heteroatom Pairs Synergetic Contribution for Efficient Oxygen Reduction, *Small*, 2023, **19**, 2304303.

182 G. Zhu, Y. Jiang, H. Yang, H. Wang, Y. Fang, L. Wang, M. Xie, P. Qiu and W. Luo, Constructing Structurally Ordered High-Entropy Alloy Nanoparticles on Nitrogen-Rich Mesoporous Carbon Nanosheets for High-Performance Oxygen Reduction, *Adv. Mater.*, 2022, **34**, 2110128.

183 H. Jin, Z. Xu, Z.-Y. Hu, Z. Yin, Z. Wang, Z. Deng, P. Wei, S. Feng, S. Dong, J. Liu, S. Luo, Z. Qiu, L. Zhou, L. Mai, B.-L. Su, D. Zhao and Y. Liu, Mesoporous Pt@Pt-skin Pt_3Ni Core-shell Framework Nanowire Electrocatalyst for Efficient Oxygen Reduction, *Nat. Commun.*, 2023, **14**, 1518.

184 X. Tang, Y. Wei, W. Zhai, Y. Wu, T. Hu, K. Yuan and Y. Chen, Carbon Nanocage with Maximum Utilization of Atomically Dispersed Iron as Efficient Oxygen Electroreduction Nanoreactor, *Adv. Mater.*, 2023, **35**, 2208942.

185 H. Hu, Z. Xu, Z. Zhang, X. Yan, Y. Zhu, J. P. Attfield and M. Yang, Electrocatalytic Oxygen Reduction Using Metastable Zirconium Suboxide, *Angew. Chem., Int. Ed.*, 2024, e202404374.

186 N. Guo, H. Xue, R. Ren, J. Sun, T. Song, H. Dong, Z. Zhao, J. Zhang, Q. Wang and L. Wu, S-Block Potassium Single-atom Electrocatalyst with $K-N_4$ Configuration Derived from K^+/Polydopamine for Efficient Oxygen Reduction, *Angew. Chem., Int. Ed.*, 2023, **62**, e202312409.

187 Y. Guo, P. Wang, Y. Liu, S. Guo, L. Shi, J. Sun, Y. Tian, X. Wang, S. Zhao and Z. Liu, Dual-type Atomic Ru Promoted Bifunctional Catalytic Process Realizing Ultralow Overpotential for Li-O_2 Batteries, *Appl. Catal., B*, 2024, **356**, 124203.

188 H. Shang, X. Zhou, J. Dong, A. Li, X. Zhao, Q. Liu, Y. Lin, J. Pei, Z. Li, Z. Jiang, D. Zhou, L. Zheng, Y. Wang, J. Zhou, Z. Yang, R. Cao, R. Sarangi, T. Sun, X. Yang, X. Zheng, W. Yan, Z. Zhuang, J. Li, W. Chen, D. Wang, J. Zhang and Y. Li, Engineering Unsymmetrically Coordinated Cu-S_1N_3 Single Atom Sites with Enhanced Oxygen Reduction Activity, *Nat. Commun.*, 2020, **11**, 3049.

189 M. Yuan, Y. Liu, Y. Du, Z. Xiao, H. Li, K. Liu and L. Wang, Dual-Shelled Hollow Leafy Carbon Support with Atomically Dispersed (N,S)-Bridged Hydroxy-Coordinated Asymmetric Fe Sites for Oxygen Reduction, *Adv. Funct. Mater.*, 2024, 2401484.

190 P. Zhu, X. Xiong, X. Wang, C. Ye, J. Li, W. Sun, X. Sun, J. Jiang, Z. Zhuang, D. Wang and Y. Li, Regulating the FeN4 Moiety by Constructing Fe–Mo Dual-Metal Atom Sites for Efficient Electrochemical Oxygen Reduction, *Nano Lett.*, 2022, **22**, 9507–9515.

191 Y. He, Z. Yin, Z. Wang, H. Wang, W. Xiong, B. Song, H. Qin, P. Xu and G. Zeng, Recent Progress on Mixed Transition Metal Nanomaterials Based on Metal–Organic Frameworks for Energy-Related Applications, *J. Mater. Chem. A*, 2022, **10**, 9788–9820.

192 Z.-y. Mei, S. Cai, G. Zhao, X. Zou, Y. Fu, J. Jiang, Q. An, M. Li, T. Liu and H. Guo, Boosting the ORR Active and Zn-air Battery Performance Through Ameliorating the Coordination Environment of Iron Phthalocyanine, *Chem. Eng. J.*, 2022, **430**, 132691.

193 X. Feng, G. Chen, Z. Cui, R. Qin, W. Jiao, Z. Huang, Z. Shang, C. Ma, X. Zheng, Y. Han and W. Huang, Engineering Electronic Structure of Nitrogen-Carbon Sites by sp3-Hybridized Carbon and Incorporating Chlorine to Boost Oxygen Reduction Activity, *Angew. Chem., Int. Ed.*, 2024, **63**, e202316314.

194 L. Li, J. Zhu, F. Kong, Y. Wang, C. Kang, M. Xu, C. Du and G. Yin, Tailoring Atomic Strain Environment for High-performance Acidic Oxygen Reduction by Fe-Ru Dual Atoms Communicative Effect, *Matter*, 2024, **7**, 1517–1532.

195 J. Gao and B. Liu, Progress of Electrochemical Hydrogen Peroxide Synthesis over Single Atom Catalysts, *ACS Mater. Lett.*, 2020, **2**, 1008–1024.

196 J. M. Campos-Martin, G. Blanco-Brieva and J. L. G. Fierro, Hydrogen Peroxide Synthesis: An Outlook beyond the Anthraquinone Process, *Angew. Chem., Int. Ed.*, 2006, **45**, 6962–6984.

197 B. Bayatsarmadi, Y. Zheng, A. Vasileff and S.-Z. Qiao, Recent Advances in Atomic Metal Doping of Carbon-based Nanomaterials for Energy Conversion, *Small*, 2017, **13**, 1700191.

198 S. Yang, Y. J. Tak, J. Kim, A. Soon and H. Lee, Support Effects in Single-Atom Platinum Catalysts for Electrochemical Oxygen Reduction, *ACS Catal.*, 2017, **7**, 1301–1307.

199 J. Tang, T. Zhao, D. Solanki, X. Miao, W. Zhou and S. Hu, Selective Hydrogen Peroxide Conversion Tailored by Surface, Interface, and Device Engineering, *Joule*, 2021, **5**, 1432–1461.

200 Y. Wang, R. Shi, L. Shang, L. Peng, D. Chu, Z. Han, G. I. N. Waterhouse, R. Zhang and T. Zhang, Vertical Graphene Array for Efficient Electrocatalytic Reduction of Oxygen to Hydrogen Peroxide, *Nano Energy*, 2022, **96**, 107046.

201 R. Lu, C. Quan, C. Zhang, Q. He, X. Liao, Z. Wang and Y. Zhao, Establishing a Theoretical Insight for Penta-coordinated Iron-nitrogen-carbon Catalysts Toward Oxygen Reaction, *Nano Res.*, 2022, **15**, 6067–6075.

202 H. Niu, X. Wan, X. Wang, C. Shao, J. Robertson, Z. Zhang and Y. Guo, Single-Atom Rhodium on Defective g-C_3N_4: A Promising Bifunctional Oxygen Electrocatalyst, *ACS Sustain. Chem. Eng.*, 2021, **9**, 3590–3599.

203 X. Chen, Y. Li and X. Zhao, Screening of Transition Metal-based MOF as Highly Efficient Bifunctional Electrocatalysts for Oxygen Reduction and Oxygen Evolution, *Surf. Interfaces*, 2023, **38**, 102821.

204 Y. Wang, C. Han, L. Ma, T. Duan, Y. Du, J. Wu, J.-J. Zou, J. Gao, X.-D. Zhu and Y.-C. Zhang, Recent Progress of Transition Metal Selenides for Electrochemical Oxygen Reduction to Hydrogen Peroxide: From Catalyst Design to Electrolyzers Application, *Small*, 2024, 2309448.

205 N. Karmodak and J. K. Nørskov, Activity And Stability of Single- And Di-Atom Catalysts for the O_2 Reduction Reaction, *Angew. Chem., Int. Ed.*, 2023, **62**, e202311113.

206 C. Lang, J. Li, K. R. Yang, Y. Wang, D. He, J. E. Thorne, S. Croslow, Q. Dong, Y. Zhao, G. Prostko, G. W. Brudvig, V. S. Batista, M. M. Waegele and D. Wang, Observation of a Potential-Dependent Switch of Water-oxidation Mechanism on Co-oxide-based Catalysts, *Chem*, 2021, **7**, 2101–2117.

207 O. Zandi and T. W. Hamann, Determination of Photoelectrochemical Water Oxidation Intermediates on Haematite Electrode Surfaces Using Operando Infrared Spectroscopy, *Nat. Chem.*, 2016, **8**, 778–783.

208 S. Chen, T. Luo, K. Chen, Y. Lin, J. Fu, K. Liu, C. Cai, Q. Wang, H. Li, X. Li, J. Hu, H. Li, M. Zhu and M. Liu, Chemical Identification of Catalytically Active Sites on Oxygen-doped Carbon Nanosheet to Decipher the High Activity for Electro-synthesis Hydrogen Peroxide, *Angew. Chem., Int. Ed.*, 2021, **60**, 16607–16614.

209 S. Chen, Z. Chen, S. Siahrostami, D. Higgins, D. Nordlund, D. Sokaras, T. R. Kim, Y. Liu, X. Yan, E. Nilsson, R. Sinclair, J. K. Nørskov, T. F. Jaramillo and Z. Bao, Designing Boron Nitride Islands in Carbon Materials for Efficient Electrochemical Synthesis of Hydrogen Peroxide, *J. Am. Chem. Soc.*, 2018, **140**, 7851–7859.

210 Z. Lu, G. Chen, S. Siahrostami, Z. Chen, K. Liu, J. Xie, L. Liao, T. Wu, D. Lin, Y. Liu, T. F. Jaramillo, J. K. Nørskov and Y. Cui, High-efficiency oxygen reduction to hydrogen peroxide catalysed by oxidized carbon materials, *Nat. Catal.*, 2018, **1**, 156–162.

211 F. Wu, C. Pan, C.-T. He, Y. Han, W. Ma, H. Wei, W. Ji, W. Chen, J. Mao, P. Yu, D. Wang, L. Mao and Y. Li, Single-Atom Co–N_4 Electrocatalyst Enabling Four-Electron Oxygen Reduction with Enhanced Hydrogen Peroxide Tolerance for Selective Sensing, *J. Am. Chem. Soc.*, 2020, **142**, 16861–16867.

212 H. Xu, X.-H. Lv, H.-Y. Wang, J.-Y. Ye, J. Yuan, Y.-C. Wang, Z.-Y. Zhou and S.-G. Sun, Impact of Pore Structure on Two-Electron Oxygen Reduction Reaction in Nitrogen-Doped Carbon Materials: Rotating Ring-Disk Electrode vs. Flow Cell, *ChemSusChem*, 2022, **15**, e202102587.

213 A. E. Thorarinsdottir, D. P. Erdosy, C. Costentin, J. A. Mason and D. G. Nocera, Enhanced Activity for the Oxygen Reduction Reaction in Microporous Water, *Nat. Catal.*, 2023, **6**, 425–434.

214 J. Xie, L. Zhong, X. Yang, D. He, K. Lin, X. Chen, H. Wang, S. Gan and L. Niu, Phosphorous and Selenium Tuning Co-based Non-precious Catalysts for Electrosynthesis of H_2O_2 in Acidic Media, *Chin. Chem. Lett.*, 2024, **35**, 108472.

215 C. Xia, J. Y. Kim and H. Wang, Recommended Practice to Report Selectivity in Electrochemical Synthesis of H_2O_2, *Nat. Catal.*, 2020, **3**, 605–607.

216 Z. Wang, Q.-K. Li, C. Zhang, Z. Cheng, W. Chen, E. A. McHugh, R. A. Carter, B. I. Yakobson and J. M. Tour, Hydrogen Peroxide Generation with 100% Faradaic Efficiency on Metal-Free Carbon Black, *ACS Catal.*, 2021, **11**, 2454–2459.

217 L. Bu, S. Guo, X. Zhang, X. Shen, D. Su, G. Lu, X. Zhu, J. Yao, J. Guo and X. Huang, Surface Engineering of Hierarchical Platinum-cobalt Nanowires for Efficient Electrocatalysis, *Nat. Commun.*, 2016, **7**, 11850.

218 S. Luo and P. K. Shen, Concave Platinum–Copper Octopod Nanoframes Bounded with Multiple High-Index Facets for Efficient Electrooxidation Catalysis, *ACS Nano*, 2017, **11**, 11946–11953.

219 C. Chen, Y. Kang, Z. Huo, Z. Zhu, W. Huang, H. L. Xin, J. D. Snyder, D. Li, J. A. Herron, M. Mavrikakis, M. Chi, K. L. More, Y. Li, N. M. Markovic, G. A. Somorjai, P. Yang and V. R. Stamenkovic, Highly Crystalline Multimetallic Nanoframes with Three-Dimensional Electrocatalytic Surfaces, *Science*, 2014, **343**, 1339–1343.

220 H. Y. Kim, T. Kwon, Y. Ha, M. Jun, H. Baik, H. Y. Jeong, H. Kim, K. Lee and S. H. Joo, Intermetallic PtCu Nanoframes as Efficient Oxygen Reduction Electrocatalysts, *Nano Lett.*, 2020, **20**, 7413–7421.

221 D. Wang, H. L. Xin, R. Hovden, H. Wang, Y. Yu, D. A. Muller, F. J. DiSalvo and H. D. Abruña, Structurally Ordered Intermetallic Platinum–cobalt Core–shell Nanoparticles with Enhanced Activity and Stability as

Oxygen Reduction Eelectrocatalysts, *Nat. Mater.*, 2013, **12**, 81–87.

222 B. Y. Xia, Y. Yan, N. Li, H. B. Wu, X. W. Lou and X. Wang, A Metal–organic Framework-Derived Bifunctional Oxygen Electrocatalyst, *Nat. Energy*, 2016, **1**, 15006.

223 L. Huang, S. Zaman, X. Tian, Z. Wang, W. Fang and B. Y. Xia, Advanced Platinum-Based Oxygen Reduction Electrocatalysts for Fuel Cells, *Acc. Chem. Res.*, 2021, **54**, 311–322.

224 L. Huang, Y.-Q. Su, R. Qi, D. Dang, Y. Qin, S. Xi, S. Zaman, B. You, S. Ding and B. Y. Xia, Boosting Oxygen Reduction via Integrated Construction and Synergistic Catalysis of Porous Platinum Alloy and Defective Graphitic Carbon, *Angew. Chem., Int. Ed.*, 2021, **60**, 25530–25537.

225 Q. An, X. Zhang, C. Yang, H. Su, W. Zhou, M. Liu, X. Zhang, X. Sun, S. Bo, F. Yu, J. Jiang, K. Zheng and Q. Liu, Engineering Unsymmetrically Coordinated Fe Sites via Heteroatom Pairs Synergetic Contribution for Efficient Oxygen Reduction, *Small*, 2023, 2304303.

226 J. Balamurugan, P. M. Austeria, J. B. Kim, E.-S. Jeong, H.-H. Huang, D. H. Kim, N. Koratkar and S. O. Kim, Electrocatalysts for Zinc–Air Batteries Featuring Single Molybdenum Atoms in a Nitrogen-Doped Carbon Framework, *Adv. Mater.*, 2023, **35**, 2302625.

227 R. Sui, X. Zhang, X. Wang, X. Wang, J. Pei, Y. Zhang, X. Liu, W. Chen, W. Zhu and Z. Zhuang, Silver Based Single Atom Catalyst With Heteroatom Coordination Environment as High Performance Oxygen Reduction Reaction Catalyst, *Nano Res.*, 2022, **15**, 7968–7975.

228 Y. Feng, L. Zhou, H. Ma, Z. Wu, Q. Zhao, H. Li, K. Zhang and J. Chen, Challenges and Advances in Wide-temperature Rechargeable Lithium Batteries, *Energy Environ. Sci.*, 2022, **15**, 1711–1759.

229 D. S. Choi, A. W. Robertson, J. H. Warner, S. O. Kim and H. Kim, Low-Temperature Chemical Vapor Deposition Synthesis of Pt–Co Alloyed Nanoparticles with Enhanced Oxygen Reduction Reaction Catalysis, *Adv. Mater.*, 2016, **28**, 7115–7122.

230 M. Liu, Z. Zhao, X. Duan and Y. Huang, Nanoscale Structure Design for High-Performance Pt-Based ORR Catalysts, *Adv. Mater.*, 2019, **31**, 1802234.

231 H. Huang, D. Yu, F. Hu, S.-C. Huang, J. Song, H.-Y. Chen, L. L. Li and S. Peng, Clusters Induced Electron Redistribution to Tune Oxygen Reduction Activity of Transition Metal Single-Atom for Metal–Air Batteries, *Angew. Chem., Int. Ed.*, 2022, **61**, e202116068.

232 W. Ni, Z. Liu, Y. Zhang, C. Ma, H. Deng, S. Zhang and S. Wang, Electroreduction of Carbon Dioxide Driven by the Intrinsic Defects in the Carbon Plane of a Single Fe–N_4 Site, *Adv. Mater.*, 2021, **33**, 2003238.

233 A. Zitolo, V. Goellner, V. Armel, M.-T. Sougrati, T. Mineva, L. Stievano, E. Fonda and F. Jaouen, Identification of Catalytic Sites for Oxygen Reduction in Iron- and Nitrogen-doped Graphene Materials, *Nat. Mater.*, 2015, **14**, 937–942.

234 G. Chen, R. Lu, C. Li, J. Yu, X. Li, L. Ni, Q. Zhang, G. Zhu, S. Liu, J. Zhang, U. I. Kramm, Y. Zhao, G. Wu, J. Xie and X. Feng, Hierarchically Porous Carbons with Highly Curved Surfaces for Hosting Single Metal FeN4 Sites as Outstanding Oxygen Reduction Catalysts, *Adv. Mater.*, 2023, **35**, 2300907.

235 G. Zhang, D. Sebastián, X. Zhang, Q. Wei, C. Lo Vecchio, J. Zhang, V. Baglio, W. Wang, S. Sun, A. S. Aricò and A. C. Tavares, Engineering of a Low-Cost, Highly Active, and Durable Tantalate–Graphene Hybrid Electrocatalyst for Oxygen Reduction, *Adv. Energy Mater.*, 2020, **10**, 2000075.

236 Z.-y. Mei, G. Zhao, C. Xia, S. Cai, Q. Jing, X. Sheng, H. Wang, X. Zou, L. Wang, H. Guo and B. Y. Xia, Regulated High-Spin State and Constrained Charge Behavior of Active Cobalt Sites in Covalent Organic Frameworks for Promoting Electrocatalytic Oxygen Reduction, *Angew. Chem., Int. Ed.*, 2023, **62**, e202303871.

237 L. Yin, S. Zhang, M. Sun, S. Wang, B. Huang and Y. Du, Heteroatom-Driven Coordination Fields Altering Single Cerium Atom Sites for Efficient Oxygen Reduction Reaction, *Adv. Mater.*, 2023, **35**, 2302485.

238 S. Liu, C. Li, M. J. Zachman, Y. Zeng, H. Yu, B. Li, M. Wang, J. Braaten, J. Liu, H. M. Meyer, M. Lucero, A. J. Kropf, E. E. Alp, Q. Gong, Q. Shi, Z. Feng, H. Xu, G. Wang, D. J. Myers, J. Xie, D. A. Cullen, S. Litster and G. Wu, Atomically Dispersed Iron Sites with a Nitrogen–carbon Coating as Highly Active and Durable Oxygen Reduction Catalysts for Fuel Cells, *Nat. Energy*, 2022, **7**, 652–663.

239 Y. Shao, J.-P. Dodelet, G. Wu and P. Zelenay, PGM-Free Cathode Catalysts for PEM Fuel Cells: A Mini-Review on Stability Challenges, *Adv. Mater.*, 2019, **31**, 1807615.

240 J. Gu, C.-S. Hsu, L. Bai, H. M. Chen and X. Hu, Atomically Dispersed Fe^{3+} Sites Catalyze Efficient CO_2 Electroreduction to CO, *Science*, 2019, **364**, 1091–1094.

241 Y. Wang, Y.-J. Tang and K. Zhou, Self-Adjusting Activity Induced by Intrinsic Reaction Intermediate in Fe–N–C Single-Atom Catalysts, *J. Am. Chem. Soc.*, 2019, **141**, 14115–14119.

242 K. Liu, J. Fu, Y. Lin, T. Luo, G. Ni, H. Li, Z. Lin and M. Liu, Insights into the Activity of Single-atom Fe-N-C catalysts for Oxygen Reduction Reaction, *Nat. Commun.*, 2022, **13**, 2075.

243 J. Liu, J. Zhu, H. Xu and D. Cheng, Rational Design of Heteroatom-Doped Fe–N–C Single-Atom Catalysts for Oxygen Reduction Reaction via Simple Descriptor, *ACS Catal.*, 2024, **14**, 6952–6964.

244 J. Cheng, C. Lyu, H. Li, J. Wu, Y. Hu, B. Han, K. Wu, M. Hojamberdiev and D. Geng, Steering the Oxygen Reduction Reaction Pathways of N-carbon Hollow Spheres by Heteroatom Doping, *Appl. Catal., B*, 2023, **327**, 122470.

245 C. Tang, L. Chen, H. Li, L. Li, Y. Jiao, Y. Zheng, H. Xu, K. Davey and S.-Z. Qiao, Tailoring Acidic Oxygen Reduction Selectivity on Single-Atom Catalysts via Modification of First and Second Coordination Spheres, *J. Am. Chem. Soc.*, 2021, **143**, 7819–7827.

246 Z. Zhuang, A. Huang, X. Tan, K. Sun, C. Chen, Q. Peng, Z. Zhuang, T. Han, H. Xiao, Y. Zeng, W. Yan, J. Zhang and Y. Li, p-Block-metal Bismuth-based Electrocatalysts

Featuring Tunable Selectivity for High-performance Oxygen Reduction Reaction, *Joule*, 2023, **7**, 1003–1015.

247 M. Yan, H. Yang, Z. Gong, J. Zhu, C. Allen, T. Cheng and H. Fei, Sulfur-Tuned Main-Group Sb−N−C Catalysts for Selective 2-Electron and 4-Electron Oxygen Reduction, *Adv. Mater.*, 2024, 2402963.

248 E. Jung, H. Shin, B.-H. Lee, V. Efremov, S. Lee, H. S. Lee, J. Kim, W. Hooch Antink, S. Park, K.-S. Lee, S.-P. Cho, J. S. Yoo, Y.-E. Sung and T. Hyeon, Atomic-level tuning of Co–N–C catalyst for high-performance electrochemical H_2O_2 production, *Nat. Mater.*, 2020, **19**, 436–442.

249 M. Ko, Y. Kim, J. Woo, B. Lee, R. Mehrotra, P. Sharma, J. Kim, S. W. Hwang, H. Y. Jeong, H. Lim, S. H. Joo, J.-W. Jang and J. H. Kwak, Direct Propylene Epoxidation with Oxygen Using a Photo-Electro-heterogeneous Catalytic System, *Nat. Catal.*, 2022, **5**, 37–44.

250 S. Choi, C. J. Kucharczyk, Y. Liang, X. Zhang, I. Takeuchi, H.-I. Ji and S. M. Haile, Exceptional Power Density and Stability at Intermediate Temperatures in Protonic Ceramic Fuel Cells, *Nat. Energy*, 2018, **3**, 202–210.

251 E.-O. Oh, C.-M. Whang, Y.-R. Lee, S.-Y. Park, D. H. Prasad, K. J. Yoon, J.-W. Son, J.-H. Lee and H.-W. Lee, Extremely Thin Bilayer Electrolyte for Solid Oxide Fuel Cells (SOFCs) Fabricated by Chemical Solution Deposition (CSD), *Adv. Mater.*, 2012, **24**, 3373–3377.

252 K. Bae, D. H. Kim, H. J. Choi, J.-W. Son and J. H. Shim, High-Performance Protonic Ceramic Fuel Cells with 1 μm Thick Y:Ba(Ce, Zr)O_3 Electrolytes, *Adv. Energy Mater.*, 2018, **8**, 1801315.

253 J. H. Kim, J. K. Kim, H. G. Seo, D.-K. Lim, S. J. Jeong, J. Seo, J. Kim and W. Jung, Ex-Solved Ag Nanocatalysts on a Sr-Free Parent Scaffold Authorize a Highly Efficient Route of Oxygen Reduction, *Adv. Funct. Mater.*, 2020, **30**, 2001326.

254 Z. Lin, Q. Zhang, J. Pan, C. Tsounis, A. A. Esmailpour, S. Xi, H. Y. Yang, Z. Han, J. Yun, R. Amal and X. Lu, Atomic Co Decorated Free-standing Graphene Electrode Assembly for Efficient Hydrogen Peroxide Production in Acid, *Energy Environ. Sci.*, 2022, **15**, 1172–1182.

255 X. Zhang, X. Zhao, P. Zhu, Z. Adler, Z.-Y. Wu, Y. Liu and H. Wang, Electrochemical Oxygen Reduction to Hydrogen Peroxide at Practical Rates in Strong Acidic Media, *Nat. Commun.*, 2022, **13**, 2880.

256 J. Zhang, S. Ricote, P. V. Hendriksen and Y. Chen, Advanced Materials for Thin-Film Solid Oxide Fuel Cells: Recent Progress and Challenges in Boosting the Device Performance at Low Temperatures, *Adv. Funct. Mater.*, 2022, **32**, 2111205.

257 X. Bi, Y. Jiang, R. Chen, Y. Du, Y. Zheng, R. Yang, R. Wang, J. Wang, X. Wang and Z. Chen, Rechargeable Zinc–Air Versus Lithium–Air Battery: From Fundamental Promises Toward Technological Potentials, *Adv. Energy Mater.*, 2024, **14**, 2302388.

258 H. W. Kim, M. B. Ross, N. Kornienko, L. Zhang, J. Guo, P. Yang and B. D. McCloskey, Efficient Hydrogen Peroxide Generation Using Reduced Graphene Oxide-based Oxygen Reduction Electrocatalysts, *Nat. Catal.*, 2018, **1**, 282–290.

259 G.-F. Han, F. Li, W. Zou, M. Karamad, J.-P. Jeon, S.-W. Kim, S.-J. Kim, Y. Bu, Z. Fu, Y. Lu, S. Siahrostami and J.-B. Baek, Building and identifying highly active oxygenated groups in carbon materials for oxygen reduction to H_2O_2, *Nat. Commun.*, 2020, **11**, 2209.

260 C. Xia, P. Zhu, Q. Jiang, Y. Pan, W. Liang, E. Stavitski, H. N. Alshareef and H. Wang, Continuous Production of Pure Liquid Fuel Solutions Via Electrocatalytic CO_2 Reduction Using Solid-Electrolyte Devices, *Nat. Energy*, 2019, **4**, 776–785.

261 X. Zhao and Y. Liu, Unveiling the Active Structure of Single Nickel Atom Catalysis: Critical Roles of Charge Capacity and Hydrogen Bonding, *J. Am. Chem. Soc.*, 2020, **142**, 5773–5777.

262 Y. Ding, P. Cai and Z. Wen, Electrochemical Neutralization Energy: From Concept to Devices, *Chem. Soc. Rev.*, 2021, **50**, 1495–1511.

263 K. Jiao, J. Xuan, Q. Du, Z. Bao, B. Xie, B. Wang, Y. Zhao, L. Fan, H. Wang, Z. Hou, S. Huo, N. P. Brandon, Y. Yin and M. D. Guiver, Designing the Next Generation of Proton-exchange Membrane Fuel Cells, *Nature*, 2021, **595**, 361–369.

264 Z. M. Bhat, D. Pandit, S. Ardo, R. Thimmappa, A. R. Kottaichamy, N. Christudas Dargily, M. C. Devendrachari and M. Ottakam Thotiyl, An Electrochemical Neutralization Cell for Spontaneous Water Desalination, *Joule*, 2020, **4**, 1730–1742.

265 F. Liu, L. Shi, X. Lin, D. Yu, C. Zhang, R. Xu, D. Liu, J. Qiu and L. Dai, Site-density Engineering of Single-atomic Iron Catalysts for High-performance Proton Exchange Membrane Fuel Cells, *Appl. Catal., B*, 2022, **302**, 120860.

266 M. Z. Jacobson, M. A. Delucchi, Z. A. F. Bauer, S. C. Goodman, W. E. Chapman, M. A. Cameron, C. Bozonnat, L. Chobadi, H. A. Clonts, P. Enevoldsen, J. R. Erwin, S. N. Fobi, O. K. Goldstrom, E. M. Hennessy, J. Liu, J. Lo, C. B. Meyer, S. B. Morris, K. R. Moy, P. L. O'Neill, I. Petkov, S. Redfern, R. Schucker, M. A. Sontag, J. Wang, E. Weiner and A. S. Yachanin, 100% Clean and Renewable Wind, Water, and Sunlight All-Sector Energy Roadmaps for 139 Countries of the World, *Joule*, 2017, **1**, 108–121.

267 S. Choudhury, S. Wei, Y. Ozhabes, D. Gunceler, M. J. Zachman, Z. Tu, J. H. Shin, P. Nath, A. Agrawal, L. F. Kourkoutis, T. A. Arias and L. A. Archer, Designing Solid-liquid Interphases for Sodium Batteries, *Nat. Commun.*, 2017, **8**, 898.

268 T. Li, M. Huang, X. Bai and Y.-X. Wang, Metal–air batteries: A Review on Current Status and Future Applications, *Prog. Nat. Sci.: Mater. Int.*, 2023, **33**, 151–171.

269 Q. Wang, S. Kaushik, X. Xiao and Q. Xu, Sustainable Zinc–air Battery Chemistry: Advances, Challenges and Prospects, *Chem. Soc. Rev.*, 2023, **52**, 6139–6190.

270 J.-N. Liu, C.-X. Zhao, J. Wang, D. Ren, B.-Q. Li and Q. Zhang, A brief History of Zinc–air Batteries: 140 Years of Epic Adventures, *Energy Environ. Sci.*, 2022, **15**, 4542–4553.

271 Y. Chen, J. Xu, P. He, Y. Qiao, S. Guo, H. Yang and H. Zhou, Metal-air batteries: Progress and Perspective, *Sci. Bull.*, 2022, **67**, 2449–2486.

272 Q. Liu, R. Liu, C. He, C. Xia, W. Guo, Z.-L. Xu and B. Y. Xia, Advanced Polymer-based Electrolytes in Zinc–air Batteries, *eScience*, 2022, **2**, 453–466.

273 S. Chai, Y. Zhang, Y. Wang, Q. He, S. Zhou and A. Pan, Biodegradable Composite Polymer as Advanced Gel Electrolyte for Qquasi-solid-state Lithium-metal Battery, *eScience*, 2022, **2**, 494–508.